Theoretical Optimization and Experimental Validation of a Microchannel Target for a High-current Accelerator-driven Neutron Source

Theoretische Optimierung und experimentelle Validierung eines Mikrokanaltargets für eine beschleunigergetriebene Neutronenquelle mit hohen Strömen

Von der Fakultät für Maschinenwesen der Rheinisch-Westfälischen Technischen Hochschule Aachen zur Erlangung des akademischen Grades einer Doktorin der Ingenieurwissenschaften genehmigte Dissertation

vorgelegt von

Qi Ding

Berichter: Univ.-Prof. Dr. rer. nat. Ghaleb Natour
Univ.-Prof. Dr. rer. nat. habil. Thomas Brückel
Univ.-Prof. Dr.-Ing. Lorenz Singheiser

Tag der mündlichen Prüfung: 01.08.2023

Abstract

The High Brilliance neutron Source (HBS) project aims to develop a high-current accelerator-driven neutron source (Hi-CANS) to deliver high-brilliant neutron beams to a variety of neutron scattering instruments. One of the key components of such a facility is the target that generates neutrons from nuclear reactions between protons and atoms of the target material.

Within the HBS project, a solid tantalum target with an innovative internal microchannel water-cooling structure was developed for a 70 MeV pulsed proton beam with a peak current of 100 mA, a duty cycle of 1.43% and an average power of 100 kW deposited on a surface area of 100 cm^2. Known potential risks like blistering, sufficient heat dissipation and thermomechanical stresses have been consequently tackled during the development by optimizing the neutron-producing target accordingly.

The first solid tantalum target with an internal microchannel water-cooling structure was manufactured and tested with a high-power electron beam. It was shown that a power of 1 kW/cm^2 can be dissipated with the special microchannel cooling.

In addition, a new target with an optimized microchannel structure was obtained from an iteration between particle transport simulations with FLUKA and thermomechanical simulations with ANSYS. Only 4.56% of protons accumulate in the neutron-producing tantalum and hence blistering issues are minimized. Additionally, a homogeneous heat deposition within the target was achieved minimizing strains and stresses. Steady-state and transient analysis on the cooling effect of the target in operation shows that the maximum temperature and heat flux could be kept in a safe range with the proposed microchannel structure. A prototype of the optimized target was manufactured via wire erosion and the tolerances were examined successfully with computed tomography. The maximum machining error is 0.2 mm and the effect on the target's lifetime is negligible, proving the optimized microchannel target is manufacturable and reliable.

Kurzfassung

Das High Brilliance neutron Source (HBS) Projekt zielt darauf ab, eine beschleunigergetriebene Hochstrom-Neutronenquelle (Hi-CANS) zu entwickeln, die hochbrillante Neutronenstrahlen für eine Vielzahl von Neutronenstreuungsinstrumenten liefert. Eine der Hauptkomponenten einer solchen Anlage ist das Target, in dem freie Neutronen durch nukleare Reaktionen zwischen Protonen und den Atomen des Targetmaterials erzeugt werden.

Im Rahmen des HBS-Projekts wurde ein Festkörper-Target aus Tantal mit einer internen Mikrokanal-Wasserkühlstruktur für einen gepulsten Protonenstrahl von 70 MeV, einem Spitzenstrom von 100 mA, einem Tastverhältnis von 1.43% und einer mittleren Leistung von 100 kW, aufgetragen auf einer Fläche von 100 cm^2, entwickelt. Bekannte Risiken wie Blasenbildung, ausreichende Kühlung und thermomechanische Spannungen wurden während der Entwicklung, durch Optimierung des Targets zur Neutronenproduktion, konsequent angegangen.

Das erste Design eines festen Tantal-Targets mit einer internen Mikrokanal-Wasserkühlstruktur wurde mit einem hochleistungs Elektronenstrahls getestet. Es hat sich gezeigt, dass mit dem speziellen Mikrokanal-Kühlkonzept eine Leistung von 1 kW/cm² abgeführt werden kann.

Darüber hinaus wurde ein neues Target mit einer optimierten Mikrokanalstruktur aus einer Iteration zwischen dem Partikeltransportcode FLUKA und thermomechanischen Simulationen mit ANSYS gewonnen. Nur 4.56% der Protonen reichern sich im Metalltarget an, so dass Blasenbildung auf ein Minimum reduziert wird. Zusätzlich wurde eine homogene Wärmeabgabe innerhalb des Targets erreicht, wodurch Dehnungen und Spannungen minimiert wurden. Die stationäre und transiente Analyse der Targetkühlwirkung hat gezeigt, dass die maximale Temperatur und der Wärmestrom mit der vorgeschlagenen Mikrokanalstruktur in einem sicheren Bereich gehalten werden kann. Außerdem wurde ein Prototyp des optimierten Targets hergestellt und die Toleranzen erfolgreich mit Computertomographie untersucht. Der maximale Bearbeitungsfehler beträgt 0.02 cm und die Auswirkungen auf die Lebensdauer des Targets sind vernachlässigbar, was beweist, dass das optimierte Mikrokanaltarget herstellbar und zuverlässig ist.

Contents

1 Introduction

Neutrons are a powerful probe for fundamental and applied research in sciences as well as in many technical and industrial fields [1 - 4]. For example, they can be applied in biological material analysis, material characterization and non-destructive testing [5 - 8]. As a neutral particle, the neutron does not carry an electric charge and thus has a high penetration depth through matter without energy loss from ionization, allowing it to be used for non-destructive investigation of large objects such as engineering devices, geological samples, or cultural artifacts. The other advantage is that neutrons interact strongly with hydrogen nuclei (protons), providing them a unique tool for investigating organic material and thus matter when it comes to hydrogen atom localization. Furthermore, neutrons have a magnetic moment due to their nuclear spin, which allows the determination of magnetic structures, magnetic excitations and fluctuations down to atomic length scales. Consequently, neutrons become an indispensable microscopic probe due to these astonishingly unique properties.

The conventional neutron provision is currently mainly provided by the large-scale facilities based on fission in nuclear reactors and spallation using high-power proton accelerators. These two techniques are widely utilized in Europe and provide the highest neutron source strength with a wide range of possibilities. The high neutron fluxes are achieved at the research fission reactors such as the FRM II [9] at the Heinz Maier-Leibnitz Zentrum in Germany with a thermal power of 20 MW offering an average neutron flux more than 10^{14} n/cm^2/s and the ILL (the Institut Laue-Langevin) high flux reactor [10] in France with a thermal power of 58.3MW providing an average neutron flux of 1.5×10^{15} n/cm^2/s [11]. However, the primary fuel element of highly enriched uranium in nuclear reactors is limited available. On the other hand, the issue of disposal and treatment of nuclear fission reactors in terms of radioactive waste management is challenging and is subject to intense debates and of great public concern. Especially in Germany, the government announced a political restriction on nuclear power in June 2011, which also results in that more and more research reactors being decommissioned throughout Europe. For example, BER II reactor in Germany was permanently decommissioned in 2019 as well as ORPHEE reactor in France was also permanently shut down in 2019 [12].

Spallation sources are one alternative approach for replacing high-performance research reactors. According to the references, spallation is a two-stage process that occurs when high-Z materials are bombarded with high energy protons (E ≥ 100MeV): the incident particle disintegrates the nucleus through inelastic nuclear reactions, consequently the target nuclei to become extremely excited and produce up to 30 neutrons per incoming proton [13]. However, the European Spallation Source (ESS) [14], a world-leading project with a time-averaged neutron flux of 3×10^{15} n/cm^2/s [15] built by European collaboration in Lund, Sweden, which is expected to start operation in 2025 [16]. New large-scale facilities based on reactors are cost-intensive and challenging to implement due to political constraints. On the other hand, the continuously high demand for neutron experiments exceeds the available capacity and thus a gap in the supply of neutrons occurs [12]. To expand the user community and promote the industrial applications of neutron beams, the high-current accelerator-driven neutron sources play an important role. It is a promising new type of neutron source which produces neutrons through nuclear reactions with sub-100MeV proton or deuteron accelerators.

1.1 High Brilliance neutron Source (HBS) project

Such a high-current compact accelerator-driven neutron source (HiCANS) [17 - 20] is currently planned at the Jülich Centre for Neutron Science (JCNS) of the Forschungszentrum Jülich GmbH in the frame of the High Brilliance neutron Source (HBS) project [21 - 23]. The HBS project aims at developing a medium-flux accelerator-driven neutron source based on a 70MeV, 100mA high current linear proton linear accelerator, and to delivery high brilliance neutron beams to a variety of neutron instruments.

In terms of the neutron yield in typical neutron sources, fission research reactors produce one usable neutron per fission event [24], for example, at ILL in France. Fission reactors enable that resolutions can be more easily tailored to experimental requirements due to its higher average flux of 10^{15} n/cm/^{2}/s [25], but it causes a high energy deposition (∼180 MeV) per useful neutron. Spallation sources generate approximately 20 - 30 neutrons per nuclear reaction [24], (∼15 in the specific case of ISIS Neutron Source [26]). Compared to reactor sources, spallation sources benefit from the lower energy deposition of ∼30 MeV per useful neutron [26]. However, the construction

of spallation sources is cost-intensive. HiCANS produces approximate 0.1 neutron per proton, thus the neutron yield is much lower compared to the fission and spallation sources. Nonetheless, a powerful high flux HiCANS has the potential to replace current medium flux reactor-based neutron sources and is a possible alternative to spallation sources. On the one hand, the lower primary ion energy in HiCANS compared to that of spallation sources with ≥ 1GeV, reduces the expense of the accelerators as well as less high energy neutrons and less secondary background. Consequently, the shielding volume is smaller and the assembly of the target-moderator-reflector (TMR) (i.e. the target station) is very compact. Thus, neutron instruments can be installed closer to the moderators because of less shielding. In general, a larger fraction of neutrons which are useful for instruments can be extracted and thus provide a high neutron flux even though the total number of neutrons generated in HiCANS is lower than spallation sources.

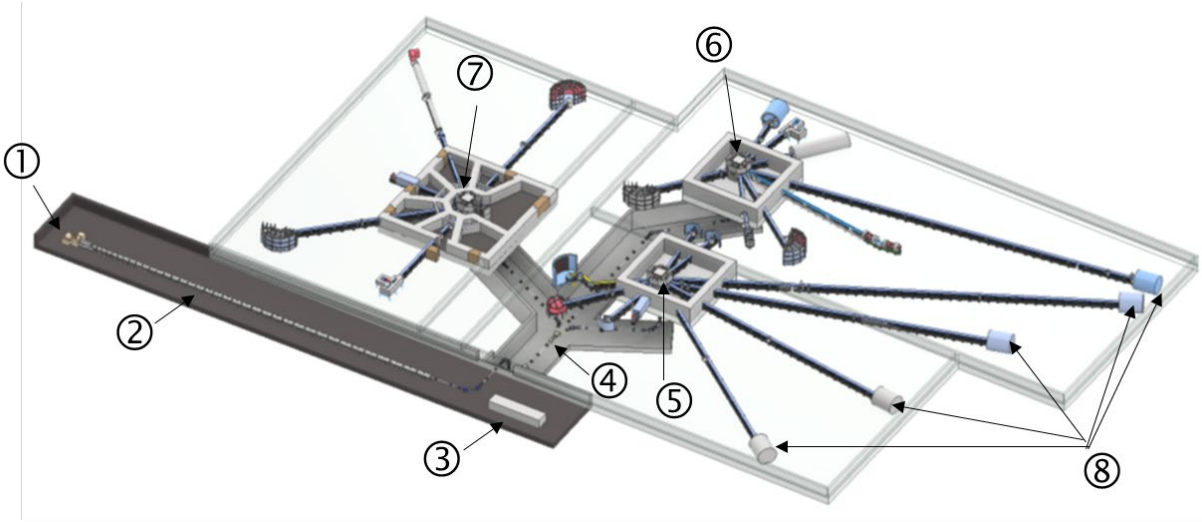

Figure 1. 1 Schematic layout of the HBS facility. 1: Ion source, 2: Linear accelerator, 3: Beam stop, 4: Proton beam multiplexer, 5: 96 Hz target station, 6: 24 Hz target station, 7: 96 Hz target station, 8: Instruments. The image is taken and adapted from [27].

A schematic layout of the HBS facility with central components is shown in Figure 1.1. The HBS facility is driven by a 70 MeV pulsed proton linear accelerator with 100 mA peak current and 1.43% duty cycle. (Note, duty cycle is the ratio of time the beam is ON compared to the time the beam is OFF.). The accelerated protons are transported to three target stations operated with frequencies of 24 Hz and 96 Hz. This is done by transferring the protons to the basement where the multiplexer is installed to unravel the interlaced proton pulse structure and to distribute the individual pulse

sequences separately to the specific target stations on the ground floor. The accelerated protons bombard bottom side of the tantalum target to produce neutrons so that instruments can be placed all around. The neutrons at HBS are mainly produced via nuclear ^{181}Ta (p, xn) W reactions when accelerated protons impinge on the solid tantalum target. Generally, most neutrons from the nuclear reactions are generated with a kinetic energy in the MeV range. Afterwards, the neutrons will be moderated to the required energy range according to the specific instruments, typically between 1 meV to 1 keV.

In order to ensure a stable long-term service life and a high neutron yield, the HBS facility needs to be optimized throughout all subsystems ranging from the ion source via the target-moderator-reflector unit to the individual instruments. This requires that all core components be properly designed, which is especially true for the target, one of the core elements of neutron generation.

1.2 Overview of the target development

Targets made of lithium, beryllium, vanadium, carbon, and other low-Z materials with simple shapes like a small piece of rectangular or cylinder are commonly employed in conventional particle accelerators to generate neutrons. The different approaches are pursued by different projects. For example, a rotation beryllium target disk cooled by water is designed by ESS Bilbao [28]. Analogously, beryllium is also selected as the high temperature target (400-500 °C) at CEA Paris-Saclay in France [29]. However, a beryllium target subjected to an intense proton current has the issue of hydrogen embrittlement. B. Bayanov etc. [30] used a thin solid lithium disk as the neutron-generating target and its opposite side is cooled with turbulent flow of water. While lithium is a kind of very reactive metal forming compounds immediately upon exposure to air and its melting point (180.5 °C) is easily reachable to cause the problem of the formation of bubbles under or within the compounds at the metal interface, resulting in decreasing significantly the target lifetime. D. Petrich etc. [31] adapted a high temperature lithium compound lithium fluoride with a higher melting point (842 °C) for a better thermal performance but lost some efficiency in terms of neutron production. The Soreq Applied Research Accelerator Facility (SARAF) [32 - 34] in Israel selects the liquid lithium flow as the target, which perfectly avoids the cooling problem but having the technical challenge to create the large volume power densities (>1MW/cm^3) by a

narrow Gaussian beam in such a design. Moreover, a microchannel lithium target with liquid Galinstan (Ga68In21Sn11) cooling was developed for neutron production in the LENOS project [35], the combination of microchannel and metal cooling solves the heat dissipation problem. But as mentioned before, lithium has a low melting point and also its thermal conductivity and tensile strength are pretty low. Besides, one investigation [36] suggests that different materials are preferable for different ion energy ranges. For example, the low-Z materials, Be and V, generate more neutrons at proton beam energies below 20 MeV. However, for the ion-energy is above 50 MeV, high-Z materials e.g., Ta and W, are preferable [36]. For the HBS project, tantalum has been chosen as the target material. The details will be introduced in section 3.1 Material selection.

1.3 Outline of this thesis

Within this thesis, a reliable neutron producing microchannel tantalum target that minimizes hydrogen implantation and features a powerful cooling system was developed, manufactured and tested successfully for the HBS project. A high flux test with a high-density electron beam was performed using the first target design in order to estimate the critical heat flux of the microchannel structure. Based on that, an optimized target with a new microchannel arrangement was developed through a fully optimization both from neutronic and mechanical aspect. Correspondingly, the extent of particle transport properties in the target are examined with Monte Carlo programs, namely FLUKA (FLUktuierende KAskade). FLUKA simulations focus on the energy deposition, particle fluence, proton implantation, atom displacements and (p, n) reactions. And the mechanical and thermo-mechanical performance of the target are checked with the industry-leading tool ANSYS (Analysis of Systems) 2022 R2 Workbench system. The predominant qualities include temperatures, pressures, heat fluxes, stresses and strains under steady and unsteady state condition. Furthermore, the optimized target prototype has been fabricated successfully with electrical discharge machining (EDM). And the machining-errors have been measured with computed tomography and the impacts of the manufactured-related tolerances on the neutronics performance of the optimized target have been estimated.

The outline of this thesis is:

Chapter 1 introduces the concept of HBS project and presents the current development state of the core component neutron-producing target.

Chapter 2 explains the theoretical background of nuclear physics, heat dissipation and mechanical properties of the neutron-producing target. Correspondingly, this chapter also elucidates the numerical methods FLUKA and ANSYS which are used in this work.

Chapter 3 describes why tantalum is chosen as the target material for the HBS project and clarifies why a microchannel structure is adapted and why the microchannel structure needs to be optimized. This chapter also displays the first target design which results from optimization between reducing thermal load and mechanical load.

Chapter 4 illustrates the high heat flux test of the first design from target manufacturing, experimental setup, IR camera calibration and estimation of critical heat flux of the target.

Chapter 5 depicts the optimization of particle transport properties of the first target and presents the relevant particle transport properties of the optimized target, for example, Bragg curves, energy deposition, proton implantation, neutron production and Displacement Per Atom (DPA).

Chapter 6 presents the design and cooling circuit of the optimized target. Besides, this chapter also shows the mechanical and thermal-mechanical properties of the optimized target in steady state and pulsed operation condition.

Chapter 7 describes the manufacturing of the optimized target via electrical discharge machining (EDM) and the examination of machining error through computed tomography test and optical microscope test. And the effects of machining errors on the particle transport properties of the optimized target are also presented.

Chapter 8 summarized the outcome of this thesis and evaluates the outlook concerning the continuation and further improvements of this work in the future.

2 Theoretical and numerical methods

The target integrity is affected by the bombardment with the high-energy protons from both microscopic and macroscopic aspects. With respect to particle transport properties, series of interactions occur and subsequently particle characteristics change. For instance, some protons react with Ta nuclei to produce neutrons, e.g. ^{181}Ta (p, xn); ionizing radiation; atomic displacements; the kinematics of particles varies due to propagation and particle-particle or particle-nucleus collisions; partial protons undergo scattering events or are absorbed and so on. On the other hand, these microscopic processes which take place due to the bombardment of high energy ions can have a significant effect on the macroscopic characteristics of the target. High heat load released in the target on account of the nuclear reactions causes target temperature going up and the temperature gradients further lead to thermal stresses and strain. Besides, target atoms are transmuted into other atoms through nuclear reactions, which could alter target compositions and subsequently affect the material performance, e.g. yield strength and thermal conductivity. Moreover, the injected protons stopping inside the metal tantalum could catch electrons to form hydrogen and to result in hydrogen embrittlement and blistering issues.

For a maximized benefit and also a prolongation of the target's lifetime it is essential to understand the underlying physics and mechanisms of the particle transport and to develop mitigations. Therefore, this chapter elucidates neutron-producing reactions at the HBS and macroscopic effects that can endanger the integrity of the target and the information on all the numerical methods and principles applied in the simulations. There are two simulation tools mainly used in this thesis, which are respectively FLUKA for particle transport characteristics and ANSYS for mechanical and thermo-mechanical simulations. For each code the frame conditions of the performed simulations, important parameters are given in chapter 5 and 6 correspondingly.

2.1 Nuclear reactions

Nuclear reactions are defined as processes where two nuclei, or a nucleus and an external subatomic particle such as an electron, photon, or muon, collide to produce one or more new

nuclides [37]. Principally, more than two particles colliding can happen in a reaction. However, the probability of three or more nuclei to meet at the same time and the same place is exceptionally rare. The content of this section will be only focused on the typical nuclear reactions involving two nuclei. If two nuclei collide with each other but separate without altering any nuclide's character, the process is called nuclear scattering instead of nuclear reactions. Only the cases where interacting particles are transformed into a completely new set of particles, is referred as nuclear reaction. Nuclear reactions are stochastic quantum processes, and any nuclear interaction's products can only be characterized by a set of statistical probabilities for a large number of potential possibilities, each of which is referred to as a reaction channel [38]. The possibility for a specific nuclear reaction is dependent on the energy, the flux of the incident particles and the corresponding cross section σ of the channel. There are two typical scenarios for nuclear reactions. The first one is direct reaction [39], where projectile and target are within the range of nuclear forces for the very short time allowing for an interaction of a single nucleon only. The time for the reaction is in the order of 10^{-22} s. The other type is the so-called compound nucleus reactions [40], where projectile and target are within the range of nuclear forces for the time allowing for a large number of interactions between nucleons. These collisions lead to a complete thermal equilibrium (equal energy partition between nucleons) inside the compound nucleus. Since energy equilibration requires time, the compound nucleus reactions are approximate 1000 times slower than direct reactions. The compound system releases energy by emitting neutrons, protons, α particles and γ-rays and has a lifetime in the order of 10^{-19} s. In any case, the bombarding particle must have enough energy to get close enough to the positively charged nucleus to be within the strong nuclear force's range.

In high-current compact accelerator-driven neutron sources, for example HBS with a tantalum target and projectile protons, the neutron product actually involves plenty of nuclear reactions. The probability of each nuclear reaction depends on the energy of the nuclei, which is influenced by the target's environment, including the material and the corresponding geometry. In addition to the primary reactions, some secondary nuclear reactions can be triggered by the byproducts of earlier nuclear reactions. Thus, in order to evaluate the nuclear reactions, particle transport and other microscopic processes in the target, Monte-Carlo simulations need to be performed with for instance FLUKA [41- 44].

2.2 Heat dissipation

The knowledge of heat transfer processes and heat dissipation is critical to a successful target design. It helps to determine the maximum power and the safety margin at which the neutron-producing target can be fully utilized and operated stably and reliably. Broadly speaking, there are two factors determining the maximum power density that the target can withstand: (i) target material; (ii) cooling capacity. On the one hand, the physical properties of the target material heavily determine the upper limitations which the target can be able to bear with regard to thermal stresses. For instance, concerning the brittle materials like graphite and some alloys with extremely low strength, cracks can emerge without plastic deformation and can quickly progress into brittle breakage. When materials are used with low melting points, the target may be melted even for higher strength. On the other hand, thermal stress is easily trigged when applying a high-power density to a target with a poor thermal conductivity resulting in a significant temperature gradient between the target's top and bottom surfaces. Responding to this problem, a sufficient heat dissipation and conductivity can efficiently alleviate thermal stresses or compensate the limitation of thermal conductivity of target itself to a certain extent.

At the HBS facility, 100 kW heat load is planned to put on a target surface of 100 cm^2 for a high neutron yield, i.e. the power density is up to 1 kW/cm^2 and furthermore the total beam power is deposited inside the target and converted to heat which needs to be removed efficiently. Since a microchannel structure has been largely considered one of the best solutions to dissipate high specific power [45], this work adapts this concept to dissipate heat in the HBS target. Generally, the heat transport dominantly proceeds through two steps: the first one is heat conduction through the solid, the other one is the forced convection from the inner wall of the cooling channel to the cooling medium.

2.3 Mechanical properties

Mechanical properties of materials are quantities that reflect the relationship between its response to or deformation from an applied load or force [46]. The mechanical properties of metals determine the range of usefulness of a material and define the service life that can be expected.

The mechanical properties are also used to help to classify and identify material. It is essential for engineers to acquire the knowledge of the mechanical properties in order to adapt suitable materials for different demands in various structures or components. The majority of a metal's mechanical properties are typically stated in terms of strain, stress, or both. For a high-power density metal target at the high-current accelerator-based neutron sources, the most important mechanical properties include a suitable combination of properties such as high thermal conductivity, low thermal expansion coefficient to reduce thermal and particularly fatigue stress as well as good elasticity and ductility and high yield strength to act as a solid target. These properties are critical since the target must tolerate a wide range of temperature variations and stress.

2.4 Particle transport simulation code-FLUKA

Particle transport simulation code, FLUKA, is a fully integrated particle physics simulation package, which is widely used in many applications from target design to accelerator shielding, activation, dosimetry, detector design, neutrino physics and radiotherapy and so on. FLUKA can simulate with high accuracy the nuclear reactions as well as the particle transport and interactions with matter. The cross-sections for all simulations are taken from “Evaluated Nuclear Data File” (ENDF/B-8R0) [47] and “Japanese Evaluated Nuclear Data Library” (JENDL40-HE) [48]. The cross-sections in nuclear physics is the area around the nucleus facing a beam of incident particles, within which the incident particles will interact with the nucleus, and outside of which the particles will penetrate the material without interacting with the nucleus [49].

In this present work, FLUKA is used to optimize the particle transport properties of the target. For example, proton flux, energy deposition, the spatial distribution of (p, n) reaction events and the spatial distribution of proton termination. Before simulations, a realistic model of the environment surrounding the target should be established firstly. The whole geometrical setup is specified by the bodies and regions. The former one describes the type, size and location of the basic units of the geometry, the latter one is constructed by combining the bodies with different Boolean operations, i.e. union, subtraction and intersection. The property of different regions can be assigned with existing or defined materials. The whole geometry must be surrounded by ideal vacuum in order to start the primary particles outside the physical geometry. All the regions have

to be contained in a closed blackhole so that all escaping particles are absorbed. These boundary conditions are applied for all the simulations in this work.

2.5 Engineering Simulation Software- ANSYS

Analysis of Systems, which is called ANSYS, is a general-purpose, finite-element modeling and multi-physics engineering simulation software for numerically solving a wide variety of mechanical problems in product design, testing and operation [50]. It is widely used to determine how the products perform with different specifications and operation conditions without fabricating prototypes of the products or conducting destructive tests. For example, the results can be used for analyzing the strength, elasticity, toughness, temperatures, pressures, heat flux, fluid flow and other properties to predict the lifetime of structures and engineering components. The main processes of ANSYS simulation include 6 steps: building geometry, implementing boundary conditions and material properties, defining ANSYS models (turbulence or laminar flow), generating mesh, obtaining solution and presenting results. All the ANSYS simulations in this thesis are performed using the ANSYS 2022 R2 Workbench system, which is a common platform for solving engineering problems.

The dimension of the required component of the target are obtained from FLUKA optimization. The target model for the ANSYS simulations is produced with Space Claim [51], which is the default 3D modeling platform under Ansys Workbench. The relevant materials used in the simulations are tantalum and water under atmospheric pressure. The material properties can be customized specifically according to user requirements. Ansys Workbench [52] also owns a database for most commonly used engineering materials regarding plenty of properties, such as density, thermal conductivity, dynamic viscosity, elastic modulus, yield stress and so on. Therefore, most of the material properties of tantalum used in this work were taken from the database. However, the pertinent properties concerning coolant water are adapted from IAPWS [53] since the water in microchannels may involve phase transition from liquid to steam. The different states of water can lead to a huge difference in the heat dissipation capacity of microchannel structure. The specific parameters of the material properties for tantalum and water are listed in Table 6.1 in

chapter 6. After the material properties are set and the target geometry is created, the next step is to mesh the model and adding the boundary conditions. The last step is to run the simulations.

3 HBS target

Within the framework of the Jülich High Brilliance Neutron Source (HBS) project, a high-current accelerator-driven neutron source (HiCANS) has been developed to produce highly brilliant neutron beams to feed a variety of neutron instruments. Such a Hi-CANS should not only have a high neutron yield, but also have a stable long-term service life. This requires all the core components to be designed properly. One of the key components as well as the main power-limiting factor is the neutron producing target that releases free neutrons from the impinging ions via nuclear reactions with an energy well below the spallation threshold. The main parameters of the HBS target are summarized in Table 3.1 [54, 55].

Table 3. 1 Main parameters of the HBS target [54, 55].

Target material	Tantalum
Particle type	Proton
Particle energy	70 MeV
Peak current	100 mA
Duty cycle	1.43%
Average power	100 kW
Power density	1 kW/cm^2
Peak power	7 MW
Neutron yield	1.45×10^{15} s^{-1}

At HBS, the accelerator delivers proton currents of 100 mA and 70 MeV energy with a duty cycle of 1.43% to impinge on the target. As a result, lots of protons accumulate in the tantalum target due to the high proton current of 8.74×10^{15} s^{-1} [55], which can cause hydrogen embrittlement and blistering problems. Over time, protons resting inside the tantalum target will trap electrons and thus form atomic and molecular hydrogen, which eventually accumulate into hydrogen bubbles. The hydrogen atoms inside the target are so small that they can penetrate into the solid tantalum and form brittle hydrides, or lower the stress required for crack generation and extension in the tantalum, leading to embrittlement [56]. On the other hand, atomic hydrogen diffusing through the

tantalum target may collect at internal defects like inclusions and laminations and form molecular hydrogen. High pressures may be built up at such locations due to continued absorption of hydrogen leading to blister formation, growth and eventual bursting of the blister [57]. In order to avoid these problems, a geometry where the thickness of the target is reduced to be slightly thinner than the penetration depth of 70 MeV protons is chosen, so that most of the protons impacting end up dumped in a water sink ("proton pool") on the backside of the target, which is called "beamstop". The other potential issue endangering the target integrity is thermal stresses due to the large volumetric heat load release in a small target volume. For this a reliable cooling should be guaranteed for the target during the operation in order to avoid local hot spots due to overheating. Correspondingly, an optimized internal cooling microchannel structure with sufficient cross-sectional area of channels to dissipate heat is proposed. The cooling substance chosen in this work is the light water, which is not hazardous and can be obtained in unlimited quantities. On the one hand, water has a very good heat capacity, high density and a wide temperature range in the liquid phase, which results in being effective in heat dissipation. On the other hand, water is easy to handle. It is hardly activatable compared to metals and it is easier to be sealed compared to gases. Besides, no corrosion occurs when tantalum is in contact with water under irradiation [58]. Another problem is that heat deposition in the target is not homogeneous as protons have different penetration depths in tantalum and water, which leads to temperature gradients and then thermal stresses. For this, a microchannel structure which can produce a homogeneous energy deposition should be determined. Therefore, to engineer a reliable target it is necessary to develop a design that minimizes hydrogen implantation and produces homogeneous energy deposition within the target and features a cooling system that efficiently removes heat.

3.1 Material selection

A careful material selection is thus made firstly in order to engineer a reliable target. There are several key factors that the material selection influences for neutron producing target like neutron yield, mechanical properties and machinability. The neutron yield due to nuclear reactions of ions with the target material is an important parameter to evaluate the efficiency of such a source since it can have a direct impact on the brilliance of neutron beams. Hence, the investigation of neutron yield for different target materials impinged with protons at varied energies is inevitable during

the design process of target. Such a systematic study has been conducted in [36]. The main result presented in Figure 3.1 shows that the relation of the neutron yield with the atomic number Z of the target material and the energy of the primary proton. It indicates the neutron yield increases with the increasing energy of the proton for all target materials in the range of atomic number from 1 to 82. Furthermore, a neutron yield up to 10^{15} n/s can be achieved when the proton energy is higher than 70 MeV for the heavy elements of the atomic number being $70 < Z < 82$. Among the high-Z materials, Tungsten is a non-reactive material, which endo-thermally dissolves hydrogen. In contrast, the solution of hydrogen in tantalum is an exothermic process. Hence, tantalum has a higher hydrogen solubility (0.76 H/M at 100 °C and 1 bar [59]) compared with tungsten (1.3×10^{-19} H/M at 100 °C and 1 bar [60]). Here the hydrogen solubility is expressed as the atomic ratio of hydrogen (H) to metal (M) at 100°C and 1 bar. Correspondingly, tantalum can accumulate large amount of hydrogen and the blistering threshold is up to 0.17 H/M at room temperature and 1 bar [61, 62]. The capacity of tantalum to store large amounts of hydrogen inhibits blistering and thus increases the life of the target. Besides, tantalum possesses excellent thermal performance and mechanical properties, especially pure tantalum displays excellent ductility even after irradiation [63]. Therefore, tantalum has been chosen as the target material for the HBS project.

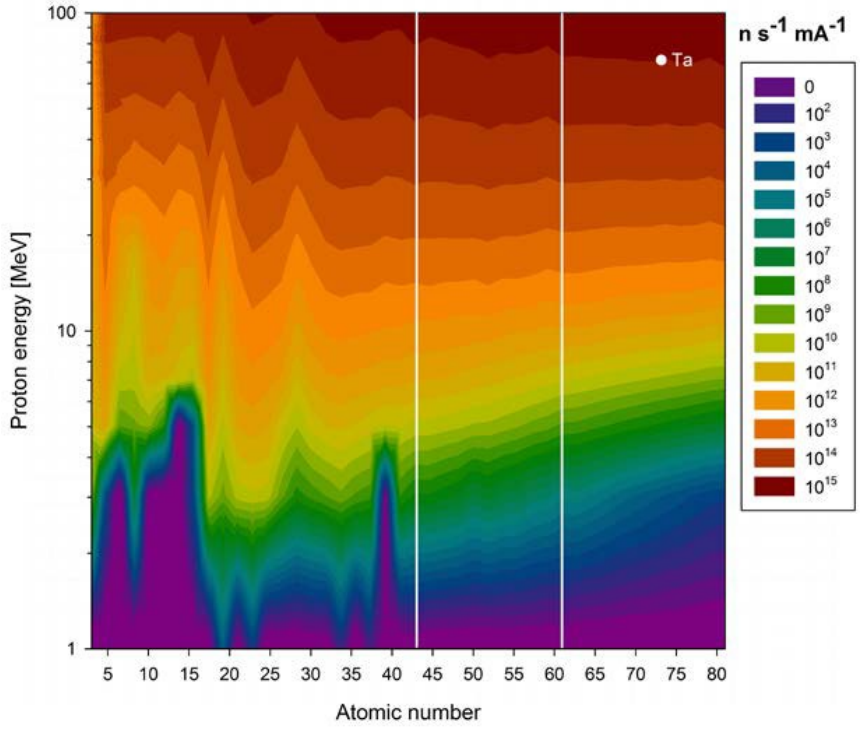

Figure 3. 1 Proton induced neutron yield for various target materials determined from the cross sections calculated with the TALYS nuclear code [64] and the stopping powers calculated with SRIM [65]. White lines: Tc and Pm, white dot: Ta at 70 MeV. Taken from [36].

3.2 Microchannel structure

The HBS target must be designed properly to ensure a safe and stable operation at 100 kW. The main risks endangering the target integrity are hydrogen embrittlement and mechanical stresses. In spite of the selected target material tantalum having a good capacity to store large amounts of hydrogen, the HBS target is designed to be slightly thinner than the penetration depth of 70 MeV protons to minimize proton implantation within the tantalum to reduce further the risk of hydrogen embrittlement. Consequently, most protons impinging are ultimately dumped into a dedicated water sink ("proton pool") behind the target at the distance of the Bragg peak. The water sink is simply called "beamstop" in the following content. The details of the determination of the target thickness will be described in chapter 5.

Most mechanical stresses are induced by the water pressure and temperature gradients. A solid thin target in combination with the enormous heat loads induced by the high-power proton beam generates strong temperature gradients within the target. Hence, a reliable cooling must be guaranteed for the target during the operation in order to avoid local overheat spots and to reduce mechanical stresses. The different cooling concepts are summarized in Table 3.2 [54]. It indicates that the achievable power densities of the traditional water-cooling methods with or without a heat sink are quite small. Even though the liquid metals coolant can boost the heat dissipation capacity, it is still below 1 kW/cm^2. However, the microchannel structure exhibits a promising cooling efficiency for water and liquid metals as coolant. P. Mastinu et al. [66] proved that a microchannel structure with water coolant was able to remove heating up to 3.5 kW/cm². The main cause for this is that the microchannels minimize the viscous boundary layer so that the thermal resistance at the interface between the coolant and walls is minimized correspondingly. Consequently, in this work we utilize an internal microchannel cooling structure to remove large volumetric heat load from a small target volume.

Table 3. 2 Cooling capabilities of various cooling methods. Taken from [54].

Method	Coolant	Heat transfer coefficient [W/m^2/K]	Achievable power density [kW/cm^2]
External forced cooling	Water	4000 – 16000 [68]	0.13
	Liquid metals		0.26
External heat sink	Water	4000 – 4700 [69]	0.2 – 0.4
	Liquid metals		0.4 – 0.8
Microchannels	Water (1-phase)	10000 [70]	0.2 – 3.0 [71]
	Water (2-phase)	100000 [70]	3 – 380 [72]
	Liquid metals		1 – 3.5 [73]

The basic concept of a metal target with an internal microchannel cooling structures shown in the schematic drawing is depicted in Figure 3.2. The gray part shows the solid tantalum, and the white microchannel structures are filled with water. A “fin structure” is adopted to increase the cooling surface contact area in order to efficiently dissipate the entire heat via the water coolant. The target consists of several individual microchannel structures as shown in Figure 3.2 instead of a long

microchannel structure through the entire target width, which minimizes bending stresses caused by the static pressure of water. The solid tantalum parts between these single microchannel structures are abbreviated as “bridges” in the following texts.

The arrows in Figure 3.2 represent some straight paths of protons inside the target. They show the protons of different paths traveling through different amounts of tantalum metal and water. For example, the protons crossing the bridge sections only travel through tantalum (like “C” and “D”), but some protons traversing the microchannel structures go through the paths containing tantalum and water (like “A” and “B”), which results in the distribution of stopped protons being inhomogeneous due to protons having different penetration depths in tantalum and water. Correspondingly, the heat deposition in the target is also inhomogeneous. Furthermore, the protons stopped within the tantalum target can catch electrons and thus form atomic and molecular hydrogen and finally accumulate to hydrogen gas bubbles, which can lead to blistering and subsequent a change of the metal matrix. In order to avoid these issues, some tantalum in the bridge sections should be removed to match with the microchannel structures owing water and tantalum, which can be depicted as in Figure 3.3. The grooves at the top side in Figure 3.3 show some tantalum cuts from the top surface of the target. In addition to the bridge sections, even for the protons impinging at the same individual microchannel structure, the amounts of water and tantalum in different paths are also different. For instance, some protons only travel through the main horizontal channel (like “B”) but some also go through the fins in addition to the main channel (like “A”). Therefore, a proper microchannel structure which can minimize proton accumulation within the tantalum target to reduce blistering problems and also to produce a homogenous energy deposition inside the target to minimize mechanical stresses, needs to be developed.

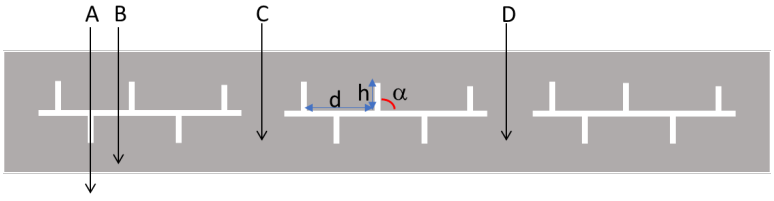

Figure 3. 2 The schematic of a metal target with microchannel cooling structures. (Arrows show the straight paths of the incident protons; the ends of arrows represent the positions of terminated protons).

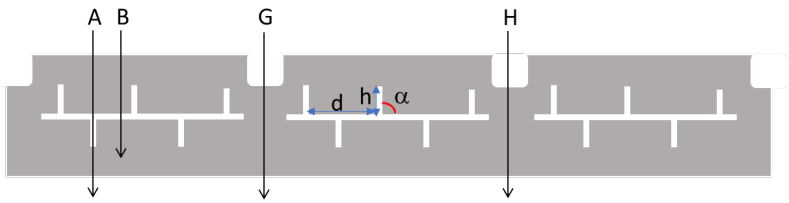

Figure 3. 3 The schematic of an adjusted metal target with microchannel cooling structures. Arrows show the straight paths of the incident protons; the ends of the arrows represent the positions of terminated protons; recess on the top surface showing the removal of some tantalum.

The straight trajectories of protons depicted in Figure 3.2 and Figure 3.3 are the ideal situation. The realistic physical paths of impinging protons are far more complicated than that because of the collision with electrons or target nuclei. Usually, the protons are forced to deviate from the straight track after a collision and the paths become more scattered. Therefore, this work adopts the particle transport code FLUKA as the investigation tool to simulate the process of protons bombarding the tantalum target to determine a proper microchannel structure. The details of the investigation and the resulting microchannel design will be presented in chapter 5.

3.3 The first target design

The main design philosophy of the HBS target is to be compact and stable. The brilliance of neutron beams, defined as neutrons per source area, wavelength band, time interval, and solid angle, is one of the figures of merit of the HBS and is inversely proportional to the size of the target, i.e. a smaller target size increases the brightness of the neutron beam. The neutron yield is approximately proportional to the target thickness until it's beyond the penetration depth of the protons. In the meanwhile, the target dimension is also limited by the thermal stresses and heat dissipation capacity. Enormous heat release generated by protons takes place at a small volume of the target, which results in temperature gradients. As a result, harmful thermal stresses arise inside the component. To avoid this issue, a reliable heat dissipation capacity must be ensured.

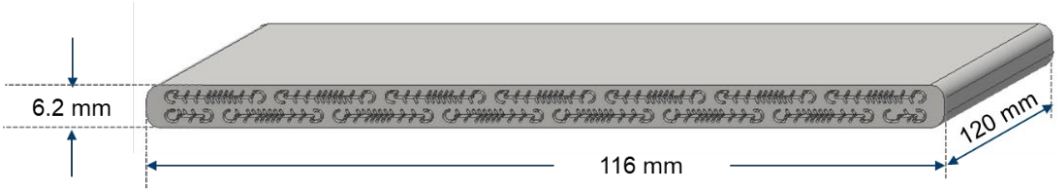

Figure 3. 4 The schematic of the first target with microchannel structures. Taken from [74].

Therefore, based on the above guiding principles, the first target [54] with a microchannel structure was developed, which is the result of optimization between thermal and mechanical load reduction. The basic structure of the first target is shown in Figure 3.4. The irradiated area of the rectangular target is 100×100 mm^2 and the thickness is 6.2 mm. The microchannel structures called "fishbone" are used to remove heat loads. The width of the microchannels is chosen as 0.35 mm since the previous studies indicate this value is a good compromise between heat dissipation capacity (a high heat transfer coefficient of 17.000 W/m^2/K with 8 m/s coolant velocity) [54], pressure loss and the manufacturability. Figure 3.5 presents the first target fabricated via wire erosion.

Figure 3. 5 The first microchannel target fabricated via wire erosion [74].

4 High heat flux tests of the first target

As mentioned before heat dissipation capacity is one of the main limitation factors during the development of the HBS high-power density neutron producing target. Hence, a high heat flux test with an electron beam was performed at the test facility JUDITH II [75] at IEK-4 of the Forschungszentrum Jülich to check the heat removal capacity of the first target design. The heat flux test and CFD simulations in this chapter were performed by Johannes Baggemann of the HBS team at JCNS-2 of the Forschungszentrum Jülich. The test results show that the first target can withstand a power load of 100 kW and that the microchannel structure can provide adequate cooling of 1 kW/cm^2.

Although there is a big difference between electron heating and proton heating, the heat load test at JUDITH II facility can still examine the heat dissipation efficiency validly. Figure 4.1 shows two exemplary temperature distributions for the first target of electron and proton heating from CFD simulations, respectively. Most of the simulation parameters remain the same in both cases, where the target thickness is 6.4 mm and the heat flux is set to 1 kW/cm^2, which is consistent with the maximum surface power density of the HBS specification. The proton or electron beam impinges the target from top in both simulations. The only difference is the dimension of the heat source. For electron heating, the entire heat source is deposited close to the target surface. For proton heating at the HBS operating case, the heat release is approximated in the entire target volume according to the stopping power of 70 MeV protons in Ta obtained from FLUKA simulations (see Figure 5.4). The energy is normalized so that a total of 100 kW is released on 10 cm×10 cm×6.4 cm. According to Figure 4.1(a), the highest temperatures occur at the target surface, as most of the heat is deposited on the target surface, due to the fact that the penetration depth of electrons in matter is typically about 1 to 5 μm [76]. Fig.4.1 (b) indicates the temperature distribution of the target heated with protons. Instead, the highest temperature occurs at the end of the target, which corresponds to the Bragg peak where the proton loses its maximum energy [77]. In this situation, the entire interfaces of the microchannels participate in the cooling for the case of proton heating. For electron heating, only approximately one third of the microchannel

interfaces contribute the cooling. All in all, the high heat flux test with electron beam at JUDITH II is a very conservative test.

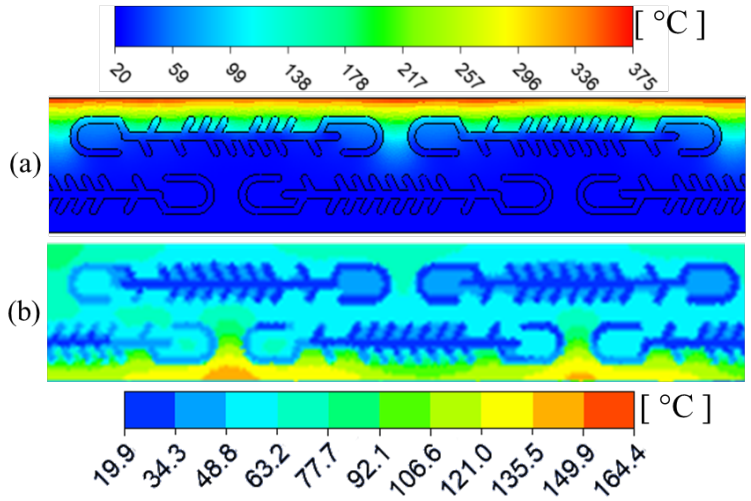

Figure 4. 1 Temperature distribution from CFD for (a) electron heating and (b) proton heating [74].

4.1 Manufacturing and testing setup

The tested component of the first target is made out of one single piece of tantalum and the microchannel structure is produced by wire erosion at the JCNS workshop of Forschungszentrum Jülich. The fabricated target for the heat flux test consists of three parts, the main body in the middle and cooling tubes on both sides, which is shown in Fig.4.2.

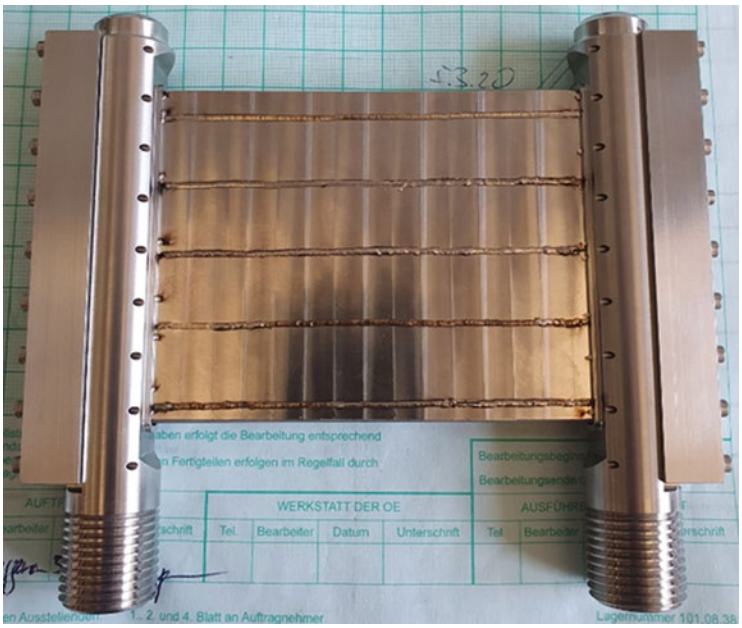

Figure 4. 2 The fabricated target for high heat flux test [74].

The high heat flux test was performed with the electron beam facility JUDITH II in the Hot Materials Laboratory of the Forschungszentrum Jülich. The facility consists of an electron beam generator with a maximum power density of 2 kW/cm^2, a process chamber with a vacuum system, an infrared camera for temperature measurement, and cooling circuits for water pressure and water flow monitoring. A schematic overview of the testing facility including arrangements of diagnostics is given in Fig. 4.3.

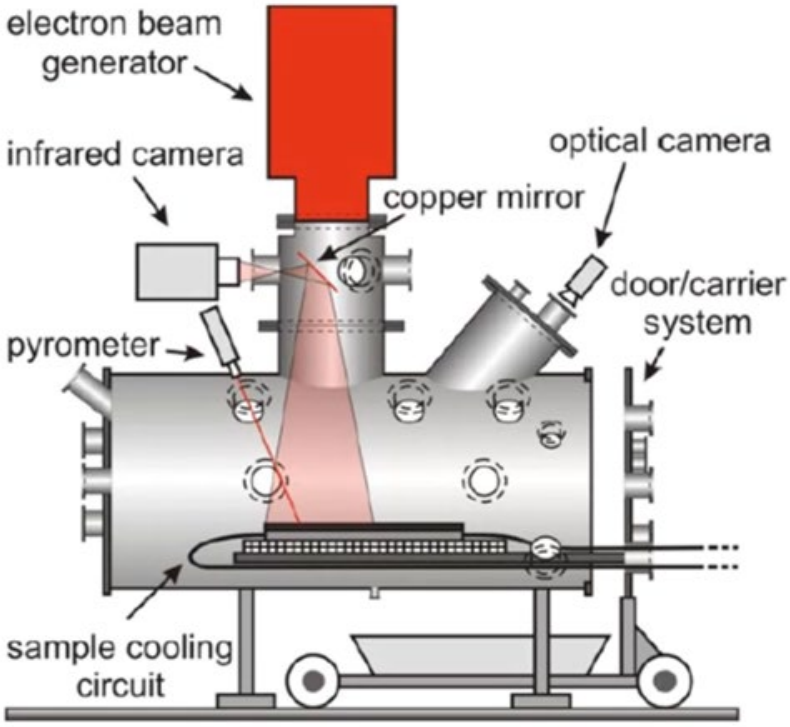

Figure 4. 3 Schematic view of JUDITH II. Taken from [75].

The beam has an approximately Gaussian shape with a diameter of 6 - 10 mm. The beam scans the target quickly and loads continuously. The target is mounted in the chamber of JUDITH II facility, which is presented in Fig.4.4. The power of the e-gun runs from 0 to 1 kW/cm^2, which is the HBS design goal. The electron beam irradiated the central area of the target with an area of 80×60 mm^2 as shown in Fig.4.5. Hence, a heat load of 48 kW was put in the target in total. During the experiment, the temperature of the target surface was constantly measured by the infrared camera. The cooling water has a temperature of 22 ˚C in an inlet. A flow rate of 54 kg/m^2/s, i.e. water velocity of 8 m/s inside the microchannels, is set for sufficient cooling, resulting in an inlet pressure of 9.5 bar and an outlet water pressure of 4.6 bar at the chamber door. This is due to the linear relationship between feeding rate and pressure of the cooling system [78].

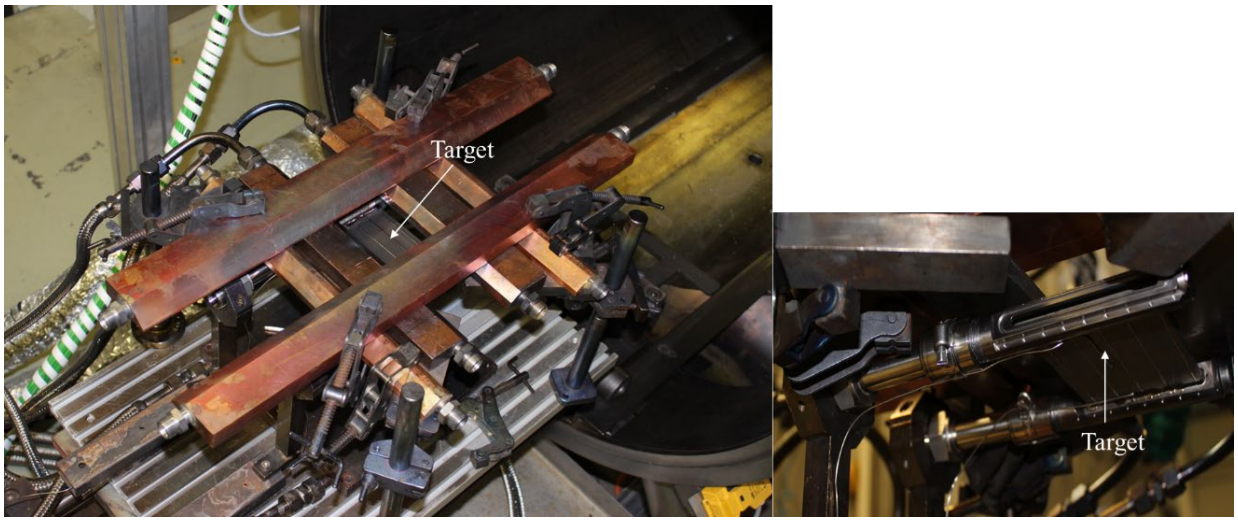

Figure 4. 4 Tantalum target mounted in the chamber of JUDITH II facility [74].

The infrared camera at the JUDITH II facility recorded four videos during the experiment, each with 3000 temperature pictures, one picture every 0.5 seconds. Each picture indicates the average surface temperature measured by the infrared camera. A pretest was performed to test the heat load when everything was set up. Afterwards, the heat load experiment for the target was conducted.

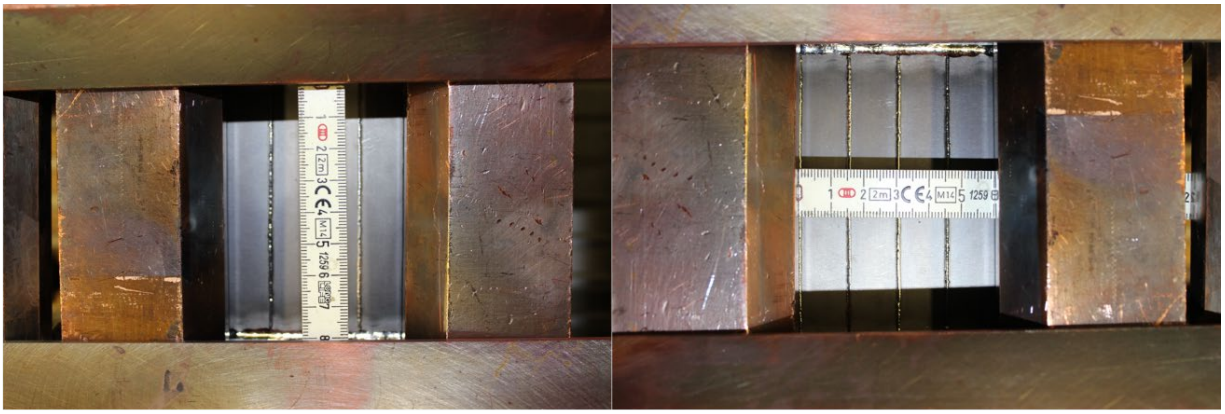

Figure 4. 5 The irradiated area of the target during the heat flux test, which is 80×60 mm^2 [74].

4.2 IR camera calibration

Infrared camera thermometry instruments are calibrated to approximate blackbody emitters. Therefore, a priori information about the emissivity of the object to be measured must be available

for non-contact temperature measurements with IR cameras. Correspondingly, the emissivity calibration of the IR-camera was performed prior to the formal high heat flux test of the target. The sample was in a vacuum insulated environment, which was directly heated to approximate 200 °C without cooling. The cool down curve as shown in Fig.4.6 was recorded with both the infrared camera (IR camera) and the thermocouple (TC) which was mounted at the bottom of the target. The orange curve represents the temperature T_{IR} measured with IR camera, which is averaged over the irradiated area of approximate 80×60 mm^2. The blue line shows the temperature T_{TC} measured with thermocouple on the target. The ΔT shown in gray curve is the difference between thermocouple and IR temperature values. It indicates that the deviation is large during heat up due to the time lag between surface temperature at the surface (IR) and retarded TC measurement at the bottom of the target. The deviation is rather low (< 10 °C) in near equilibrium condition during cool down. When the emissivity (ε) setting is adjusted to 0.12, the temperature of the target surface measured with the IR camera is closest to the temperature of the thermocouple. Since the emissivity varies with temperature, it should be mentioned that 50-200°C was used as a reference for the calibration, since at first it was expected that the target would be destroyed when heated to 200 °C. The calibration curve starts at 50 °C because the photographic temperature signal of the infrared camera is too low below 50 °C.

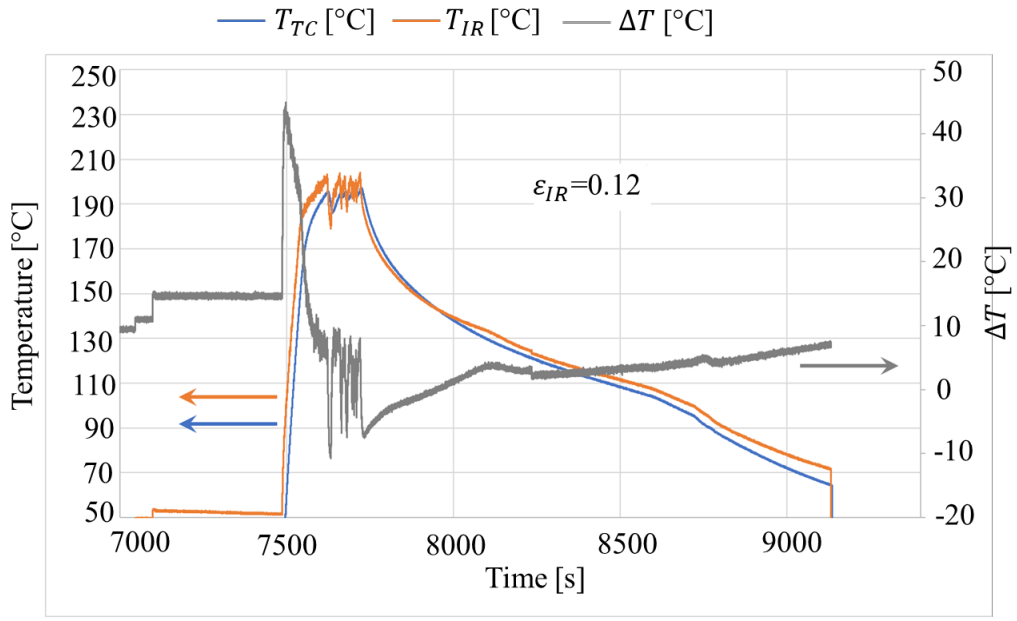

Figure 4. 6 Temperature measurements with thermocouple (TC) and infrared camera (IR) during calibration [74].

4.3 Experimental data

The formal high heat flux test is performed after the initial configuration test. All the original data during the test are exhibited in Figure 4.7. The green curve illustrates the average surface temperatures of the target T_{IR} measured with the IR camera. The blue line displays the temperature difference of the cooling water inlet and outlet ΔT_{water}. The deep blue line indicates the power density of the electron gun *L* heating target. The entire test consists of three parts. The first stage is that the electron gun heats the target uniformly with a continuously increasing power density. The average surface temperature of the target rises with the increase in heating power density. The mass flow rate of the coolant is kept at 54 kg/m^2/s in this stage while the power density increases rapidly to a higher level within 10 seconds and remains at a level to heat the target for approximately 1 minute until a constant surface temperature value is reached. The first stage ended at 1840 seconds when the average surface temperature of the target reached 250 °C and the power density was 5 MW/m². The power density then drops sharply to a lower level of 3 MW/m², and the second phase of the flow variation test begins with the power density remaining constant but the mass volume of coolant slowly dropping to 32 kg/m^2/s (i.e. the coolant velocity decreases within the microchannel) and again slowly returning to the standard cooling conditions of 54 kg/m^2/s at 5000 s. It indicates that the average surface temperature of the target varies slightly and the reduced mass flow rate has a stronger impact on the temperature difference of coolant water. The third phase is similar to the first stage, where coolant mass flow rate maintains at 54 kg/m^2/s but the heating power density is constantly increased until reaching 10 MW/m² (i.e. 1 kW/cm^2), which is the HBS design goal. As the main purpose of this chapter is the estimation of the critical heat flux of the first target design, only the experimental data of first and third stage are analyzed and discussed below.

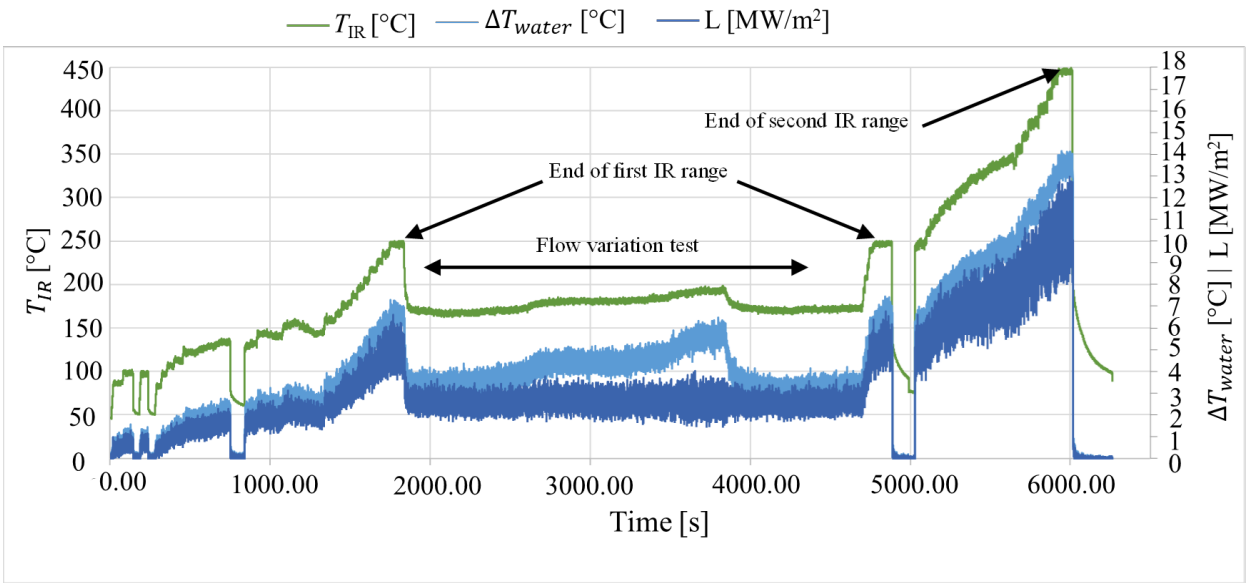

Figure 4. 7 Measurement results of the high heat flux test [74].

4.4 Data analysis

Figure 4.8 presents the comparison of partial surface temperatures of the target from the infrared camera and CFD simulations for different heat loads, (a) $q^{\cdot}$ = 0.2 kW/cm^2, (b) $q^{\cdot}$ = 0.5 kW/cm^2, (c) $q^{\cdot}$ = 0.7 kW/cm^2 and (d) $q^{\cdot}$ = 1.0 kW/cm^2. (Note. The white part of Figure 4.8(d) represents a temperature that exceeds the maximum value marked in the color bar.). The CFD simulation attempted to reproduce the surface temperature pictures of the target measured with the infrared camera. As a result, the temperature distribution of the target surface derived from the simulation contains rectangular stripes that appear regularly on the surface and at higher temperatures, similar to the temperature pictures measured with the IR camera. The reason for the rectangular stripes is that the cooling inside the target body is not homogeneous. Still, there exist some differences between IR pictures and simulation results. On the one hand, there are a number of red-hot spots in the temperature photographs taken with the infrared camera, which can make the local target surface temperature higher. In addition, other potential causes of temperature differences will be further explained in the analysis of the results in Figure 4.10.

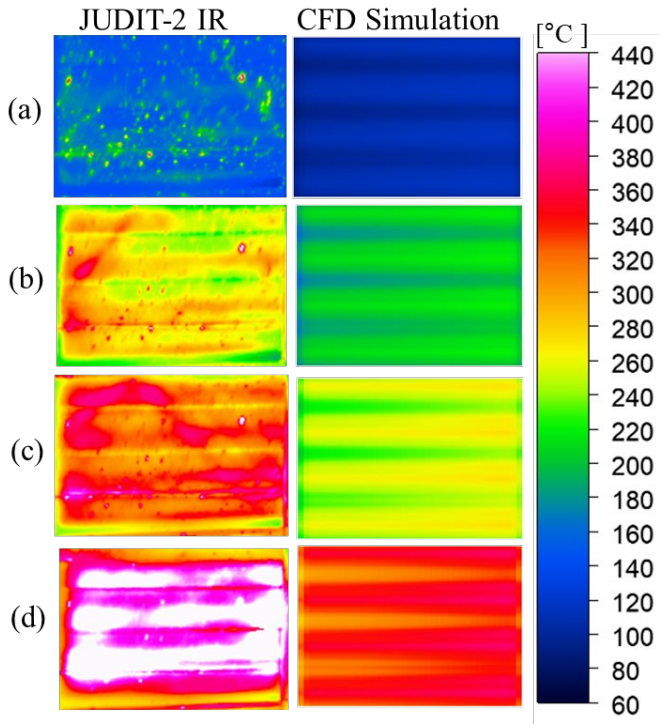

Figure 4. 8 Comparison of surface temperature of the target from infrared camera and CFD simulations for different heat loads. (a) $\dot{q} = 0.2$ kW/cm^2; (b) $\dot{q} = 0.5$ kW/cm^2; (c) $\dot{q} = 0.7$ kW/cm^2; (d) $\dot{q} = 1.0$ kW/cm^2 [74].

Taking Figure 4.9 as an example, which depicts the temperature distribution of the target surface when the heat load is 0.3 kW/cm^2. It can be seen that the target has an inhomogeneous cooling structure due to the staggered arrangement of the cooling channels. The hot green regions marked with red lines of the heat map correspond to the solid tantalum parts without any microchannel structures, which results in a bad cooling in these regions and therefore a higher surface temperature. The blue regions marked with withe lines correspond to the microchannel cooling structures, which leads to a better cooling efficiency and also a lower target temperature. The red-hot spots may be caused by dust on the target surface.

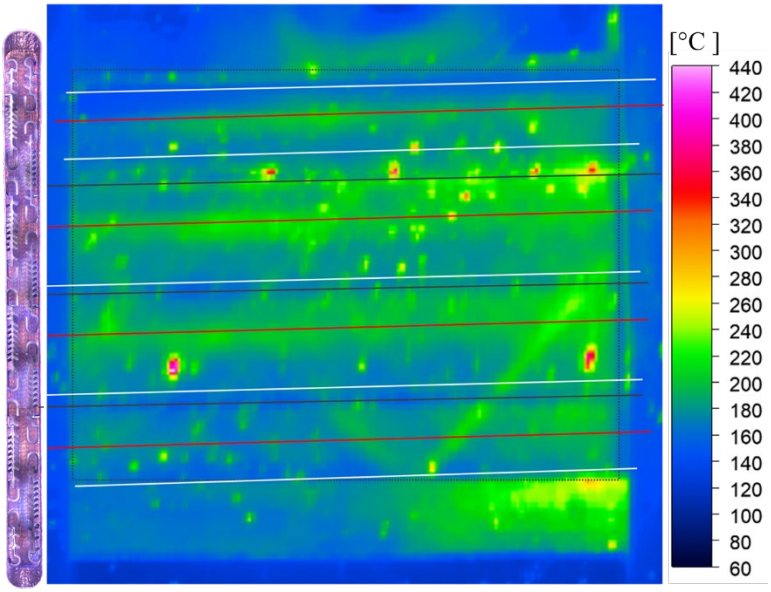

Figure 4. 9 Temperature of the target surface from infrared camera with a heat load of 0.3 kW /cm^2 [74].

Fig.4.10 describes how the average surface temperature of the target changes with the heat load increase during the experiment. The red dots in Fig.4.10 represent the average surface temperatures of the target T_{IR} which are measured with infrared camera. The experimental data in Fig.4.10 are averaged over an irradiated area of 80 × 60 mm^2 using 20 infrared photographs taken within 1 second. The red dash line is a linear fit to the experimental data. The black dots are the temperatures T_{CFD} obtained from CFD simulations used for comparisons. Analogously, the black is a linear fit of the simulation data. According to Fig.4.10, the highest surface temperature of the target is up to 450 °C for a heat load of 1.0 kW/cm^2. However, the target was not destroyed during the experiment even if the heat load reached 1.0 kW/cm^2. In other words, even if it is a very conservative heat load test, the target is able to withstand power densities in excess of 1.0 kW/cm^2. The target is able to dissipate more than 1.0 kW/cm^2 heat and the target achieves the HBS design goal. On the other hand, it can be seen that the result of CFD simulation underestimated the average surface temperatures of the target which were measured with infrared camera. There is a difference of 70 K. The potential reasons for this discrepancy are explained below.

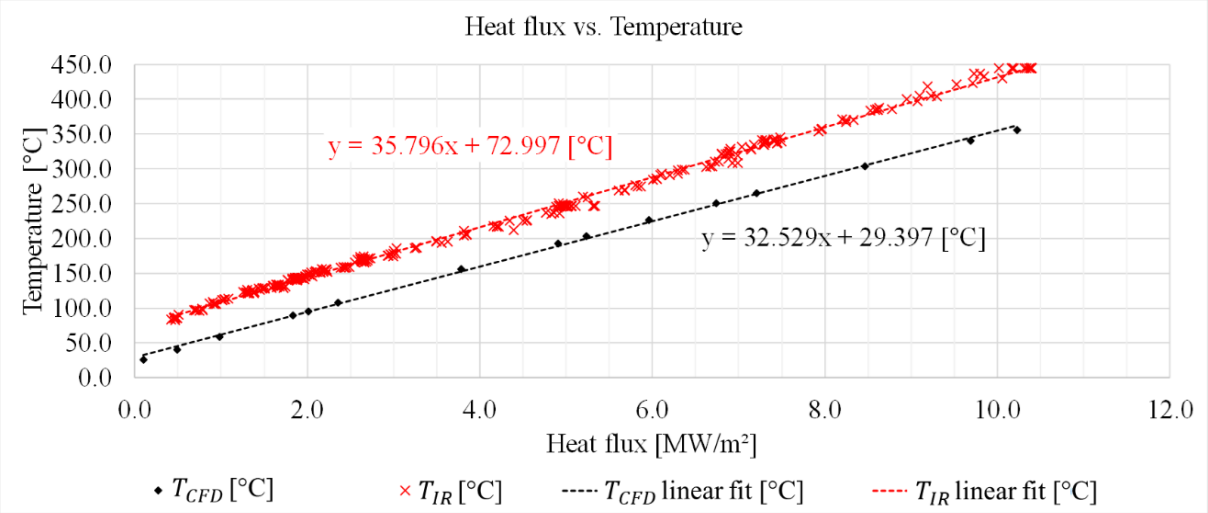

Figure 4. 10 The average surface temperature of the target under different heat loads at a vacuum pressure of 1.7×10^{-2} Pa and a cooling water velocity of 8 m/s [74].

As mentioned in section 4.1, the microchannel structures are fabricated via wire erosion [79]. The cut-wire enters into the target body from a thin seam in the surface to create the individual microchannel element. The thin seams from the manufacturing process are closed via welding after all the microchannel structures are machined. As a consequence, each of this seam welded clogged one cooling microchannel, which can cause an increase of the surface temperature by 5 K according to CFD simulation [74]. On the other hand, there exist certain machining-errors during the manufacturing process. For example, the nominal value of the distance from the channel to surface is 0.83 mm. However, the real value has an average deviation of ± 0.16 mm according to the optical measurement of the dimensions and tolerances [74]. The larger distance between the target surface and the microchannels leads to a worse cooling. According to Fourier's law [80], even a processing error of only 1 mm from the channel to the surface results in a temperature difference of 166.7 K for solid tantalum at a heat flux of 1 kW/cm^2. (Note, the thermal conductivity of tantalum used for estimation is 60 W/m/K [81]). Thus, for a larger distance of 0.16 mm in the CFD simulation, the surface temperature can be increased by 27 K. Besides, the actual diameter of the microchannel is 0.43 mm instead of the nominal value of 0.35 mm. The wider microchannels have a lower water velocity inside the channels, which results in a reduced heat transfer at the interface. As a result, the surface temperature can be increased by another 24 K [74] according to a simple conservative estimation based on the heat transfer. In total, the temperature difference

between experimental data and CFD simulations can be explained with these very conservative estimations together with the inaccuracy in the fabrication process.

4.5 Estimation of CHF

The aim of the high heat flux test is to determine the critical heat flux (CHF) of the first target design with microchannel structure and thus the safety margin in operation. CHF is the heat flux where the local heat transfer coefficient sharply goes down as a result of the replacement of liquid by vapor adjacent to the heat transfer surface [82]. It is important to evaluate the CHF as it would destroy the target and the safety margin should be known. Plenty of investigations [83, 85] have been performed to investigate CHF on flow boiling in regular mini or microchannels. Most studies adapt the classic theoretical model developed by Kandlikar [86] to estimate the CHF.

According to [86], there are three nondimensional quantities used to evaluate CHF. The nondimensional quantity K_{CHF} represents the ratio of the evaporation momentum force to the surface tension force. The Weber number W_e represents the ratio of inertia to surface tension forces, and the capillary number C_a represents the ratio of the viscous to surface tension forces. The correlation of these three non-dimensional quantities is illustrated in the following equations [86]:

$$K_{CHF} = \left(\frac{q_{CHF}}{h_{fg}}\right)^2 \left(\frac{D_h}{\rho v \sigma}\right) \qquad (4.1)$$

$$W_e = \frac{G^2 D_h}{\rho \sigma} \qquad (4.2)$$

$$C_a = \frac{\mu_L G}{\rho \sigma} \qquad (4.3)$$

where q_{CHF} [W/m^2] is the CHF; D_h [m] is the hydraulic diameter of the cooling channel; h_{fg} [J/kg] represents the latent heat of vaporization; v [m/s] is water velocity; ρ [kg/m^3] is water density; σ [N/m] is surface tension; G [kg/m^2/s] is mass flux; μ_L [kg/ms] is dynamic viscosity.

According to the Weber number W_e, the whole region is subdivided into low and high inertia regions. In addition, each region is subdivided into low CHF region (LC) and high CHF region (HC). The detailed set of equations is shown below [86]:

(1) Low Inertia Region, LIR: W_e < 900:

I. For High CHF Subregion, i.e. LIR-HC: $L/D_h \leq 140$,

$$K_{CHF} = a_1(1 + cos\theta) + a_2 W_e(1 - x) + a_3 C_a(1 - x) \qquad (4.4)$$

II. For Low CHF Subregion, i.e. LIR-LC: $L/D_h \geq 230$;

$$K_{CHF} = a_4[a_1(1 + cos\theta) + a_2 W_e(1 - x) + a_3 C_a(1 - x)] \quad (4.5)$$

(2) High Inertia Region, HIR: $We \geq 900$:

I. For High CHF Subregion, i.e. HIR-HC:L/D_h < 60,

$$K_{CHF} = a_1(1 + cos\theta) + a_2 W_e(1 - x) + a_3 C_a(1 - x) \qquad (4.6)$$

II. For Low CHF Subregion, i.e. LIR-LC: $L/D_h \geq 100$;

$$K_{CHF} = a_4[a_1(1 + cos\theta) + a_2 W_e(1 - x) + a_3 C_a(1 - x)] \quad (4.7)$$

where L [m] is channel length; θ [degree] is the receding contact angle; x [%] is mass friction of vapor. The coefficients a_1 - a_4 [86] are scaling parameters, which are assumed to be constants and evaluated using the available experimental data:

$$a_1 = 1.03 \times 10^{-4}$$

$$a_2 = 5.78 \times 10^{-5}$$

$$a_3 = 0.783$$

$$a_4 = 0.125$$

In this work, the cooling material is water. And the channel diameter D_h is 0.35 mm, the length L is 80 mm, and x is assumed to be 0. The static contact angle θ is not directly measured in experiments, a value for contact angle was somewhat arbitrarily assumed in the model. For instance, a hemispherical bubble nucleus (θ = 90°) was assumed in [87], while a spherical bubble nucleus (θ = 180°) was assumed in [88]. Contact angles of 30° and 80° were assumed in [89] and only a weak dependence of the predicted incipient heat flux was noted on the value of the contact angle assumed. Therefore, in the present predictions, a contact angle of 30° was adopted.

Combining Equation (4.1) to (4.7), q_{CHF} [W/m^2] at JUDITH-II experiment in different subregions are summarized in Table 4.1.

Table 4. 1 Estimation of CHF of the first target with microchannel structures.

We =535.4		Ca=0.29		L/D=228.6
Region				q_{CHF} [W/m^2]
LIR: We < 900	Ture	HC: $L/D \leq 140$	False	8.41×10^6
		LC: $L/D \geq 230$	False	2.97×10^6
HIR: $We \geq 900$	False	HC: $L/D < 60$	False	8.41×10^6
		LC: $L/D \geq 100$	Ture	2.97×10^6

Note: "Ture" or "False" is determined according to the value of "We" or "L/D".

From the Table 4.1, the critical heat flux q_{CHF} from different approximations is between 3×10^6 W/m^2 and 8.4×10^6 W/m^2, which obviously underestimates the actual CHF of the target. The highest heat flux achieved at JUDITH-II experiment is 1.0×10^7 W/m^2 and the target is able to withstand it during the test. The CHF of the HBS target can just be estimated very roughly due to the special microchannel cooling geometry and unusual parameters (a high mass flux of 54 kg/m^2/s in at a small channel width of 0.35 mm). According to the Weber number We of the target, the q_{CHF} is supposed to occur in low inertia region (LIR). However, the value of L/D does not fit any subregion at LIR but match the inequality equation of low CHF subregion (LC) at the high inertia region (HIR), i.e. the actual q_{CHF} of the first target should be in the transition region. Still, the experimental values can provide some valuable insights. According to the reached heat flux of 1.0×10^7 W/m^2 during the test, it can be inferred that the true CHF should be double or triple the current experimental value since at the HBS facility the target will be operated with a proton beam rather than an electron beam. For electron heating, most power concentrates on the target surface, where only one-third of the tantalum-water interface participates in the cooling. However, for proton heating, all the tantalum-water interface, which contributes to cooling, is three times larger than the electron-heated surface.

Furthermore, this work would like to determine the value according to the available experimental data from measurements with similar channel width and comparable mass fluxes. Literatures [90 - 94] indicate a CHF is in the range between 1×10^7 to 2×10^7 W/m^2.

Fig.4.11 presents the heat flux distribution of the target which obtained from CFD simulations under the same setup as the high heat flux test at the JUDITH-2 facility. It can be seen that the heat flux mainly distributes on the target surface as expected. While the highest heat fluxes up to 1.0×10^7 W/m^2 occur in the solid tantalum region, i.e. the part between two separate microchannel structures and at the end of the microchannel structure, where the cooling efficiency is worse compared to the central region of the microchannel structure.

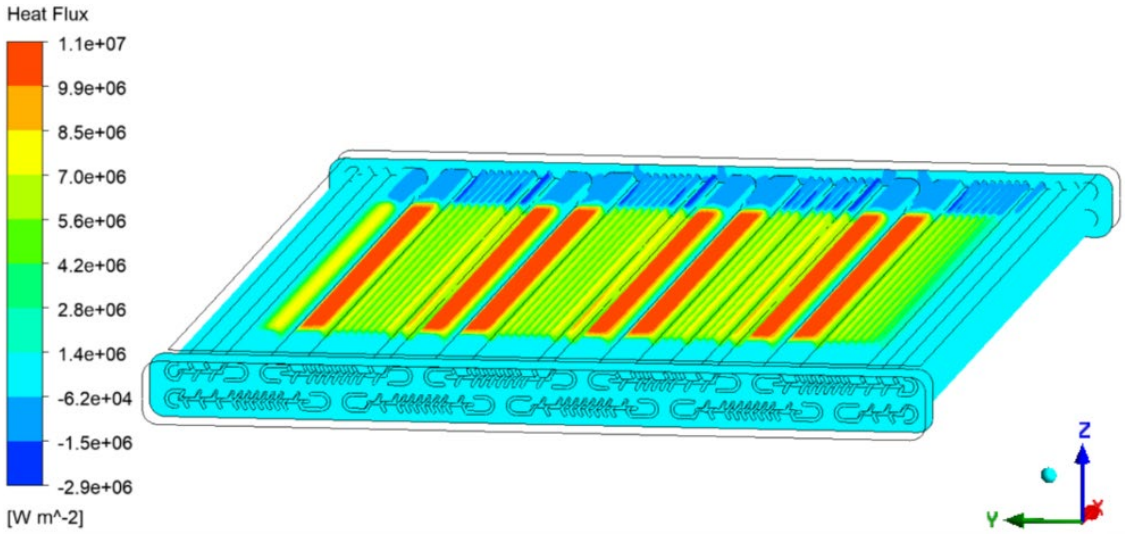

Figure 4. 11 Heat flux of the first target of CFD simulation [74].

4.6 Conclusions

The high heat flux test of the first microchannel target with an electron beam at the JUDITH-2 facility has shown that a power density of 1 kW/cm² can be dissipated with the special microchannel cooling concept, achieving the HBS design goal. The target has a twice or three times the current experimental value safety margin. Besides, the CFD simulations calculate the heat dissipation reliably.

5 Optimization of particle transport properties of the target

As introduced in the previous chapter, the first solid tantalum target [54] with a microchannel structure, is the result of optimization between the reduction of thermal and mechanical loads. The results of high heat flux test indicate the microchannel structure of the first target is able to provide sufficient cooling efficiency of 1 kW/cm². However, in addition to the heat dissipation issue, hydrogen embrittlement [56] and blistering problems [57] due to proton implantation and thermal stresses because of temperature gradients induced by inhomogeneous energy deposition are the other two risks endangering the target integrity according to literature [54]. Therefore, the relevant particle transport properties of the first target were checked with FLUKA in this chapter. It has been shown that 35% of the protons stop in the tantalum target and the energy deposition in the target is not homogeneous so local overheating occurs. From this point of view, the first target design was not fully optimized.

For the purpose of getting an optimal target design from both particle transport properties and mechanical aspects, the microchannel geometry was gradually adapted using the particle transport code FLUKA and thermo-mechanical simulations with ANSYS. The details of FLUKA simulations and the resulting microchannel target design will be presented in this chapter. The main relevant simulated particle transport properties include proton fluence, energy deposition, the spatial distribution of (p, n) reaction events and the spatial distribution of stopping protons within the target. The resulting design produces a homogeneous proton fluence and energy deposition without heat spots. In addition, only 4.56% of the impinging protons accumulate in the metal target, which can significantly reduce the risk of hydrogen damage. Besides, the average neutron yield of the optimal target can reach 1.45×10^{15} n/s, which meets the desired objective.

Note: Sections 5.1, 5.3, 5.4 and 5.5 are extracted from an associated publication [55].

5.1 Numerical method

All the simulations in this work are performed with the particle transport code FLUKA 2020.0 for GNU/Linux operating system, which is a fully integrated particle physics simulation package. The cross-sections for all simulations are taken from ENDF/B-8R0 [47] and JENDL40-HE [48].

The geometrical model utilized for the FLUKA simulations is depicted in Fig.5.1. The simulated geometry includes all details of the neutron-producing center of the target. The outer edge of the target and the cooling water connections are not simulated.

The target in Fig.5.1 is used to elucidate the simulation model, and the exact geometry of the target changes during the optimization process. The proton beam is a monoenergetic beam of 70 MeV, which is defined as a rectangular volume source, emitting the protons homogenously along Z (the target depth) direction. The beam surface covers the facing target surface completely. The assumption of a rectangular volume source is valid because the proton beam in the HBS project is scanned over a rectangular portion of the target with a high focus. The volume of the rectangular neutron-producing tantalum target is 10×10× [target depth] cm^3. The microchannel structures are filled with water. The beamstop at the backside of the neutron-producing tantalum target is filled with water to provide additional cooling at the target backside and to stop the protons. The water in all simulations of this Chapter is considered as liquid without bubbles under room temperature and standard atmospheric pressure. A thin layer of tantalum behind the beamstop is used as a structural material and to prevent proton leakage from the beamstop. All the microchannel structures have the same parameters, therefor the “lattice card” is used to replicate the periodic geometry when building the simulated model. The whole geometry has to be contained in a closed blackhole to absorb all escaping particles. This boundary condition is applied for all the simulations in this Chapter.

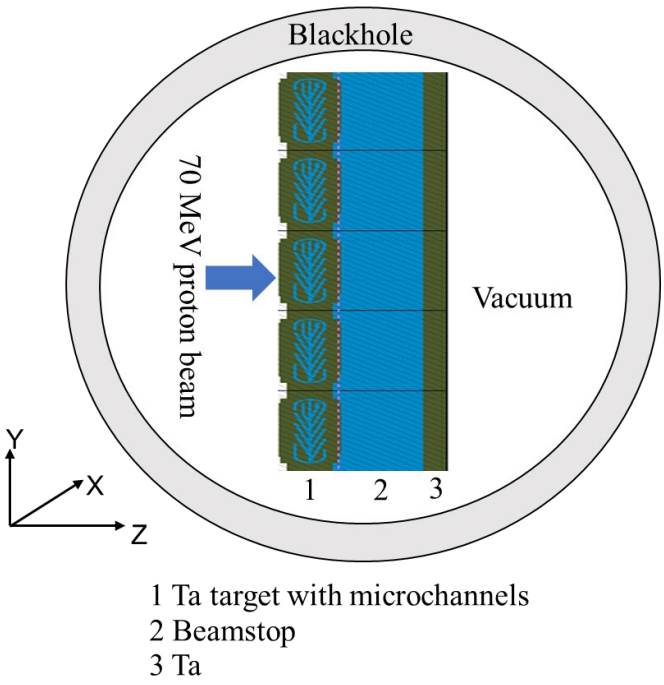

Figure 5. 1 Target geometry for simulations with FLUKA.

Concerning the energy deposition and proton fluence, the USRBIN[1] estimator is selected to score the pertinent quantities. The (p, n) reactions occurring in the whole target were recorded with the USEEDUMP[1] estimator. The information cannot be obtained through the standard options of FLUKA. Thus, an advanced subroutine, the USDRAW[1] entry of the MGDRAW[1] estimator was modified accordingly to record the 3-dimensional coordinates of the (p, n) reactions. The USEEDUMP[1] estimator is also utilized to record the spatial distribution of stopped protons. Analogously, the ENDRAW[1] entry of the MGDRAW[1] estimator is also customized correspondingly. In order to reduce the statistical errors sufficiently, the number of primary source particles to be simulated was always set to 5×10^6. The computation time of such a simulation is about one hour with Intel(R) Xeon(R) Gold 6154 CPU @ 3.00GHz. (Note: 1. The abbreviation is the name of a specific detector in FLUKA. Any result in a FLUKA simulation is obtained by adding up the contributions to the output of a detector defined by the user. A detector in FLUKA is the equivalent of a measurement instrument in experiments. Each “estimator” (detector type) is designed to estimate one or more radiometric quantities, and the final output is a statistical estimation of the average value of the corresponding population [95]).

5.2 Particle transport properties of the first target

The geometry of the first target [54] is shown in Fig.5.2, which has two rows of microchannel structure inside the solid tantalum target for cooling. The microchannel structures are staggered to distribute cooling evenly. Pure light water was filled inside the microchannels and the beamstop.

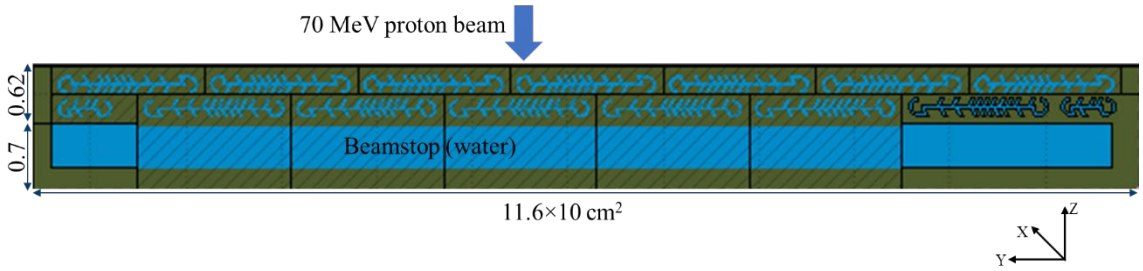

Figure 5. 2 The schematic diagram of the first target. Parameters are taken from [54].

The target is 11.6 cm long and 10 cm wide, and the main body of neutron-producing tantalum layer is 0.62 cm thick. The depth of water beamstop is 0.45 cm and a structural component behind the beamstop is a thin tantalum layer of 0.25 cm. The angle of the microchannels with respect to the main channel is 62°, the height of the microchannels is 0.0775 cm. The main parameters of the first target are listed in Table 5.1.

Table 5. 1 Main parameters of the first target.

Parameters	Values
Angle of the microchannels α	62°
Height of the microchannels h	0.0775 cm
Distance between neighboring channels d	0.04 or 0.12 cm
Thickness of the neutron-producing tantalum layer l	0.62 cm

The optimization was done in multiple steps beginning with the examination of the proton fluence and energy deposition. The geometry of the first target [54] utilized for the FLUKA simulations is depicted as in Fig.5.2. In the FLUKA simulations, protons bombard the target from the top direction. The proton beam is a 70 MeV monoenergetic beam, which is defined as a rectangular volume source that emits protons uniformly along the negative Z-direction, i.e. the target depth. The surface of the beam completely covers the surface of the facing target. The simulation tasks

are performed with the particle transport code FLUKA 2020.0 for GNU/Linux operating system. The cross-sections for all simulations are taken from ENDF/B-8R0 [47] and JENDL40-HE [48].

The two-dimensional distributions of proton fluence and energy deposition for the first target along the target width (Y) and target depth (Z) are shown in Fig.5.3, where the proton hits the target from the right side, i.e. along the target depth. According to Fig.5.3(a), the highest proton fluence occurs at the main body of the neutron -producing tantalum layer. At the intersection of the main body and the beamstop of the first target, part of the fluence drops sharply, which means that some protons stop at these critical points. Subsequently, some convex jagged peaks appear in the water beamstop and extend to the beginning of the thin tantalum wall, which reveals that proton fluence is not homogeneous. The energy deposition of the first target is presented in Fig.5.3(b), it can be observed that most energy is deposited at the end of tantalum target and even some red-hot spots occur there, i.e. energy deposition in the target is not homogeneous. Analogously, some convex jagged peaks also appear in the water beamstop and extend to the beginning of the thin tantalum wall. Ideally, energy deposition of the target should be homogeneous without local hot spots with the most energy deposit in the beamstop with no or little energy deposition in the tantalum wall.

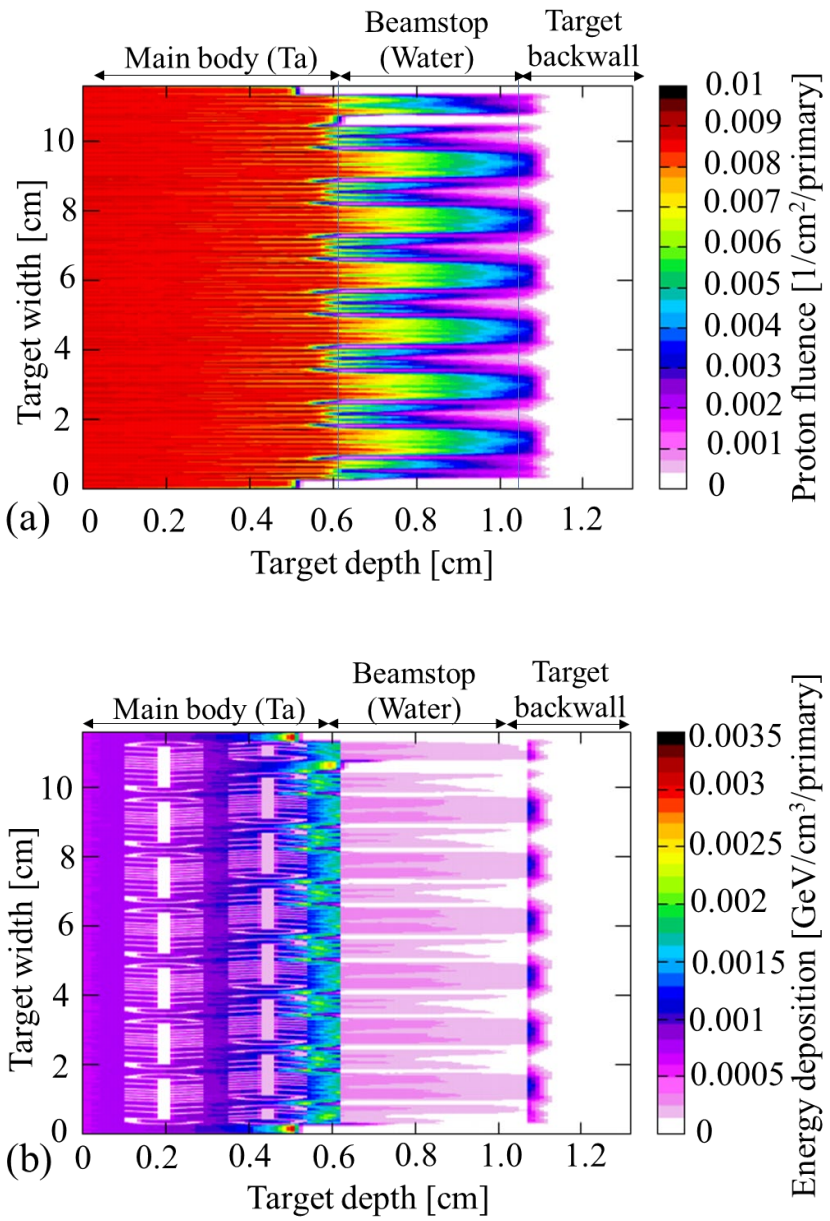

Figure 5. 3 Two-dimensional distributions of (a) proton fluence [1/cm^2/primary] and (b) energy deposition [GeV/cm^3/primary] for the first target along the target width (Y) and target depth (Z). The proton hits the target from the right side, i.e. along the target depth.

The other important factor is the quantity of proton implantation in the first target. For this, the spatial distribution of stopping protons in the first target is depicted in Fig.5.4(a). It indicates that most protons accumulate at the end of the main body of the target and then the tantalum backwall behind the beamstop, only few protons are dumped into the water beamstop at the backside of the

main body. In order to more intuitively present the information of the specific distribution, the percentage of the stopping protons over the target depth is plotted in Fig.5.4(b). The percentage along the target depth is normalized by dividing the corresponding number of stopped protons for a given target depth by the total number of stopped protons in the target, where the corresponding number of stopped protons for a given target depth is the integral of the stopped protons along the target length (X), the target width (Y) and the given target depth (Z), and the total number of stopped protons in the target is the total integral of the stopped protons along the target length (X), the target width (Y) and the entire target depth (Z). The X, Y and Z directions are shown in the 3D coordinates in Figure 5.1.

It can be directly observed from Fig.5.4(b) that about 35.3% of the protons accumulate in the main body of the neutron-producing tantalum layer and even 17% of them reach the tantalum backwall behind the beamstop, which indicates the first target has a severe proton implantation which would lead to a high risk of hydrogen embrittlement and blistering. One of the probable explanations is that the main body of the target is too thick so that most protons lose all energy within the neutron-producing tantalum layer and then stop in the main body of the target. The other one is the target geometry is complicated, with its multiple microchannel structures filled with water inside the tantalum target. The incident trajectories of the protons are scattered, some with straight tracks but most with inclined paths. Some protons barely travel through the water channels so that they lose all energies and finally to rest in the main body of the target, i.e. the first target design does not match with the proton beam of 70 MeV. In addition, only 47.6% of protons are deposited in the water beamstop and 17% of protons arrive in the target backwall of the thin tantalum layer, which reveals that the beamstop is not sufficient to consume the energies remaining of the protons crossing the neutron-producing tantalum layer. In general, all the results of particle transport properties suggest that the first design is not optimal.

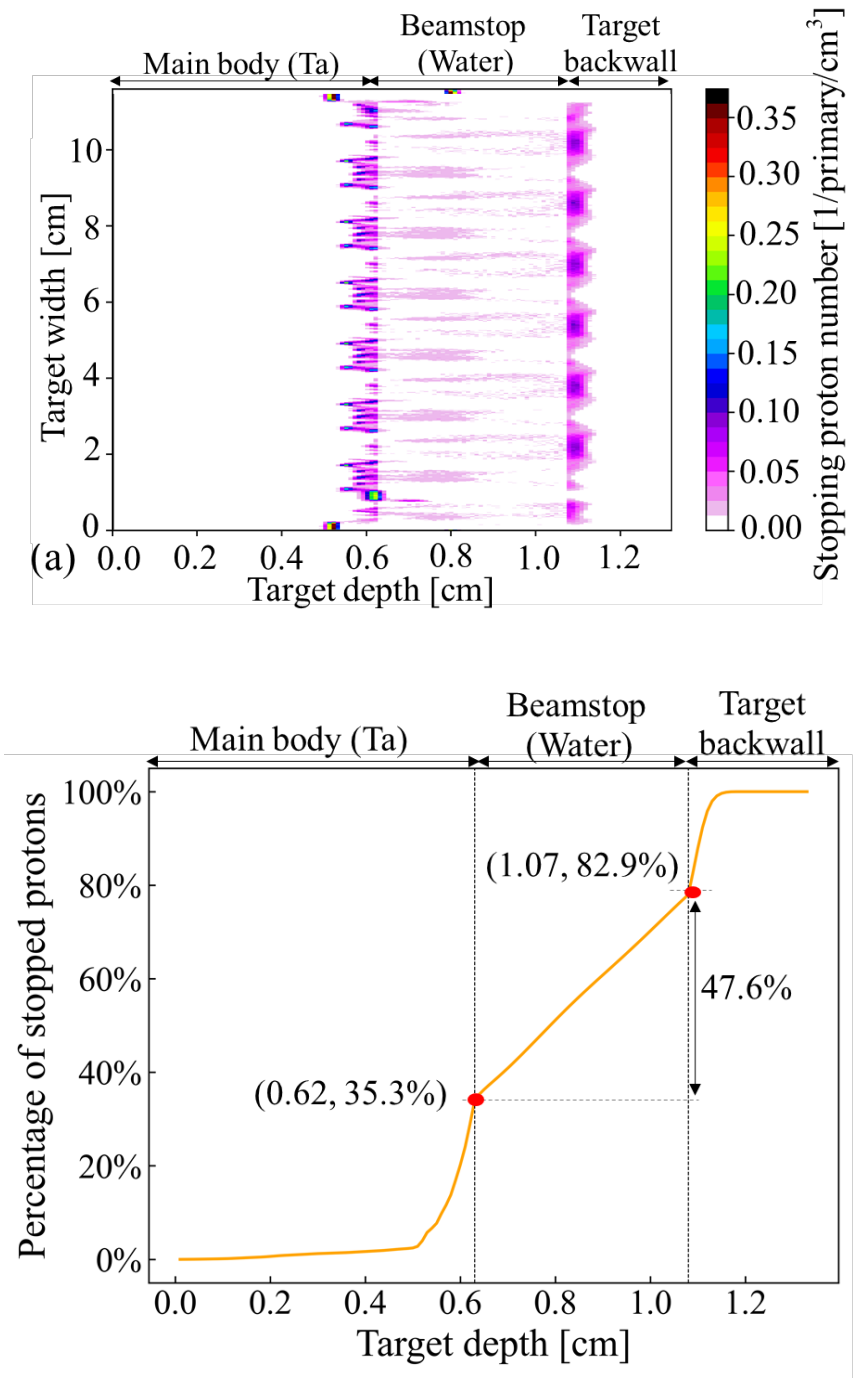

Figure 5. 4 (a) The two-dimensional spatial distribution of the stopped protons for the first target along the target width (Y) and target depth (Z); (b) The percentage of stopped protons along the target depth (Z) of the first target. The proton hits the target from the right side, i.e. along the target depth.

5.3 Optimization process

It is known that the first target can be further improved concerning the particle transport properties according to the results presented in the previous section. The aim is to obtain an optimal design that minimizes hydrogen implantation and features a cooling system that effectively removes heat and produces homogeneous energy deposition within the target. Objectives and potential problems and mitigations and partial constrain conditions are listed in Table 5.2.

Table 5. 2 Objectives, potential problems and mitigations for target optimization. Taken from [55].

Design goals	Potential issues	Mitigations	Constrain conditions
(1) Minimum proton implantation (2) Homogeneous energy deposition (3) Sufficient cross-sectional area of cooling channels (4) Maximum neutron yield [36]	(1) High proton current of 100 mA peak current (2)100 kW heat load release in a small target volume of 60 cm^3 (3) Inhomogeneous heat deposition	(1) To optimize microchannel structure (2) To have enough cooling area (3) To produce homogeneous heat deposition (4) To reduce thickness	(1) Microchannel width 0.35 mm [54] (2) 1.2 mm^2 of cross section of water channels per millimeter of target width[1] (3) The number of microchannel structures must be more than one[2]

Note: 1. According to CFD simulations of the first target [54], a water channel cross-section of more than 130 mm^2 over a total target width of 110 mm (Y-direction) can provide sufficient cooling efficiency, i.e., 1.2 mm^2 of water cross-section per millimeter of target width. **2**. In the HBS facility, the target will be placed in a vacuum with a pressure of 4 bar inside the microchannel structure caused by the cooling water (see Figure 6.9 in Chapter 6). The target will be deformed by the high bending stress caused by the water pressure. As the length of the microchannel structure increases, the bending stress on the target will also increase. To reduce the stresses appearing on the target, the number of microchannel structures should be more than one.

In order to create a target design with a periodic microchannel cooling structure which minimizes proton implantation and possesses sufficient cross-sectional area of cooling and homogenizes energy deposition, a microchannel structure as shown in Fig.3.2 was optimized. The main optimized parameters are listed in Table 5.3. The definition of parameters can be found in Fig.3.2.

Table 5. 3 Main optimized parameters of the microchannel structure of a target [55].

Optimized parameters	Range	Per step
Angle of the microchannels α	0º -30º	0.5º
Height of the microchannels h	0.7- 6 mm	0.2 mm
Distance between neighboring channels d	0.4- 8 mm	0.2 mm
Number of fins of each straight trajectory n	0-4	1

The parameter optimization is a manual step by step process, which can be divided into 3 steps in general. Firstly, to determine an arrangement of the microchannel fins that produces a homogeneous proton fluence and energy deposition. The variable in this step is only the angle of the microchannel fin, other parameters like the total tantalum volume, the thickness of microchannel fins and the position of the horizontal water channel are fixed. In order to narrow the scope of the study, we made a rough estimation concerning how energy deposition changes by varying the angle α from 0º to 90º (10º per step). It was found that microchannel structures with angles below 30º exhibited better homogeneity compared to other structures. The definition of the criteria to determine the homogeneity of energy deposition of a microchannel arrangement can be found in Section 5.4.2. Then a more specific investigation was made regarding the microchannel structure with angle α below 30º. The increment is decreased to 0.5º. Overall, the optimization process can be described in the following workflow diagram as shown in Figure 5.5.

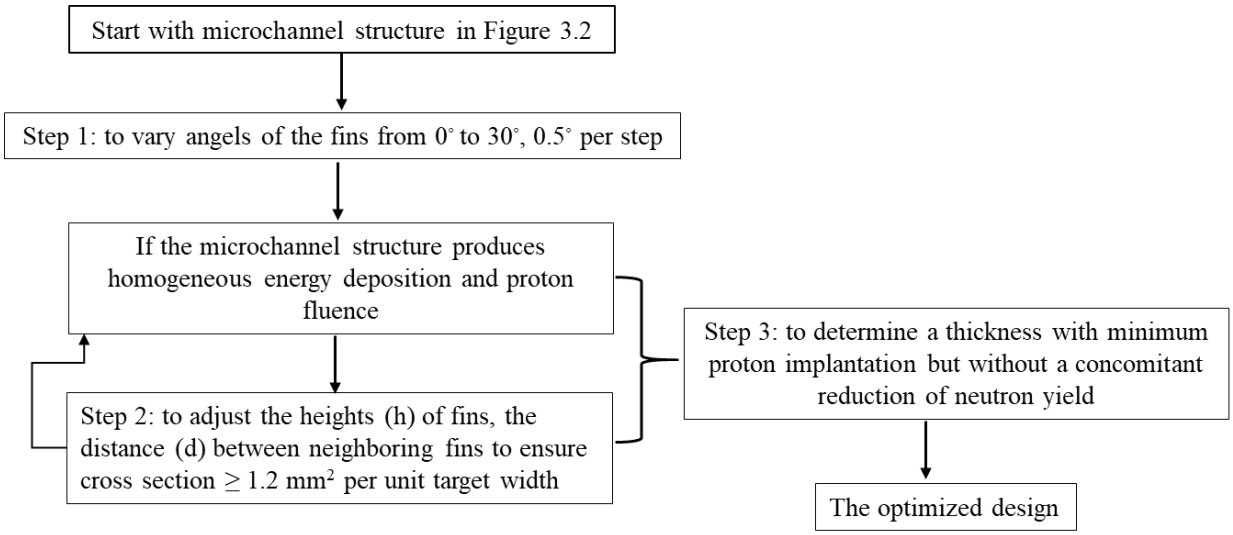

Figure 5. 5 Workflow diagram for target optimization [55].

5.4 Particle transport properties of the optimized target

5.4.1 Bragg curves of 70 MeV protons

As described in Table 5.2, the main design goals of the target include to minimize proton implantation, to homogenizes energy deposition and to maximize neutron yield. Each of these properties is related with "Bragg curves" [96], i.e. energy loss of ionizing radiation versus proton penetration depth during its travel through matter. Hence, FLUKA is used to calculate the energy deposition [MeV/cm/primary] (i.e. energy loss) of protons along the target depth during its travel through pure tantalum and water respectively.

For a high current proton beam bombarding a tantalum target, nuclear reactions along the penetration path lead to a build-up of neutron production and also an accumulation of stopped protons and an enormous energy being deposited towards the backside of the metal target. As mentioned before, the protons resting within the tantalum target can lead to hydrogen implantation, and heat release can cause stress problems. Thus, it is important to find out how the specific ionization is distributed along the path of the particle. For this we adapted "USRBIN" card of FLUKA to calculate the energy deposition (i.e. energy loss per bin) of protons along the target depth during its travel through tantalum and water, respectively. The unit of the output of

"USRBIN" is [GeV/cm^3/primary]. Then multiplying the output by the transverse area (100 cm^2) of the bin and 10^3 (GeV to MeV), then we get the energy loss per cm [MeV/cm/primary] along the target depth. Such a distribution, for a monoenergetic 70 MeV proton beam in solid tantalum and liquid water, are shown in Fig. 5.6 (a) and (b), respectively. Apparently, both the resulting depth-energy profiles (Bragg curves) exhibit a flat plateau region at the beginning of the track and a distinct peak near the end range of the particles. Note, a monoenergetic homogenous volumetric proton beam perpendicularly impinges from left perpendicular on the target.

From the curves in Fig.5.6 the penetration depth of 70 MeV protons in tantalum and water can be determined as 0.55 cm and 4.25 cm, respectively. The stopping range of tantalum for 70 MeV protons is about 7.8 times shorter than for water. Theoretically, a target with a thickness more than the penetration depth of ions is thick enough to stop all protons within the target. For a distinction, this work will define such a target as a thick target. And a target with a thickness thinner than the penetration depth will be called a thin target.

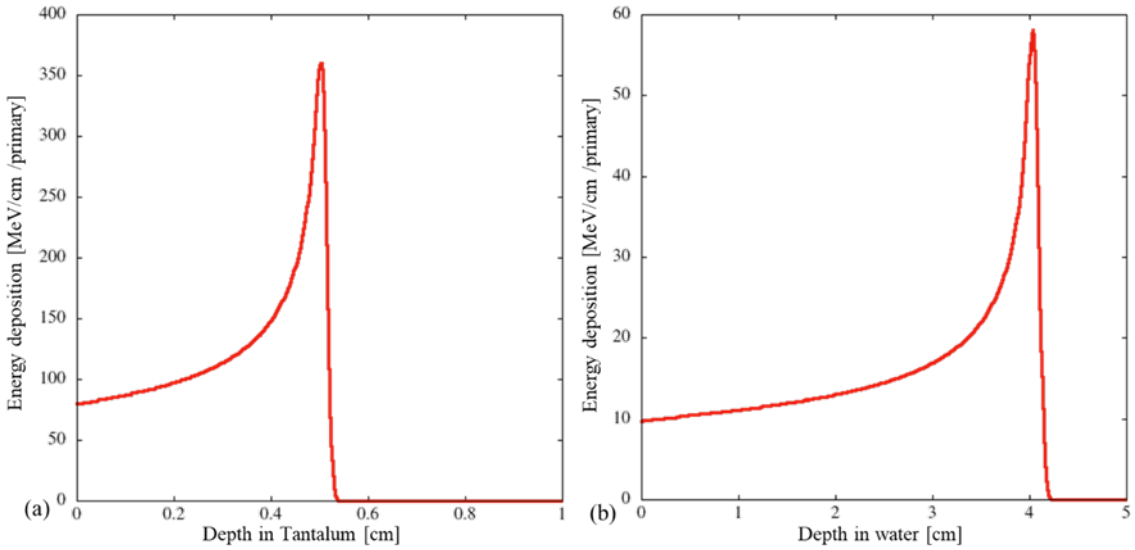

Figure 5. 6 Bragg curve of a 70 MeV proton beam in (a) tantalum and (b) water [55].

5.4.2 Energy deposition

It is important to have a homogeneous energy deposition on the target in order to reduce the stresses induced by temperature gradients and local hot spots. If a microchannel structure that can produce a homogeneous energy deposition is determined, the other two important factors of the

minimized proton implantation and the maximized neutron yield can be achieved by adjusting the target thickness. The main criteria to determine the homogeneity of the energy deposition of a microchannel arrangement include three points. For this we adapt the normalized rms (root mean standard) deviation *T* (see equation (5.1)) as a measure for the relative fluctuations, and calculate it at two critical positions (lines). The smaller the deviation is, the more homogeneous the energy deposition is. The homogeneity of the energy deposition at the exit of the neutron-producing tantalum layer allows for the location of the proton implantation point. Thus, two critical lines are only 0.1 or 0.2 mm before and after the interface between the neutron-producing tantalum layer and the light baffle, respectively.

$$T = \frac{\sqrt{\langle (\mathrm{e}(y) - \langle \mathrm{e}(y) \rangle)^2 \rangle}}{\langle \mathrm{e}(y) \rangle} \quad (5.1)$$

where $\mathrm{e}(y)$ is the energy deposition of protons along the critical line(s) as a function of the y coordinate.

Figure 5.7 shows energy deposition of designs for α= 14.5º (up) and 26º (down) and the specific three critical positions.

The critical lines are:

Line 1 x = 0.02 cm, which is inside tantalum target, but behind the microchannel structure;

Line 2 x= -0.01 cm, which is just after tantalum target and the beginning of water beamstop;

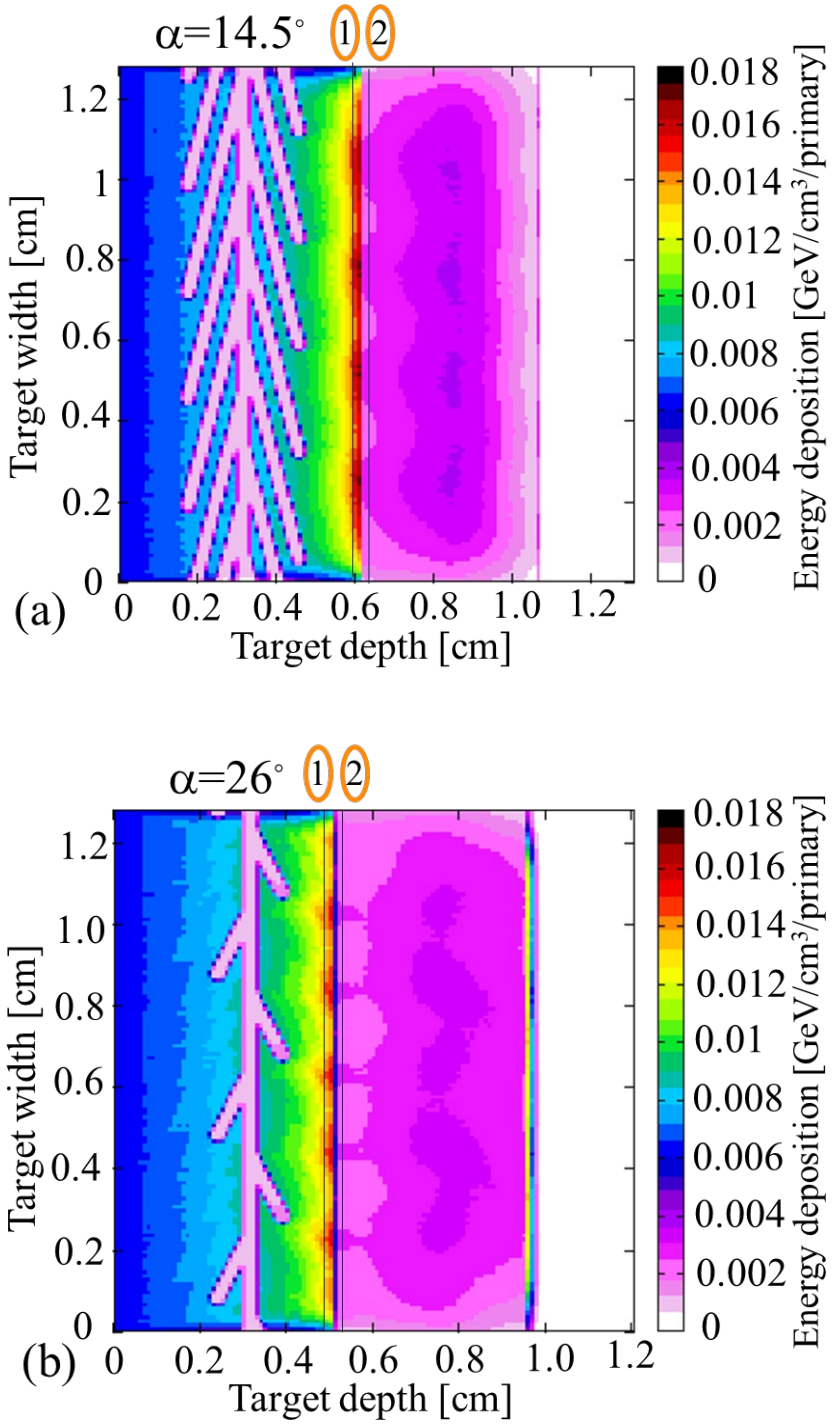

Figure 5. 7 Energy deposition of microchannel structures of (a) angle α=14.5º and (b) α=26º.

The normalized rms deviations of energy deposition in the critical lines for both microchannel structures presented in Figure 5.7 are summarized in Table 5.4.

Table 5. 4 Normalized rms deviations of the energy deposition in critical lines of microchannel structures for angle α=14.5º (up) and 26º (down).

Angle α	T_1 at line 1 x= 0.02 cm	T_2 at line 2 x= -0.01 cm
14.5º	0.028	0.043
26º	0.041	0.062

According to the deviations in Table 5.4, it can be seen that the fluctuations of energy deposition in the microchannel structure of α=14.5º is smaller than ones of α=26º, i.e. the energy deposition in the former case is more homogeneous than the later one. This also can be observed from Figure 5.7.

5.4.3 Proton implantation

Based on the homogeneity of energy deposition for different microchannel structures, a microchannel structure (α=14.5º) shown in Figure 5.8, was obtained. In a design as shown in Figure 5.8, the microchannel structure has a cooling channel cross-section of 1.64 mm^2 per unit target width, which meets the constraints listed in Table 5.2, where the microchannel structure for cooling water should have a cross-section greater than 1.2 mm^2 per millimeter of target width in order to have sufficient cooling efficiency. Therefore, the microchannel structure presented in Figure 5.8 is selected in the further investigations where only the target thickness will be varied to minimize proton implantation (see this section) and maximize neutron yield (see section 5.4.4).

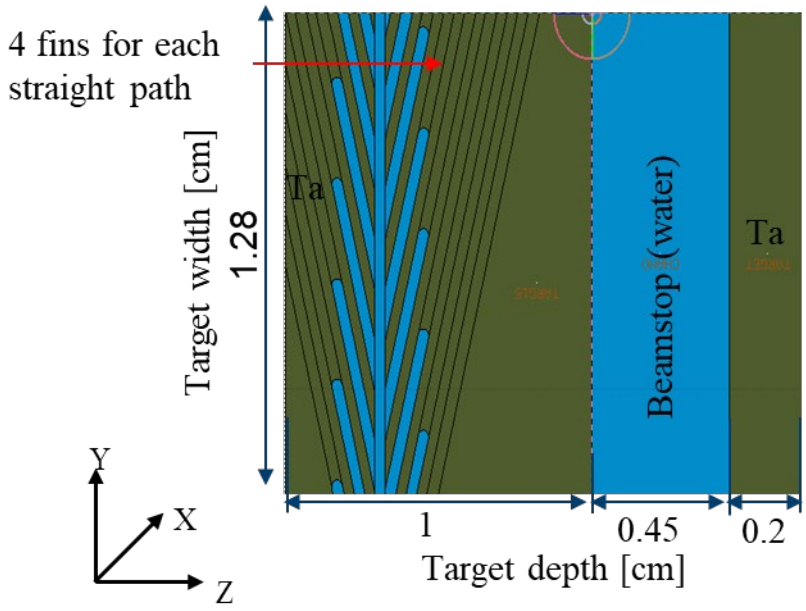

Figure 5. 8 A slice of a target with periodic microchannel structure (α=14.5º) [55].

The key to minimizing proton implantation in the target is to stop the proton at the beamstop, i.e. the Bragg peak of the proton should occur after the neutron-producing tantalum layer, but within the beamstop. In order to determine the Bragg peak, the thickness of the neutron-producing tantalum layer is increased to 1 cm as shown in Figure 5.8. It is more than 0.55 cm of the penetration depth of 70 MeV protons in Ta (see Figure 5.6), we will simply call it a thick target in the following text. In a target with a microchannel structure as shown in Figure 5.8, a straight trajectory of each impinging proton, e.g. the red arrow in Figure 5.8, intersects 4 fins as well as a main water channel. Besides, the beginning of one microchannel fin on one side always coincides with the end of the second next fin on the opposite side. Main parameters of such a geometry are listed in Table 5.5. The angle of the microchannels with respect to the main channel is α=14.5º, the height of the microchannels is h=0.14 cm and the distance between neighboring channels is d=0.26 cm. The thickness of the neutron-producing tantalum layer is 1 cm. With such a thick target, all protons are stopped in the neutron-producing tantalum layer so that the Bragg peak position can be determined. In this way, a proper target thickness which is slightly smaller than the penetration depth of protons but without a concomitant reduction of the neutron yield can be obtained.

Table 5. 5 The main parameters of a slice of a thick target. Taken from [55].

Parameters	Values
The angle of the microchannels α	14.5°
The height of the microchannels h	0.14 cm
The distance between neighboring channels d	0.26 cm
The number of fins of each straight trajectory n	4

Figure 5.9 shows the proton fluence and energy distribution of a piece of target with microchannel structure presented in Figure 5.8. It is worth mentioning that the tantalum on the right side was increased to 1 cm thick in order to completely stop the 70 MeV protons from flying off the target. Figure 5.9 focusses only on the thick neutron-producing tantalum layer and does not show the entire mechanical structure with the water beamstop and the thin tantalum layer behind the beamstop in order to get a better resolution. The proton fluence, Figure 5.9(a) indicates that the highest change of proton fluence concentrates on a straight line, which is 0.65 cm away from the target surface. This is the location of the so-called Bragg peak, where most protons are stopped. Overall, the distribution of proton fluence is pretty homogeneous except minor dark thin strips appear at intervals. The probable reason is that some protons crossing the tip of a water fin are scattered into ambient tantalum, which causes the local proton fluence to be higher. Analogously, the energy deposition presented in Figure 5.9(b) is homogenous as well. Therefore, we adapt this microchannel structure to continue the further optimizations.

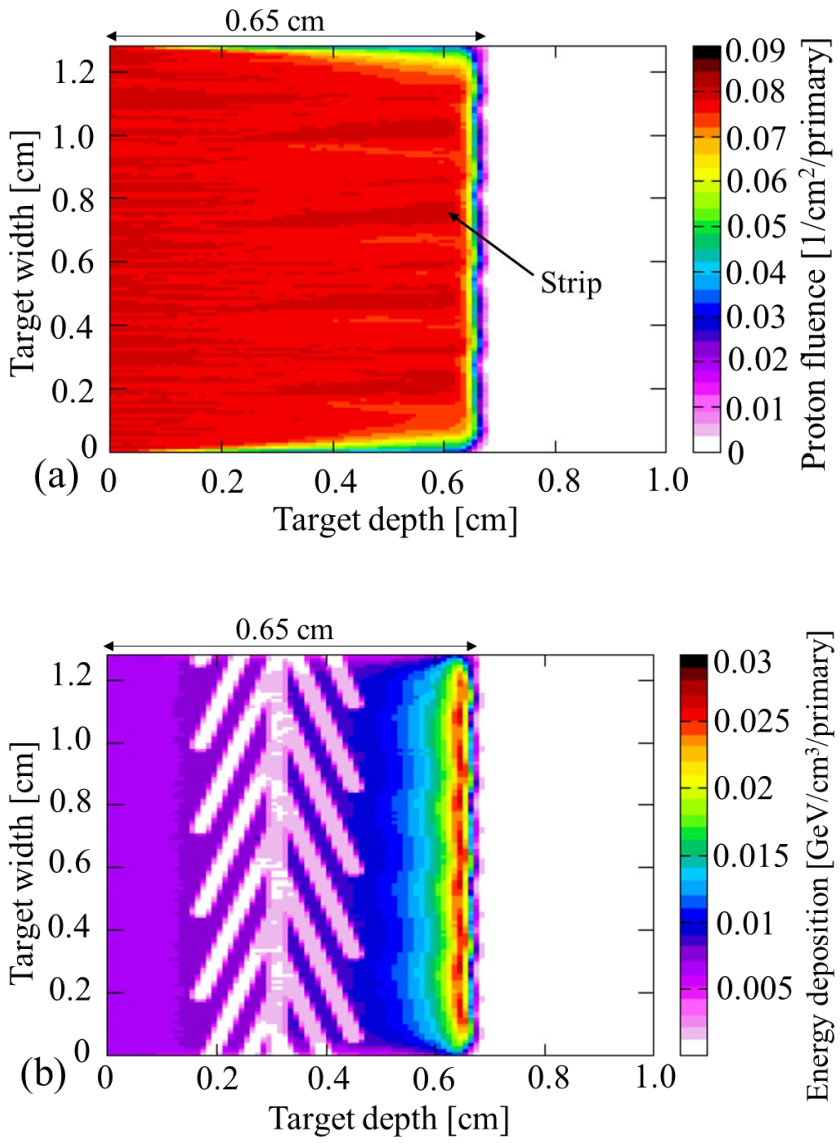

Figure 5. 9 (a) Proton fluence [1/cm^2/primary] and (b) Energy deposition [GeV/cm^3/primary] of a slice of a target with periodic microchannel structure (α=14.5^o).

For the purpose of obtaining a proper target thickness to alleviate hydrogen implantation but without the associated loss of neutron output, the percentage of stopped protons, the percentage of neutron production and the percentage of energy deposition as a function of depth in the thick target are shown in Fig.5.10. The percentage has been normalized by dividing the number of the corresponding quantities accumulating in a given target depth by the corresponding total amount in the target, where the number of the corresponding quantities accumulating in a given target depth is the integral of the stopped protons or neutron production or energy deposition along the

target length (X), the target width (Y) and the given target depth (Z), and the corresponding total amount in the target is the total integral of the specific quantity along the target length (X), the target width (Y) and the entire target depth (Z). The X, Y and Z directions are shown in the 3D coordinates in Figure 5.8.

The green curve in Figure 5.10 depicts the distribution of the stopped protons along the target depth. The counted stopped protons include both primary and secondary protons. It can be observed that the green curve features a steep step, from a nearly constant level at the target depth of 0.58 cm. This perfectly explains the phenomenon presented in Figure 5.9 that the highest change of proton current concentrates on a straight line and the most energy also deposits at a small interval. Only 4.6% of protons is implanted at the first inflection point where the target is 0.58 cm thick. Besides, the yellow curve of Figure 5.10 shows that the percentage of energy deposition in different target depth. It indicates that the percentage of energy deposition increases steadily towards the end of the target and reaches 100% at the target depth of 0.65 cm. It is just 76% of the heat load is deposited in the target and 24% of the heat load can be shifted towards the beamstop when the target thickness is reduced to 0.58 cm.

Last but not least, the percentage of neutron production as a function of depth in the thick target is also presented with a red line in Figure 5.10. It shows that the neutron production increases with an increase in the target depth reaching up to 98% at the target depth of 0.58 cm, where only 4.6% of protons and 76% of the heat load is accumulated in the target. Correspondingly, the Bragg peaks would appear in the beamstop (water channel) behind the neutron-producing tantalum layer. With the intention of reducing heat load and minimizing hydrogen implantation in the target but also maximizing neutron production, the target thickness should not be thicker than 0.58 cm.

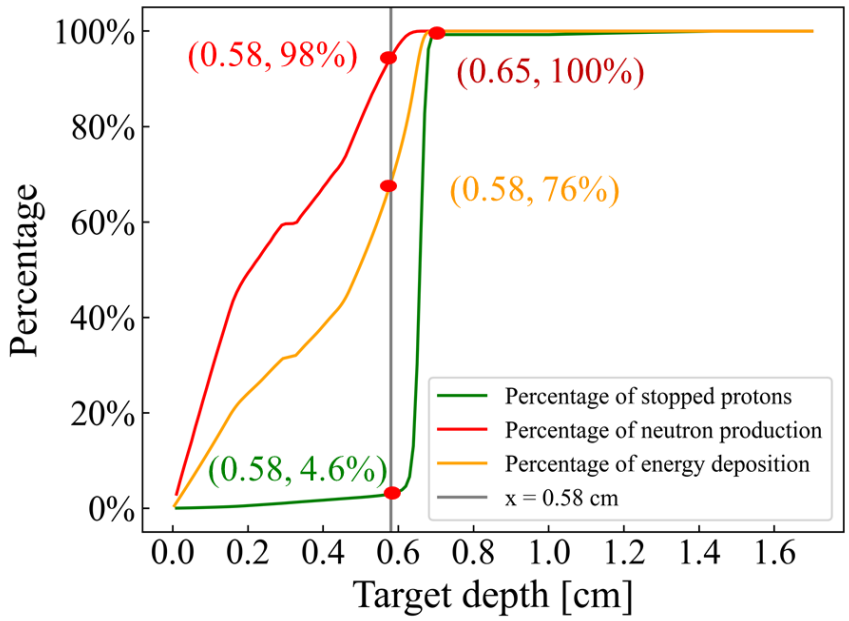

Figure 5. 10 Percentage of stopped protons, energy deposition and neutron production induced by ^{181}Ta (p, xn) along target depth of a thick target.

To determine a realistic target design, the microchannel structure and target thickness are identified according to the optimization results presented in Figure 5.9 and 5.10. Given the notch effect [97], each microchannel structure ended with rounded segments to minimize an uneven stress distribution. Therefore, a complete thin target presented in Figure 5.11 is obtained on the basis of the thick target with the microchannel structure shown in Figure 5.9. Main parameters of the microchannel structures are summarized in Table 5.5. The solid tantalum parts between the individual microchannel structures are simply called “bridges”. The distance between the bridges and the width of the bridges are determined by mechanical simulations of the target to avoid too much deformation due to the water pressure inside the microchannel structure. The specific details will be introduced in Chapter 6. In order to avoid proton implantation in the bridges, part of the tantalum is removed from the upper surface to ensure that Bragg peaks appear in the beamstop. On the other hand, cutting some tantalum in the bridge section can also help to produce homogeneous proton energy loss throughout the whole target to minimize temperature gradients.

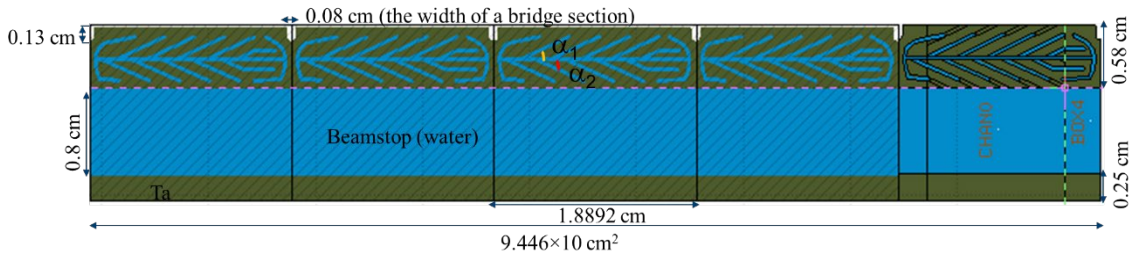

Figure 5. 11 The schematic diagram of a complete target.

As mentioned before, the key to minimize the risk of hydrogen embrittlement and blistering problems is to minimize the number of protons accumulating in the neutron-producing tantalum layer. For this, the two-dimensional spatial distribution of stopped protons along the target depth and target width in the complete thin target is recorded correspondingly as shown in Figure 5.12(a). As apparent in Figure 5.12(a), most protons are dumped into the beamstop ("proton pool") at the backside of the tantalum target. There are nearly no protons accumulating in the neutron-producing tantalum layer except some little spots at the end of the bridge sections of the target. One probable explanation could be that some protons crossing the steep edges of the bridge sections are scattered into the solid tantalum. Those protons traverse more tantalum, which results in losing all energy and ultimately stopping inside the target. In addition, the percentage of the stopped protons over the target depth in the complete target is plotted in Figure 5.12(b). Apparently, only 4.56% of protons accumulate in the metal target and 93.22% of protons stop in the beamstop. Even only 2.22% of protons arrive to the tantalum wall behind the beamstop, which states the current target design results in a well-defined Bragg-Peak positioned inside the water beamstop minimizing the accumulation of protons within the target. This work also tried to decrease the percentage of protons accumulating in the target, it turns out that 4.56% is already the best compromise situation under the constraints of a maximum neutron yield. Most of the protons resting inside the target have experienced a (p, n) reaction event or a scattering event with a Ta nucleus, which leads to a strong energy loss or a strong deviation from the original flying direction, so that they cannot reach the beamstop.

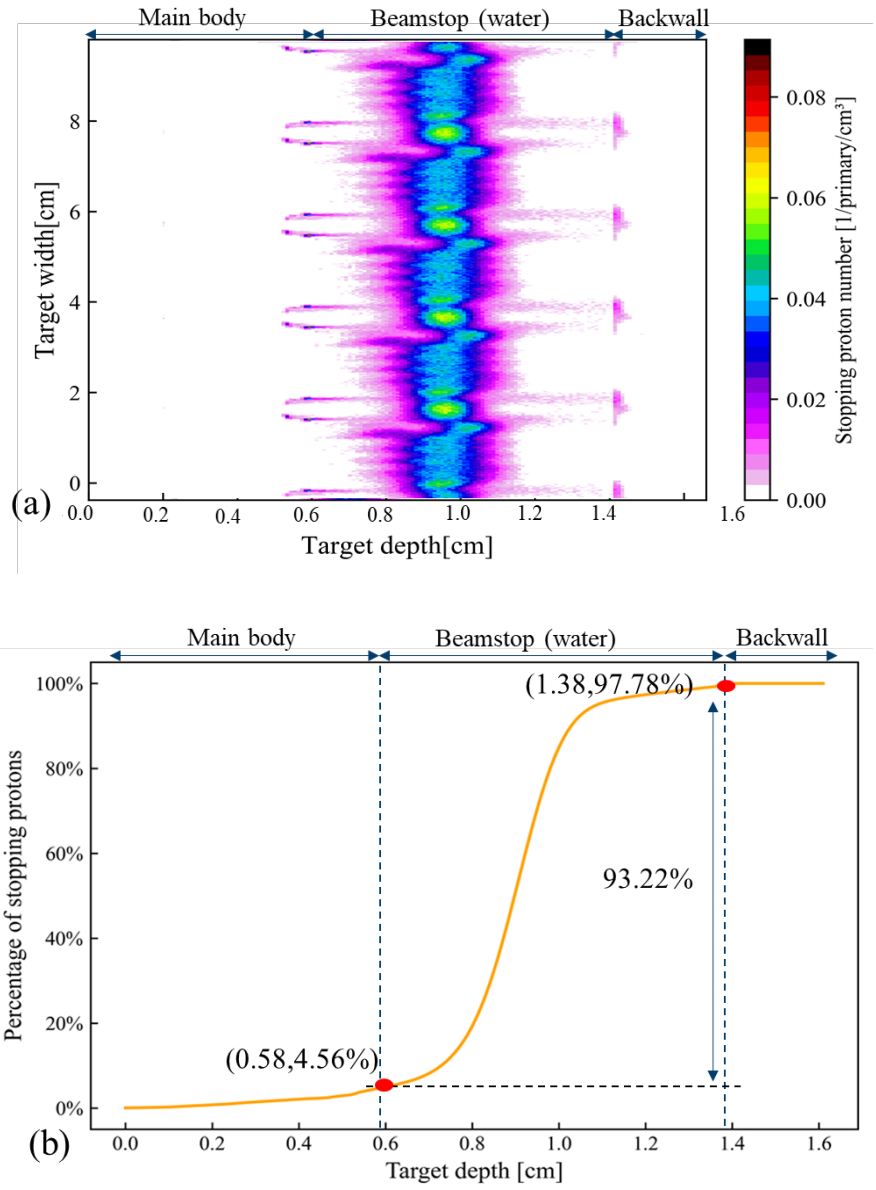

Figure 5. 12 (a) The spatial distribution of stopping protons in the complete target; (b) Percentage of stopping protons along the target depth in the complete target.

5.4.4 Neutron production

In addition to prevent hydrogen implantation and inhomogeneous energy deposition, this work also optimized the target design for a high neutron yield. The pattern of neutron production of the target is as expected, based on the obtained distribution of ^{181}Ta (p, xn) reactions in the thin target and the number of ^{181}Ta (p, xn) reaction events along the target depth, depicted in Fig.5.13. Most

^{181}Ta (p, xn) reactions take place in the metal Ta of the target. The blue region at the beginning of the target indicates most neutrons are produced where the energies of protons are highest. The amount of the reactions becomes lower towards the end of the target. In the beamstop and also the tantalum wall behind the beamstop nearly no neutrons are produced as the proton energy threshold is 10 MeV for ^{181}Ta (p, xn) reactions [47]. This also states the thickness of 0.61 cm of the thin target is a proper choice for 70 MeV protons to produce a high neutron output.

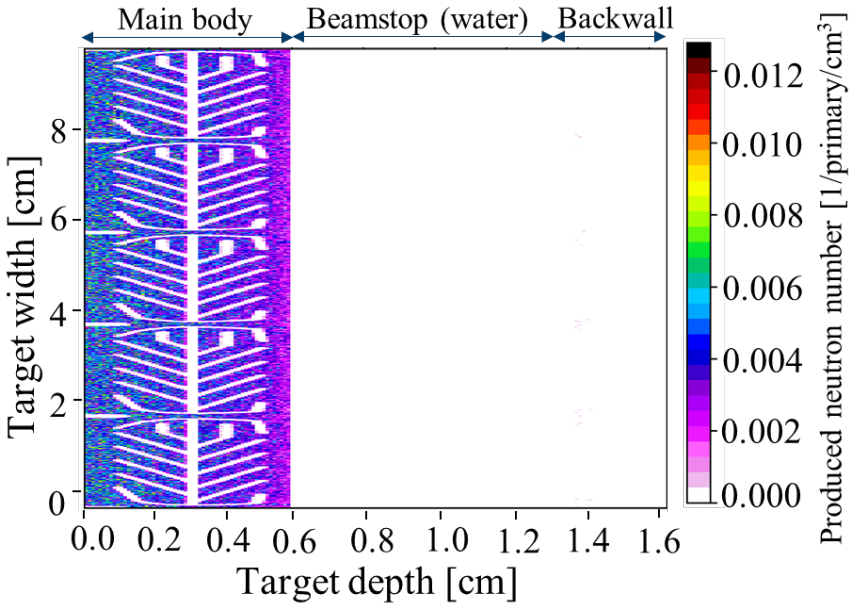

Figure 5. 13 The distribution of ^{181}Ta (p, xn) events in a thin complete target.

5.4.5 Displacement Per Atom (DPA)

Considering the manufacturing and maintenance expenses, the HBS target is expected to have a service period as long as possible. It is possible to obtain DPA values or the two-dimensional spatial distribution of DPA by using the DPA-SCO option in the WHAT (2) field of the USRBIN card in FLUKA simulations, where DPA are given as number of displacements per atom per unit primary weight, averaged over the bin volume, so-called average DPA [1/primary]. Therefore, this work also calculated the DPA (Displacement per atom), a unitless physical quantity accepted standard indicator for radiation damage in materials, to estimate the target's lifetime. In the DPA simulations with FLUKA, the threshold displacement energy E_d is defined as 90 eV [98].

Regarding the particle transport, a global threshold of 10^{-14} GeV was defined by a PART-THR card for protons and neutrons generated during the collisions cascade.

The induced damage is dominated by protons and neutrons, which is consistent with the results in the literature [98]. The damage caused by protons and emitted neutrons are characterized based on the target depth Z and target width Y two-dimensional spatial distribution of atomic displacement in the target, as show in Fig.5.14 (a) and (b), respectively. It can be seen from Fig.5.14 (a) the maximum values of the proton-induced DPA mainly concentrates at the end of target, corresponding to the region where the protons have the highest energy loss and are stopped. As shown in the Fig.5.14 (b), neutron-induced damage is quantitatively smaller and more evenly distributed compared with DPA induced by protons.

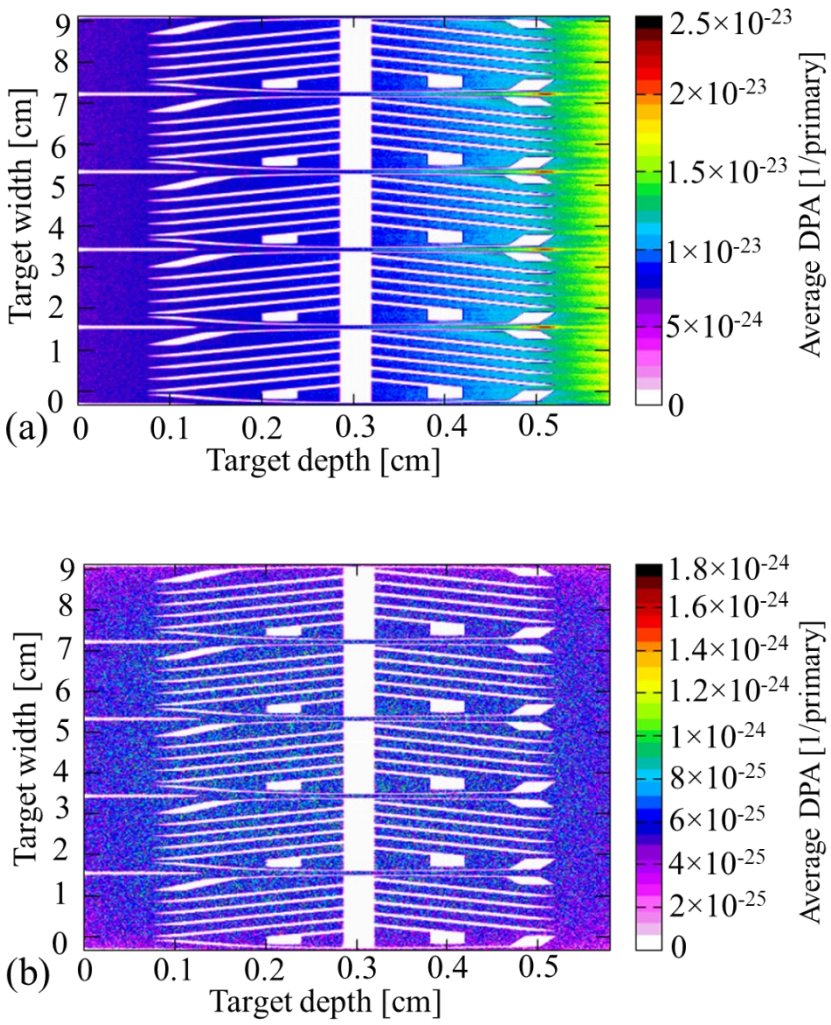

Figure 5. 14 (a) Spatial distribution of the proton atomic displacements of the optimized target; (b) Spatial distribution of the neutron atomic displacements of the optimized target.

The minimum lifetimes are estimated based on the reference DPA values derived from irradiation tests of the tantalum target operated for ISIS, i.e. 11 dpa [58], [99] for proton-induced damage and 0.14 dpa [100] for the damage rates of neutrons, as depicted in Table 5.6. According to the total integrated values of the average DPA induced by protons and neutrons over the target, the lifetimes of 5.70 and 1.17 years respectively, are predicted, which are higher than the estimation of 2.62 and 0.78 years reported in [98]. The reason is the target in [98] is a solid tantalum target without water channels inside and the target thickness is 0.5 cm, where the top point of Bragg peak occurs exactly according to Fig.5.4(a). In this case, the highest energy loss of protons occurs inside the target, and then more protons accumulate there, thus causing higher DPA damage and shorter service life.

Table 5. 6 Estimation of the minimum lifetime of the optimized target.

	Annual dose [dpa/fpy]		Minimum target lifetime [years]	
	Reference values	Calculated values	This work	Reference [98]
Protons-induced	11	1.93 ± 0.02	5.70	2.62
Neutrons-induced	0.14	0.12 ± 0.02	1.17	0.78

Note: [DPA/fpy] is displacements per atom (DPA) per full power year.

5.5 Conclusions

An optimized microchannel tantalum target for a low energy (proton beam 70 MeV) accelerator-driven neutron source was obtained by parameter optimizations. The challenge in such a design is the hydrogen embrittlement and blistering problem because of the high average proton current of 8.74×10^{15} s^{-1} focusing on a target surface of 100 cm^2 and 100 kW heat load release in the thin target, and thermal stresses due to inhomogeneous energy deposition. It is resolved by determining an optimized internal cooling microchannel structure matching the energy of the proton beam and a proper target thickness, which is slightly smaller than the ion penetration depth. In this optimized design more than 93% of protons are dumped into the beamstop and only 4.56% of protons accumulate in the target, which strongly minimizes the risk of hydrogen damage. A cross-sectional area of cooling channels of 164 mm^2 are used to dissipate heat. Also, a homogenous proton fluence and energy deposition can be obtained by this target design, which can efficiently decrease thermal stresses caused by temperature gradients. Last but not least, based on the damage induced by protons and neutrons, a minimum lifetime of 1.17 years is predicted.

This work provides an efficient and practical target design to produce high brilliance neutrons with a limited hydrogen implantation, which will be of benefit in the development of compact accelerator-based neutron sources.

6 Thermo-mechanical design of the target

The thermo-hydraulic and thermo-mechanical simulations with ANSYS in this chapter were carried out by Jörg Wolters of the HBS team at ZEA-1 of the Forschungszentrum Jülich. The simulations were performed on 2 nodes of the ZEA1-HPC-Linux- Cluster, each with 48 cores and 500 GB of main memory. The CFX-simulation for the pulsed operation took 8 days and 15 hours (for 13 pulses). The two subsequent mechanical simulations took about 1 hour on 96 cores.

This chapter presents the final geometry of the optimized target which results from a long iteration between particle transport optimization with FLUKA and thermal-hydraulic and thermo-mechanical simulations with ANSYS. The cooling circuit of the optimized target will be introduced. In addition, the relevant mechanical and thermal-mechanical characteristics of the optimized target will be described in detail as well. ANSYS simulation starts at time averaged steady state condition [101], i.e. the beam power stays at a constant value of 100 kW during operation time. However, since the HBS target will be operated under a pulsed proton beam, thermal-hydraulic simulations were also performed for unsteady flow condition [102]. For steady state conditions, the specific simulated performances include temperature distribution [°C], pressure map [MPa], heat flux [W/m^2], stress [MPa] and strain [mm/mm]. For the pulsed operation, so far only temperatures [°C] and heat flux [W/m^2] have been investigated in detail. Mesh studies were performed to get an adequate mesh in the relevant zones. For this, sweep method [103] is used for target and fluid in heated region. The inflation layer for a good resolution of the solid-fluid interface have been used. The material properties of the solid tantalum and liquid water adopted in ANSYS simulations are summarized in Table 6.1. For coolants, i.e. liquid water, the relevant properties listed in Table 6.2 are referenced from the IAPWA library [53].

Table 6. 1 Material properties of solid tantalum adopted in ANSYS simulations.

Material	Properties	Values
Tantalum	Density	16600 kg/m^3
	Specific heat capacity	140 J/kg/K
	Thermal conductivity	57.6 kg/m^3/K
	Elastic modulus	184 GPa
	Poisson's ratio	0.28
	Yield stress	185 MPa [104]

Table 6. 2 Material properties of liquid water adopted in ANSYS simulations.

Material	Properties	Values		
Water	Temperature [°C]	20	50	100
	Density [kg/m³]	998.3	988.2	965.38
	Thermal conductivity [W/m/K]	0.59853	0.64365	0.67541
	Heat capacity [J/kg/K]	4184.2	4178.0	4204.7
	Dynamic viscosity [mPa·s]	1.007	0.5481	0.31483

6.1 Target design and cooling

Fig.6.1 shows the design of the optimized target, which consists of three parts, 180° turnaround for serial coolant flow, the adapter for inlet and outlet and the main body for neutron production. Fig.6.2 presents the cut view of the main target with microchannel structure. It indicates that the main target is composed of a solid tantalum body, a layer of water behind it and a tantalum backside behind the water. In reality, the neutron-producing tantalum body is approx. 0.58 cm high, the beamstop is 0.8 cm and the back layer is 0.25 cm. As a result, this work gets a tantalum mass of 4.43 kg and a water mass of 0.244 kg in the target with these dimensions. Compared to the first target, the optimized target has an increased distance from the two ends of the body to the microchannel, so there are almost no sheets from the welding that block the cooling channels. With

the improved design of the 180° turnaround for coolant flow, the heat transfer is increased in the beamstop by increasing the velocity at the corresponding surface of the target close to the turnaround and hence the cooling is also improved. On the other hand, the combination of the inlet and the improved design of the 180° turnaround avoids the coolants at the inlet entering into beamstop instead of the microchannel structure. (Note, for the first target, one side with the inlet connected to both the microchannel structure and beamstop, and the other side with one outlet connected to both the microchannel structure and beamstop. When the microchannel structure is clogged, coolant would flow into the beamstop instead of the clogged microchannels, which results in a low cooling efficiency).

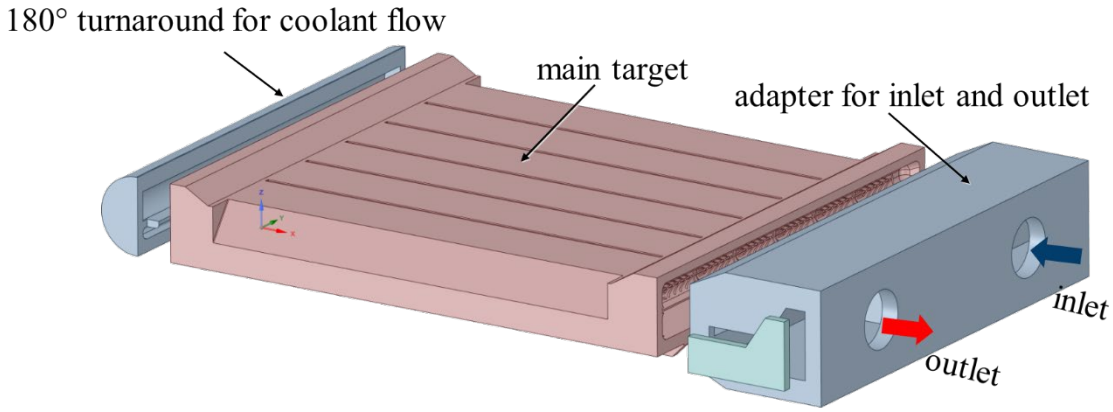

Figure 6. 1 An outside view of the optimized target. The blue arrows show the direction in which water enters the target. The red arrows show the direction in which water flows out of the target [105].

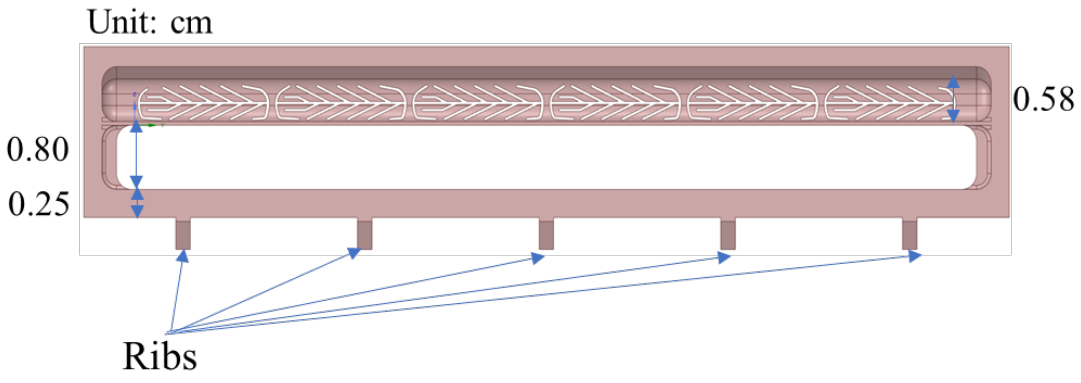

Figure 6. 2 A cut view of the main target [105].

For the first target, the water flow in the microchannels is parallel as the one inside the water beamstop which is behind the target. But for the optimized target, as shown in Fig.6.1, the entire flow of coolant water is changed as there is only one water connection with inlet and outlet for the optimized target. Here are a few pictures to illustrate the water flow. Fig.6.3 (a) and (b) depict the cooling circuit of the target in the neutron producing tantalum part and the beamstop, respectively. And Fig.6.4 describes the cooling structure of the target in two more side views. The blue arrows represent at the inlet the flow enters into target and red arrows show the cooling flow out at the outlet. According to Fig.6.3 and 6.4, the primary cooling circuit is connected to the round holes in the target. From the inlet the water goes into the target and enters into the microchannels to make a heat exchanger. Then the fluid makes 180° turn around and flows back through the water beamstop to the outlet.

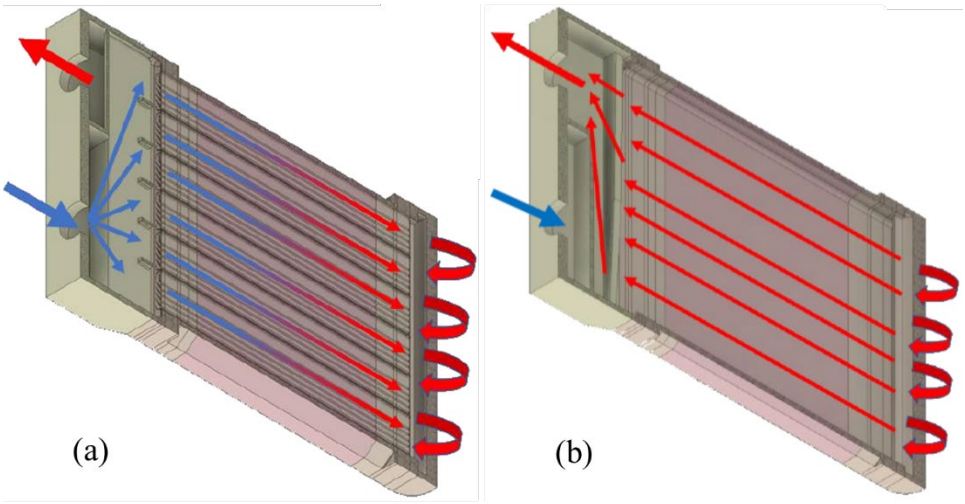

Figure 6. 3 Cooling circuit of the target (a) in the neutron producing tantalum part (b) in the beamstop. The blue arrows show the direction in which water enters the target. The red arrows show the direction in which water flows out of the target [105].

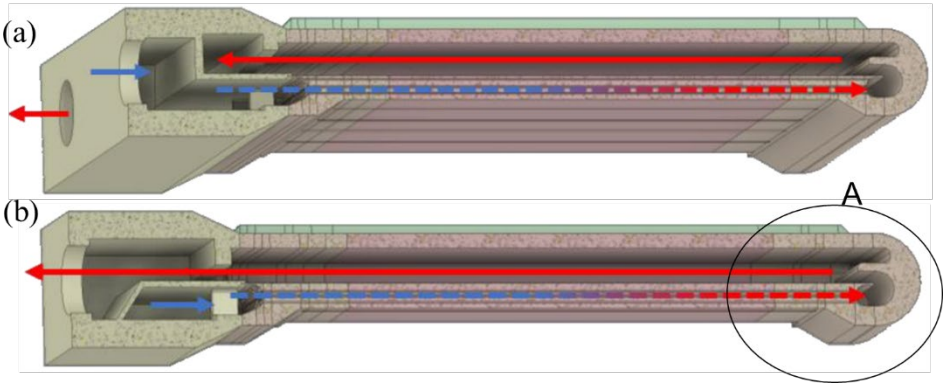

Figure 6. 4 Cooling circuit of the target in side views. The blue arrows show the direction in which water enters the target. The red arrows show the direction in which water flows out of the target [105].

Figure 6.5 shows that the schematic representation of velocity profiles in the beamstop with (a) a simple turnaround and (b) an optimized turnaround. To show the turnaround, the cross-sectional geometry in Figure 6.5 is a partial enlargement of the right-hand part A of Figure 6.4. Likewise, the coolant water enters into the microchannels and then flows through the turnaround and finally goes out in the beamstop as described in Figure 6.3 and 6.4. For a simple 180° turnaround presented in Figure 6.5(a), the velocity at the target interface was unsatisfactory due to low velocities. The improved turnaround design is shown in Figure 6.5(b). The main effect of the improved turnaround design is to increase the velocity close to the wall and to avoid a large recirculation zone at the surface due to the turnaround.

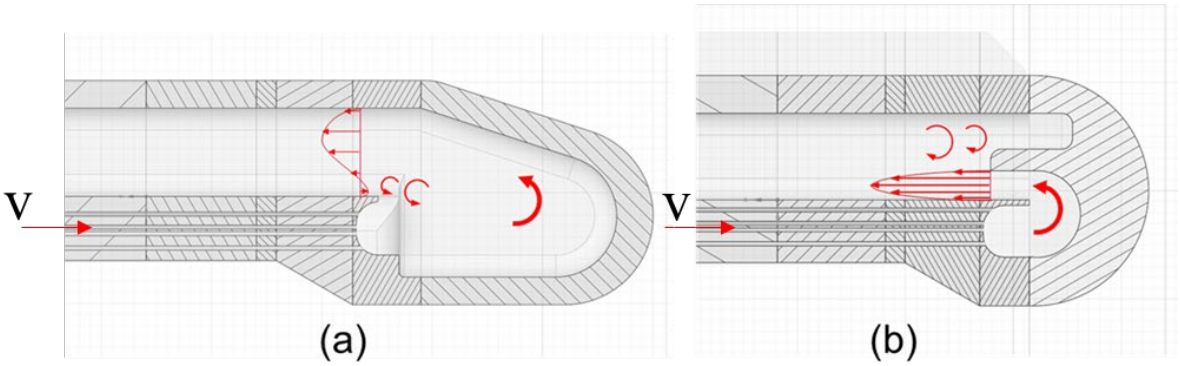

Figure 6. 5 Schematic representation of velocity profiles in the beamstop with (a) a simple turnaround and (b) an optimized turnaround. The red arrows show the direction of the water flow [105].

6.2 Steady state operation

Steady state models are based on the assumptions that all flow conditions and properties of the system are constant with respect to time, i.e. all the simulations in this section are based on a constant heat flow. A steady-state flow simulation can generally save a lot of computer resources and CPU time but also provide reliable values to some extent. This work hence firstly performed steady state simulation for the optimized target.

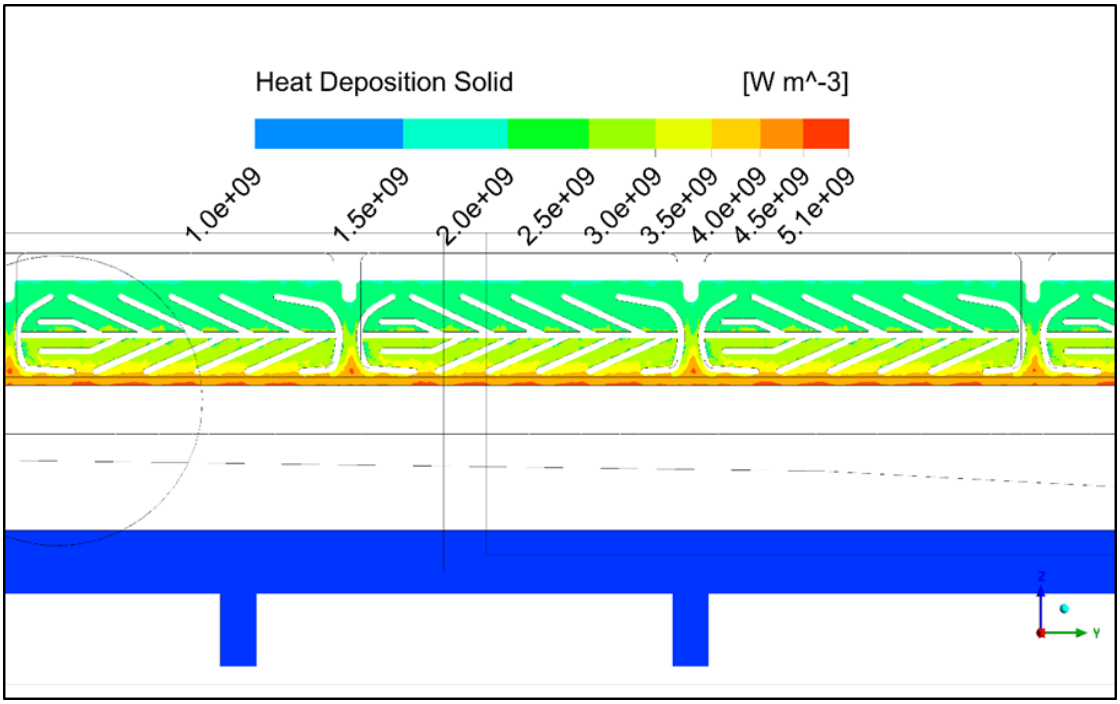

Figure 6. 6 Heat deposition of the optimized target imported from FLUKA simulation [105].

Figure 6.6 illustrates the time-averaged heat depositing of the protons in the optimized target, which is imported from energy deposition of protons obtained from FLUKA simulation. It can be seen from the graph that most heat is deposited at the lower side of the target. One thing should be mentioned is that the total amount of heat load converted from FLUKA to CFD is 121 kW instead of 100 kW (nominal value) due to some interpolation inaccuracy, like for example for mixed fluid-solid cells in FLUKA. In this case, all the ANSYS simulations are on a conservative side. Partial parameters used for CFD steady state simulations are summarized in Table 6.3.

Table 6. 3 Partial parameters used for CFD steady state simulations.

Parameters	Values
Coolant mass flow rate	1.33 kg/s
Outlet pressure	3 bars
Inlet temperatures	20 °C
Heat deposition solid	115 kW
Heat deposition fluid	6 kW
Total heat deposition	121 kW
Total heat deposition (nominal)	100 kW

6.2.1 Temperature and pressure

This mechanical optimization always starts with CFD simulations, from which one gets the temperature and pressure distributions. Because these are the necessary boundary conditions for the subsequent mechanical finite element simulation (FEM-simulation) [107]. Fig.6.7 and Fig.6.8 respectively show the solid and metal-fluid interface temperature distribution of the optimized target. According to the temperature distribution, the maximum solid temperature is 115 °C and the maximum interface temperature is 103 °C. The temperatures at the inlet and outlet are 20 °C and 42 °C respectively.

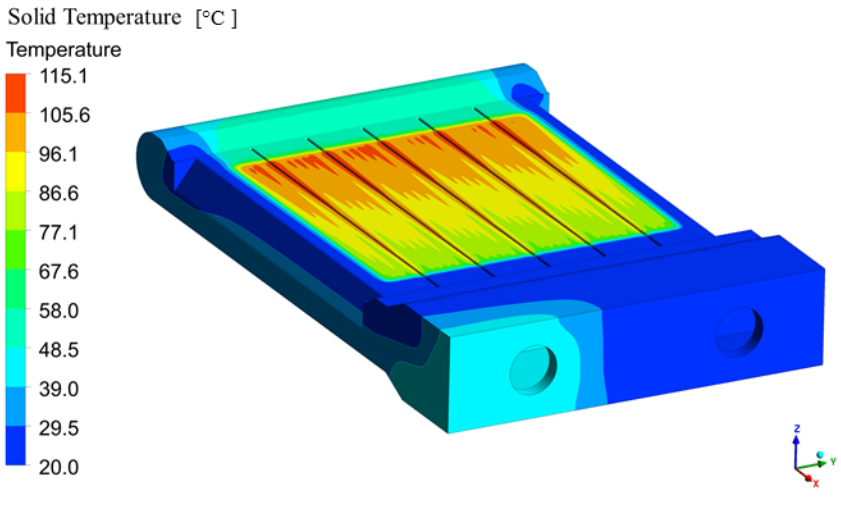

Figure 6. 7 Solid temperature of the optimized target under steady state simulations [105].

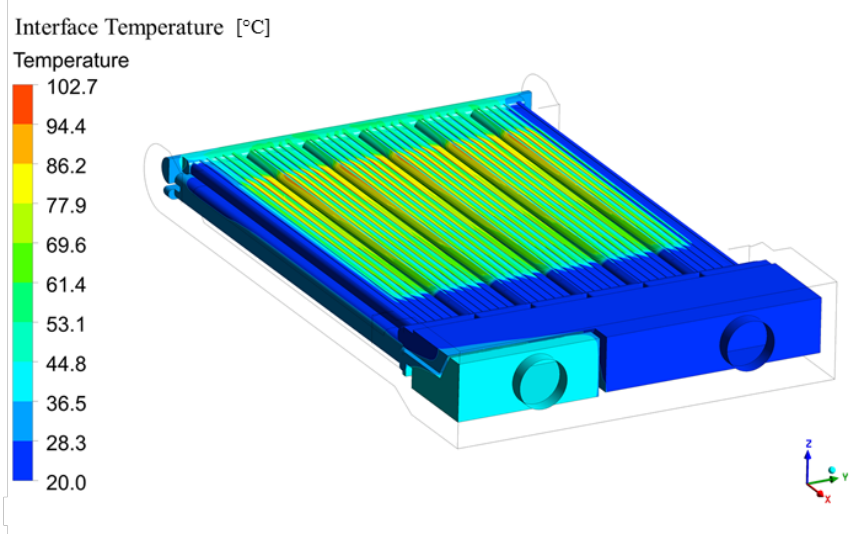

Figure 6. 8 Interface temperature of the optimized target under steady state simulations [105].

The steady-state pressure distribution is shown in Fig.6.9 with respect to the optimized target. The mean pressure at the inlet is about 6.4 bar and hence the pressure drop within the target is 3.4 bar. The pressure varies significantly along the small microchannels while it is almost constant in the beamstop, which is slightly above 3 bar and this is the most relevant pressure for the mechanical loads. The coolant first enters the microchannels with a mean pressure of 6.5 bar, and hence the pressure drop within microchannels is about 3 bar. The pressure drop within the 180° turnaround adapter is about 0.5 bar. The pressure within the beamstop is almost constant at 3 bar due to the large free flow cross section and hence the low velocity inside the beamstop.

The high pressure inside the microchannels in combination with the low thickness of the surrounding walls causes high mechanical loads which is counteracted by adjusting the width of the single microchannel segments within the optimization process. The lower pressure inside the beamstop in combination with the thicker beamstop back cover however causes strong mechanical loads as well due to the longer width of the beamstop. These mechanical loads are counteracted by several measures such as adding the ribs (see Figure 6.2) at the back wall and adjusting the thickness of the tantalum back cover itself.

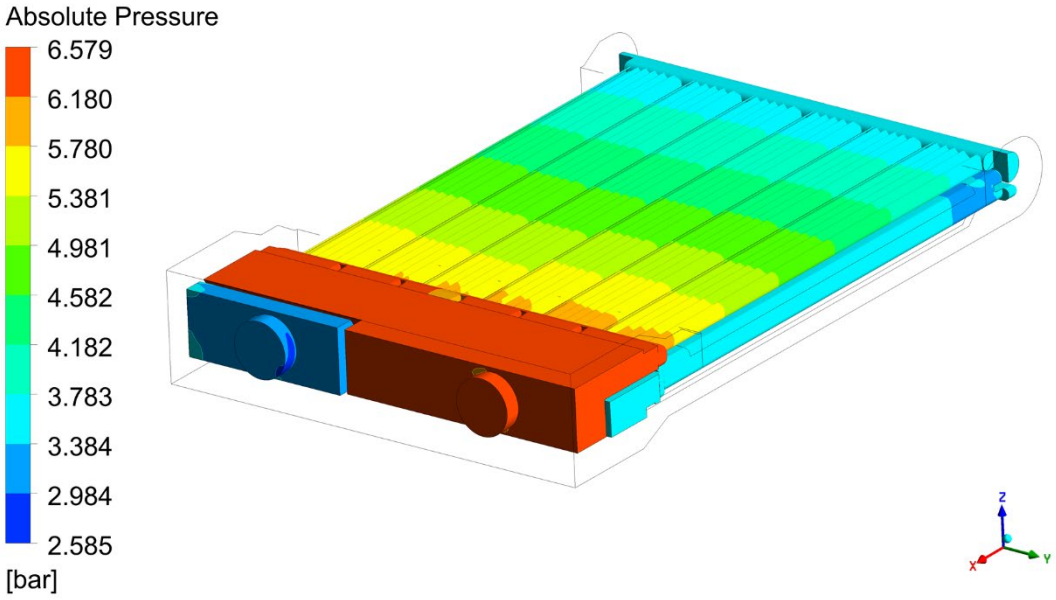

Figure 6. 9 Pressure distribution of the optimized target under steady state simulations [105].

6.2.2 Heat flux

Heat removal is one of the most important factors which limits the target performance. Thus, this work also investigates the heat flux at the interface between tantalum and coolant water. As shown in Fig.6.10, the maximum interface heat flux which occurs at the optimized target is 3.3×10^6 W/m^2 under the steady state operation condition. This is a factor of 3 lower than the heat flux of 1.1×10^7 W/m^2 which is already achieved on the first target at the last JUDITH experiment. It can be inferred that the high interface heat flux is not a problem for the cooling channels of the optimized target. And there exists a quite sufficient safety margin against burn-out of the optimized target.

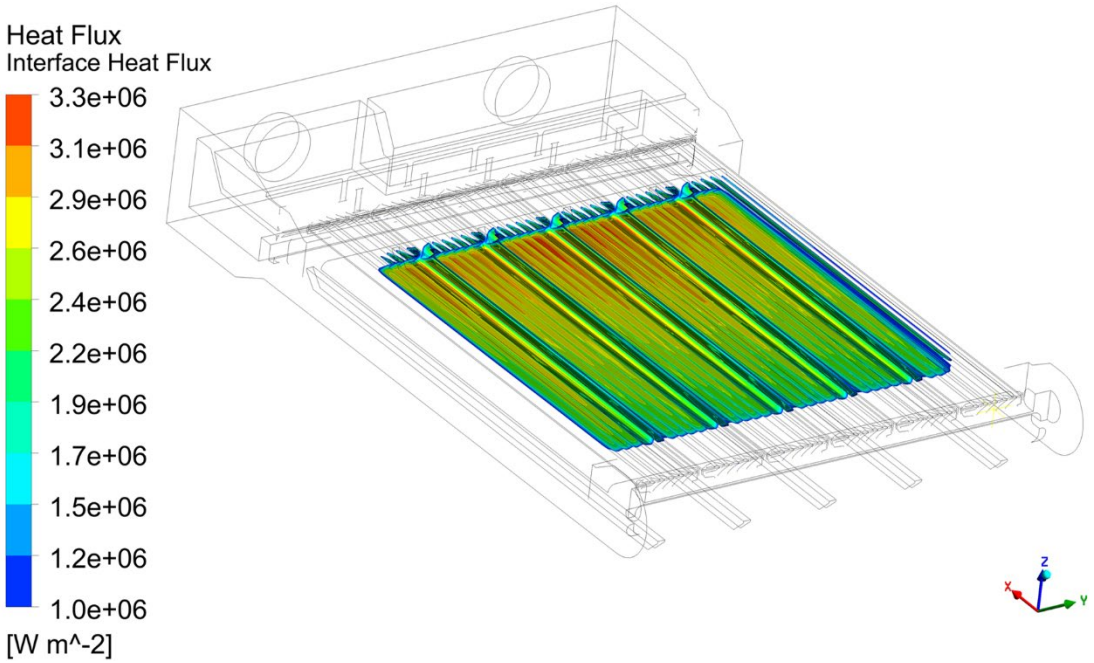

Figure 6. 10 Heat flux at the channel interfaces of the optimized target under steady state simulations [105].

6.2.3 Stress and strain

The estimation of stress and strain of the optimized target began with a pure mechanical simulation based solely on pressure and not temperature. The tantalum target is assumed to be at the state of linear elasticity. The distribution of equivalent stresses induced by pure pressure loads in the optimized target surface is depicted in Fig.6.11. At first glance, the maximum of the equivalent stress in the optimized target reaches 450 MPa according to the color bar. However, most stresses in the target surface are lower than the assumed yield stress of 185 MPa.

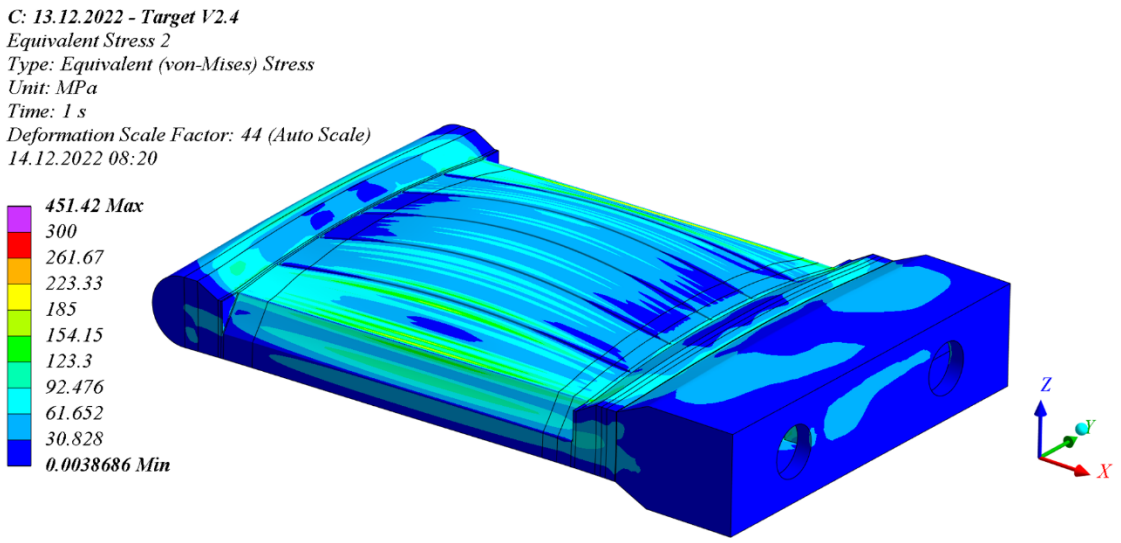

Figure 6. 11 Equivalent stresses (linear elastic) of the optimized target at target surface under pressure loads [105].

To be more specific, Fig.6.12 describes the distribution of equivalent stresses of the optimized target under pure pressure loads at channel interfaces. It can be observed that most stresses are very local and the higher values are always at the end of the microchannels. The maximum stress of 450 MPa occurs only once at the end of microchannel structure.

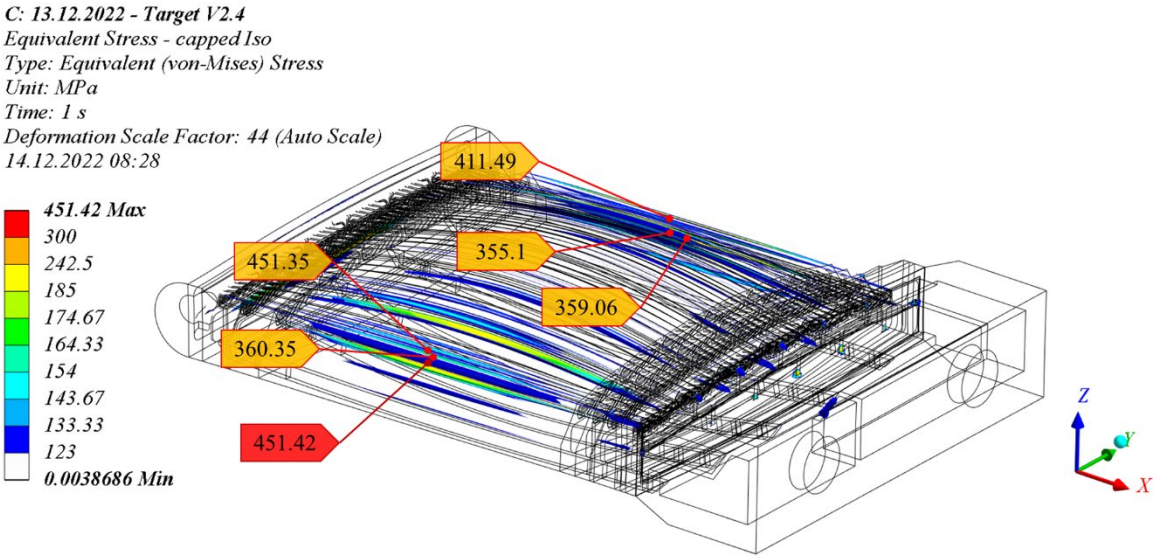

Figure 6. 12 Equivalent stresses (linear elastic) of the optimized target at channel interfaces under pressure loads [105].

In addition, a section diagram (see Figure 6.13) was made to present concretely the distribution of equivalent stresses in the cross-section of the microchannel structure under pure pressure loads. According to Figure 6.13, it clearly shows most stresses in the microchannels are within the safety range and below 185 MPa. Most local high stresses occur at the tips of microchannels, and the maximum stress of 450 MPa actually appears at the point “A” which is the end of the rounded channel.

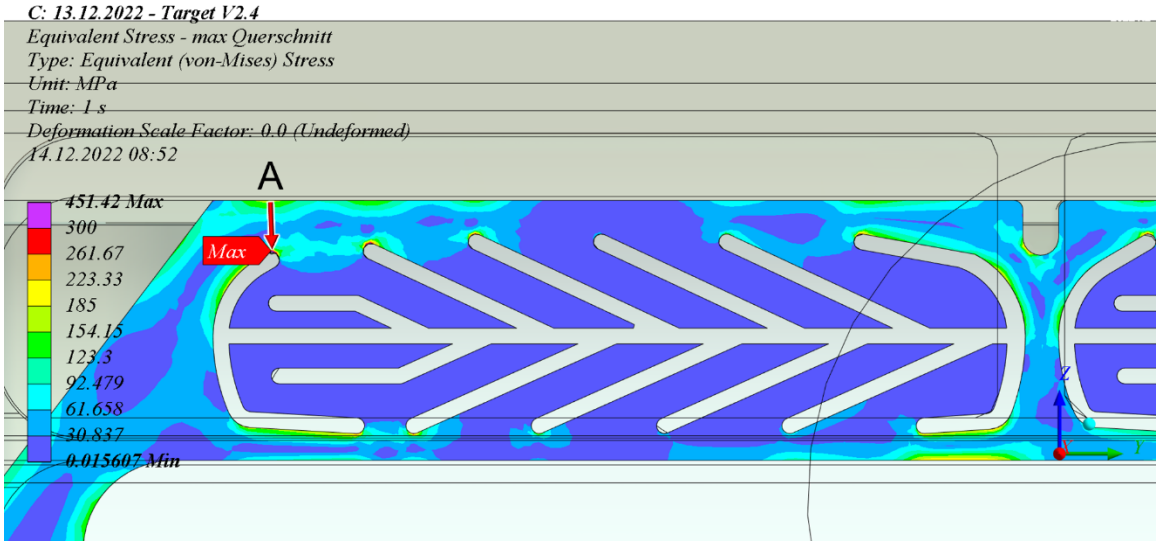

Figure 6. 13 Equivalent stress (linear elastic) distribution in the cross-section of a microchannel structure under pure pressure loading [105].

Typically, a technique so called stress linearization is used to decompose a through-thickness elastic stress field into equivalent membrane, bending, and peak stresses for comparison with appropriate allowable limits. It is usually carried out at the point of maximum stress and on the shortest path through the material. Correspondingly, the maximum stress at the point “A” (see Figure 6.13) along the path is divided into three parts as shown in Figure 6.14. The first one is membrane stress described in blue, which is the average stress through the thickness and it is a constant over the entire path. Theoretically, membrane stresses are most relevant because collapse will occur once the yield stress (185 MPa) is reached (if no material hardening is assumed). However, this membrane stress is just 22 MPa, which is quite low. The second part is the so-called bending stress depicted in dash orange, which is the linearly varying through the thickness. The bending stresses are also relevant because a plastic hinge can form and will also lead to collapse.

According to the dash orange line in Figure 6.14, the bending stress has a maximum value of 166 MPa, which is also below the yield stress of 185 MPa. Besides, there are some reserves between reaching the yield stress at the outer fibers of the cross-section and plastic collapse (for a rectangular cross-section the factor is 1.5). The peak stress of the remaining part is the total stress minus the membrane plus bending stress, which is neither linear nor constant along the path. Although peak stresses will be compensated by small plastic deformations and are not critical with respect to plastic collapse, it can be vital with regard to fatigue. Hence, further look is necessary at this.

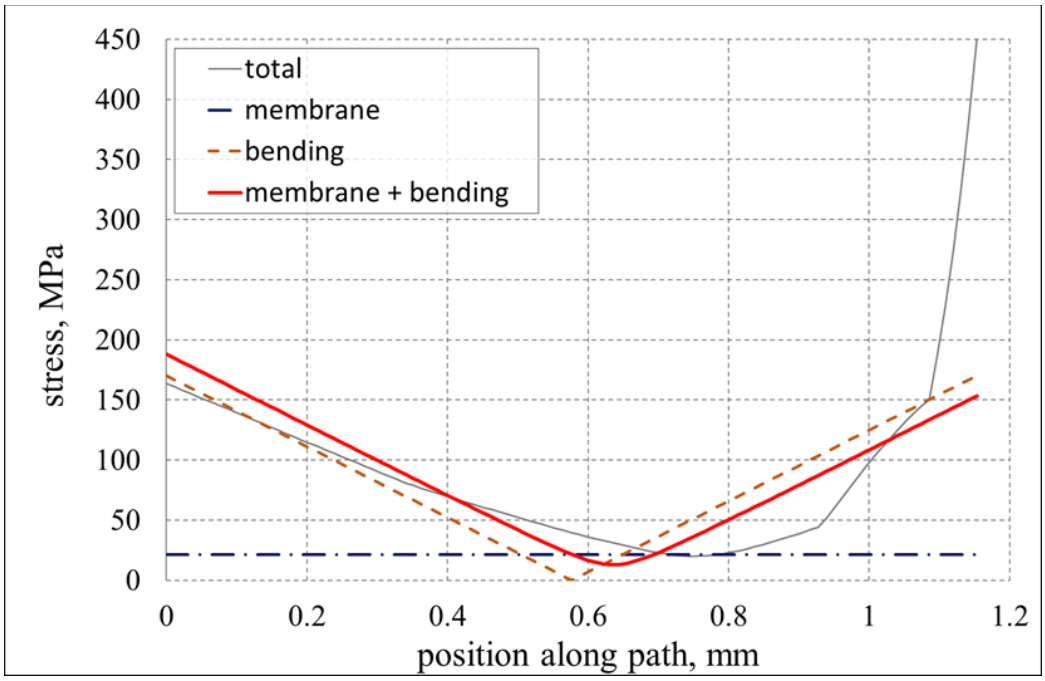

Figure 6. 14 The linearization of the equivalent stress (linear elastic) at the point of "A" [105].

First, equivalent stresses (linear elastic) of the optimized target on the target surface under thermo-mechanical loads are displayed in Figure 6.15. When compared to the corresponding stresses shown in Figure 6.11, it shows that the maximum stress somewhat decreases to 421 MPa when the heat and pressure effects are both included. Thus, it appears that the mechanical stresses are somehow counteracted by the temperatures. In some areas, the total stresses will be mitigated by the superposition of primary and secondary stresses. This is done for all components of the stress tensors with correct signs and afterwards the equivalent stress is determined.

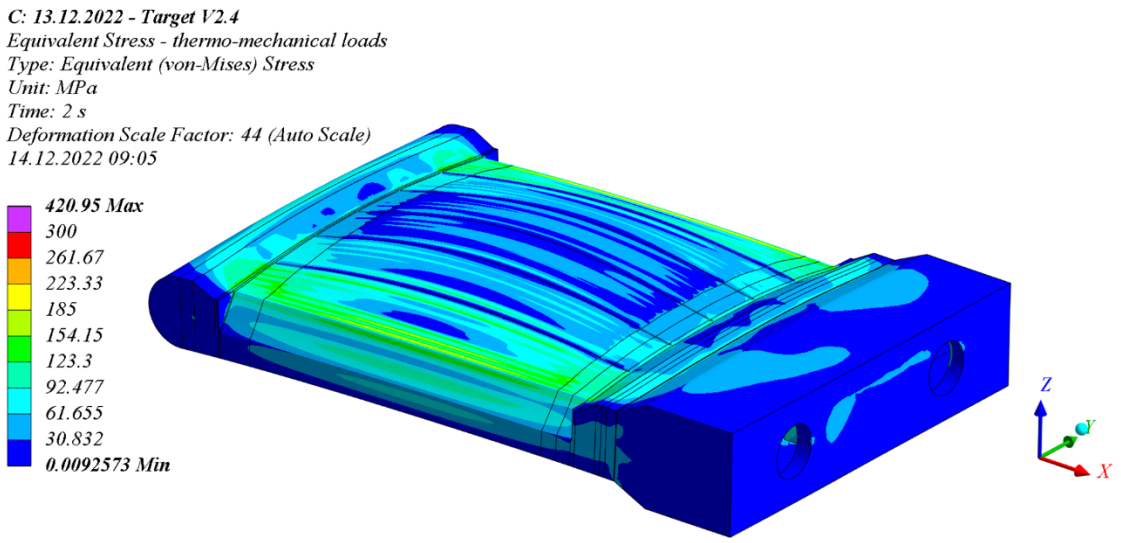

Figure 6. 15 Equivalent stresses (linear elastic) of the optimized target at target surface under thermo-mechanical loads [105].

Figure 6.16 shows the distribution of equivalent stresses of the optimized target under thermo-mechanical loads at channel interfaces. Analogously, when the impacts of heat are taken account into pressure effects, most local stresses go down and the maximum at the end of the microchannels also slightly drops to 421 MPa when compared to the comparable stresses illustrated in Figure 6.12.

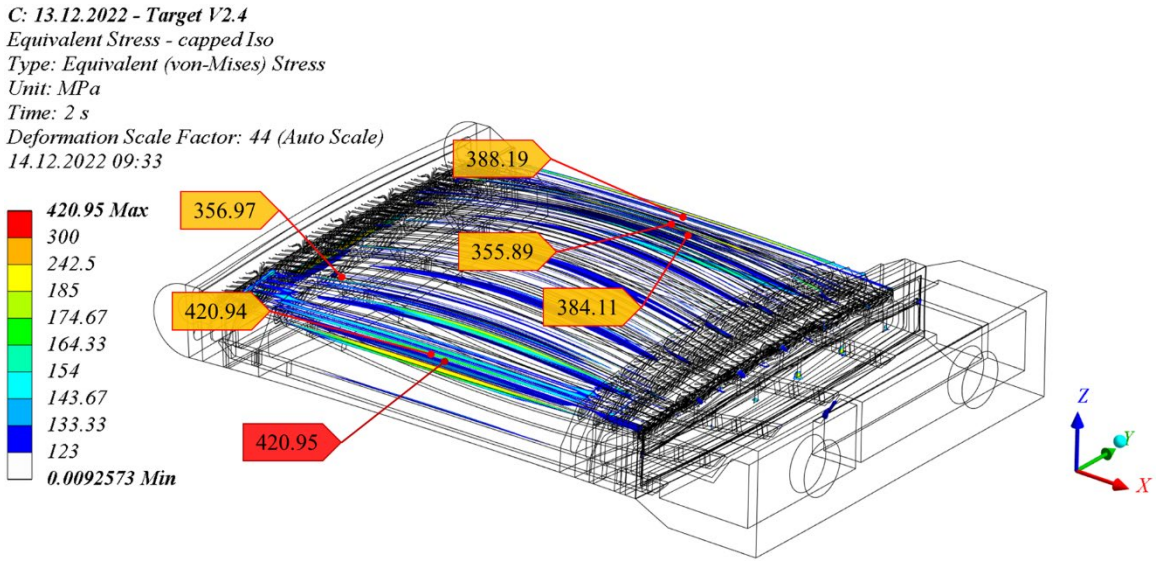

Figure 6. 16 Equivalent stresses (linear elastic) of the optimized target at channel interfaces under thermo-mechanical loads [105].

Analogously, the cross-section graph (see Figure 6.17) was drawn to present a specific view of the distribution of equivalent stresses in the cross-section of the microchannel structure under thermo-mechanical loads. According to Figure 6.17, most stresses in the microchannels are within the safety range and below the yield stress of 185 MPa. Compared with Figure 6.13 (equivalent stress (linear elastic) distribution in the cross-section of a microchannel structure under pure pressure loading.), most of the local high stresses occurring at the tips of microchannels become lower. Besides, the maximum stress occurring at point "A" was reduced to 421 MPa.

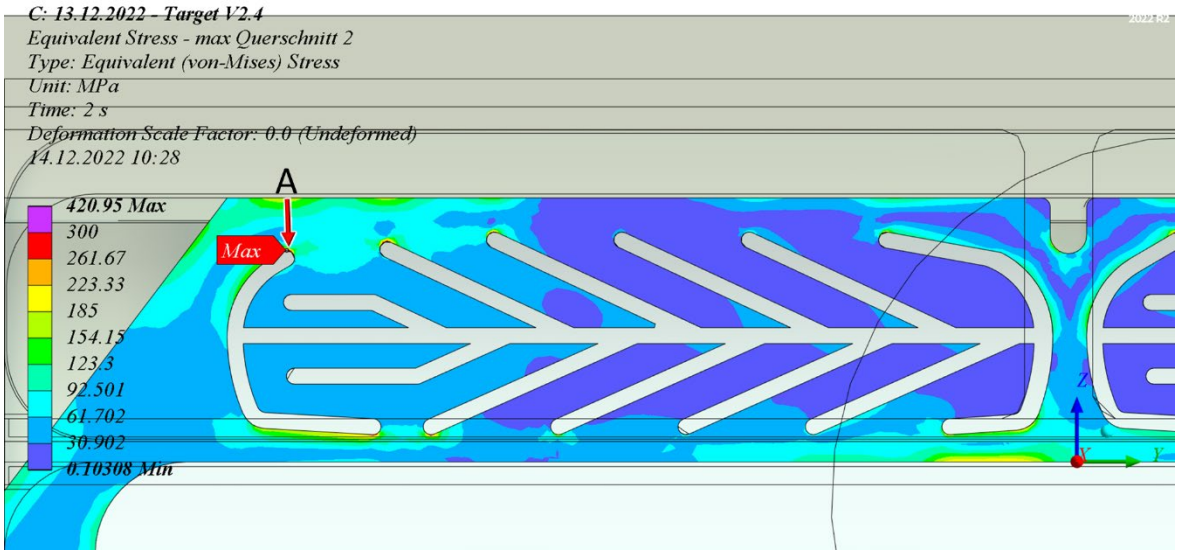

Figure 6. 17 Equivalent stress (linear elastic) distribution in the cross-section of a microchannel structure under thermo-mechanical loads [105].

As a very high local stress maximum can be significantly reduced by a relatively small plastic deformation, a simulation with an elastic – ideal plastic material model has been performed. Figure 6.18 presents the equivalent plastic strain (elastic-ideal plastic) of the optimized target under pure mechanical loads. As can be seen in Figure 6.18, the highest deformation due to local stress occurs at the end of the microchannel, reaching a maximum plastic deformation of 0.23%, which is very small and well below 1% if the yield stress is in the range of 185 MPa [104]. As tantalum is a ductile material, there is absolutely no problem. Besides, it is self-evident that stresses are limited to the yield stress if an ideal-plastic material behavior is assumed. Therefore, this is not a "safe" limit but the plastic deformations have to be assessed to be "safe".

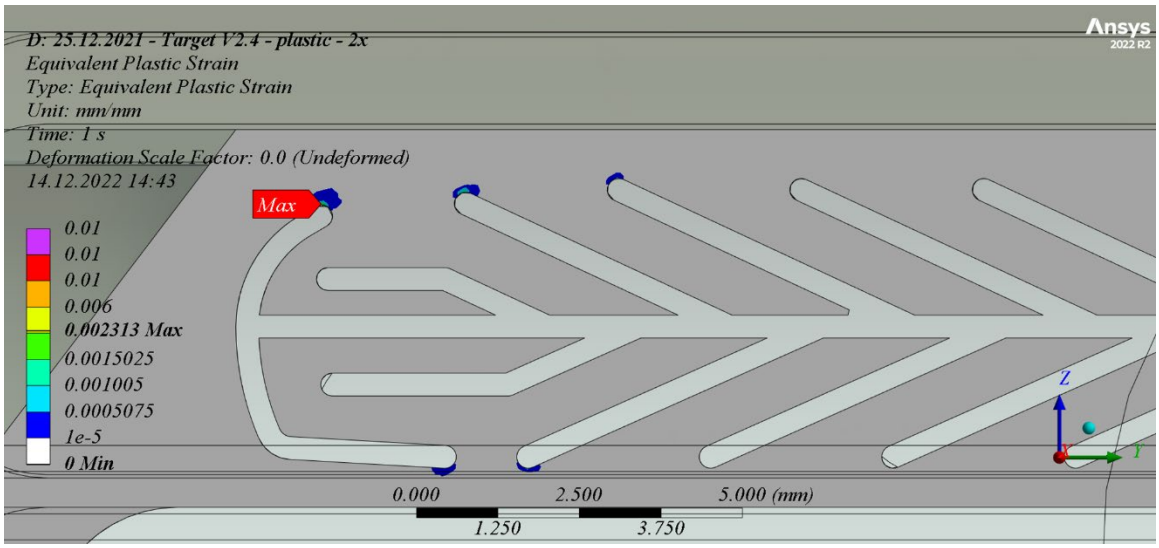

Figure 6. 18 Equivalent plastic strain (elastic-ideal plastic) distribution in the cross-section of microchannel structures under mechanical loads [105].

In addition, this work also performed a simulation with the pressure load doubled and without the temperature load, which is a very conservative estimation. But even with the twofold pressure, small plastic deformations are able to reduce the stresses to the allowed limits. Figure 6.19 depicts the equivalent plastic strain (elastic-ideal plastic) distribution in the cross-section of microchannel structures of the optimized target under double mechanical loads. It is able to observe that the most of deformations because of the local stresses mainly distribute at the end of microchannels, and the vulnerable area of the target concentrates on the end part of the microchannel structures. However, despite a maximum plastic deformation of 4.03% at twice the pressure load, the target was not destroyed.

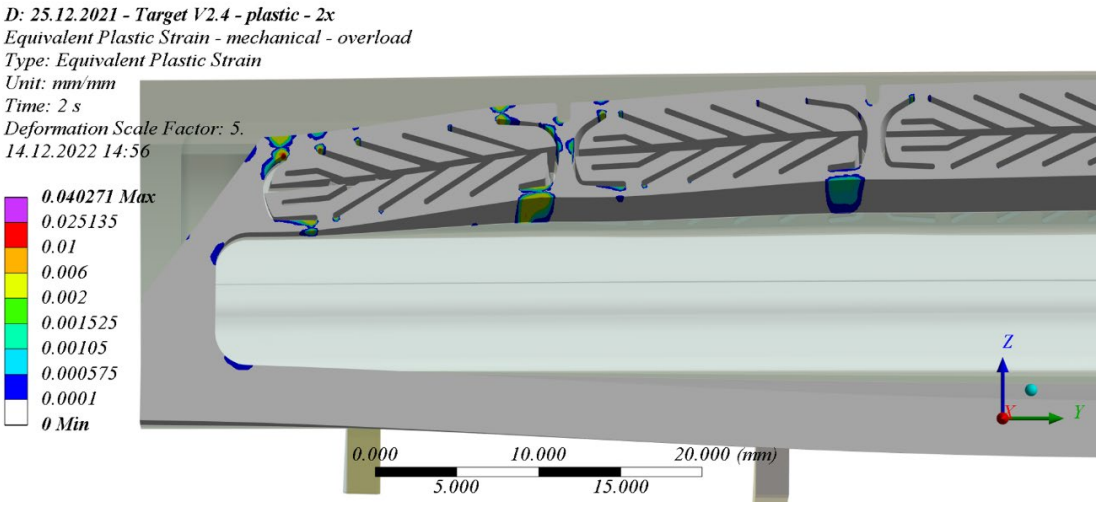

Figure 6. 19 Equivalent plastic strain (elastic-ideal plastic) distribution in the cross-section of microchannel structures under double mechanical loads [105].

In order to find out the limit of mechanical load of the target, a simulation of plastic collapse has been performed as well. It turns out that the safety factor against plastic collapse due to mechanical loads is about 8.9. Figure 6.20 shows the equivalent plastic strain (elastic-ideal plastic) distribution of the optimized target during plastic collapse. There is significant deformation of the target in the z-direction due to the water pressure, with the maximum deformation marked in red occurring at the end of each microchannel structure, i.e. the ends of each microchannel structure are the critical areas.

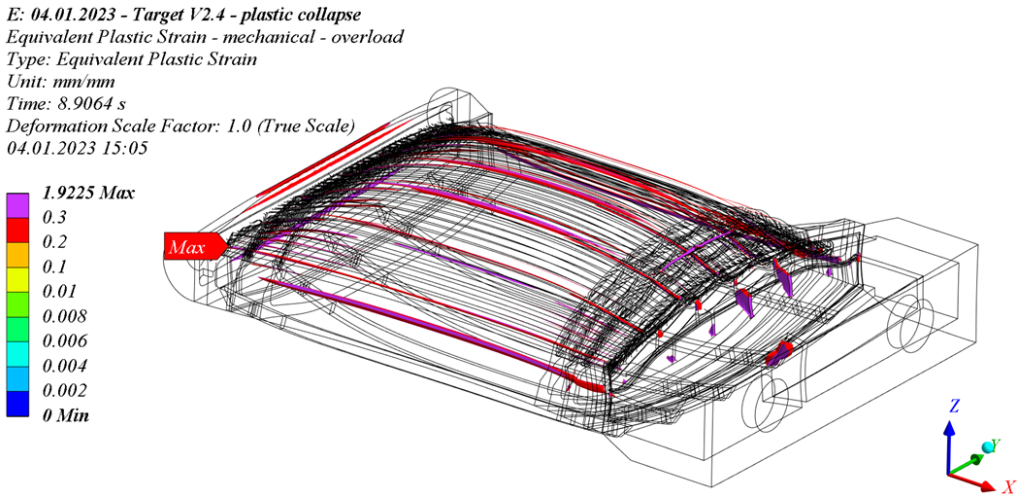

Figure 6. 20 Equivalent plastic strain (elastic-ideal plastic) distribution of the optimized target at plastic collapse under pure mechanical loads [105].

In addition, this work also performed simulations to determine the safety load factor against the fracture strain. Figure 6.21 shows that the equivalent plastic strain (elastic-ideal plastic) for reaching elongation at break [107] at a load factor of about 2.8. Partial enlargement of the right-hand side of Figure 6.21 clearly illustrates that the maximum deformation takes place in the thin "bridge" part which is between the individual microchannel structures. Although the load factor for plastic collapse was 8.9, the maximum equivalent plastic strain will reach the elongation at brake for a load factor of about 2.8.

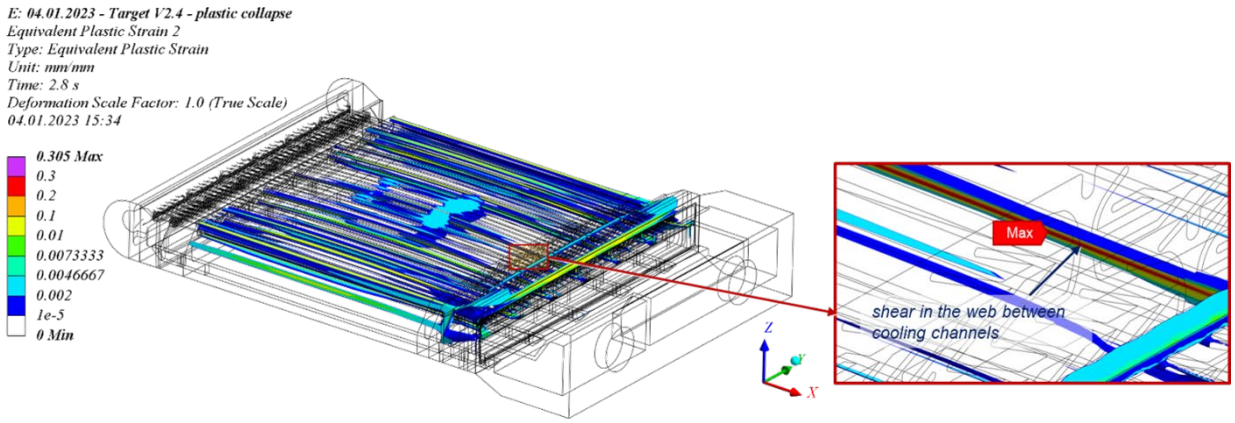

Figure 6. 21 Equivalent plastic strain (elastic-ideal plastic) reaching elongation at break [105].

6.3 Pulsed operation

This work also did simulations on transient flow condition because the HBS target will be operated with a pulsed proton beam. Transient (unsteady) models can handle conditions that change with time and assess the time-dependent impact on thermal and flow predictions. Since postprocessing of such a big model is really time-consuming, just the most relevant results with respect to temperatures and heat fluxes occur at one certain timepoint are investigated (e.g. the situation at the beginning of a new pulse or the state at the end of one pulse). The pulse frequency used in the simulation is 24 Hz.

6.3.1 Temperature

Figure 6.22 and Figure 6.23, respectively, shows the solid and metal-fluid interface temperature of the optimized target at the end of 10th pulse. The temperature maps show that the highest solid

temperature is 151.1 °C and the maximum interface temperature is 151.1 °C as well, which a little differs from the comparable values under steady state operation presented in Figure 6.7 and Figure 6.8. The main cause is the high heat deposition during the pulse and the resulting temperature increment.

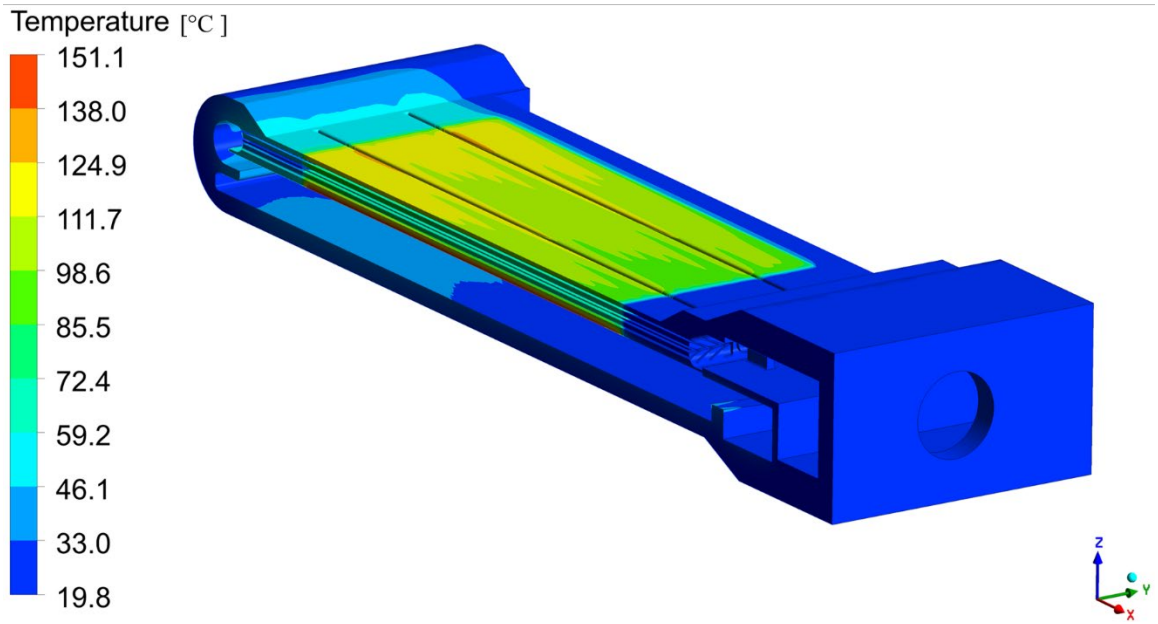

Figure 6. 22 Solid temperature of the optimized target at the end of 13th pulse [105].

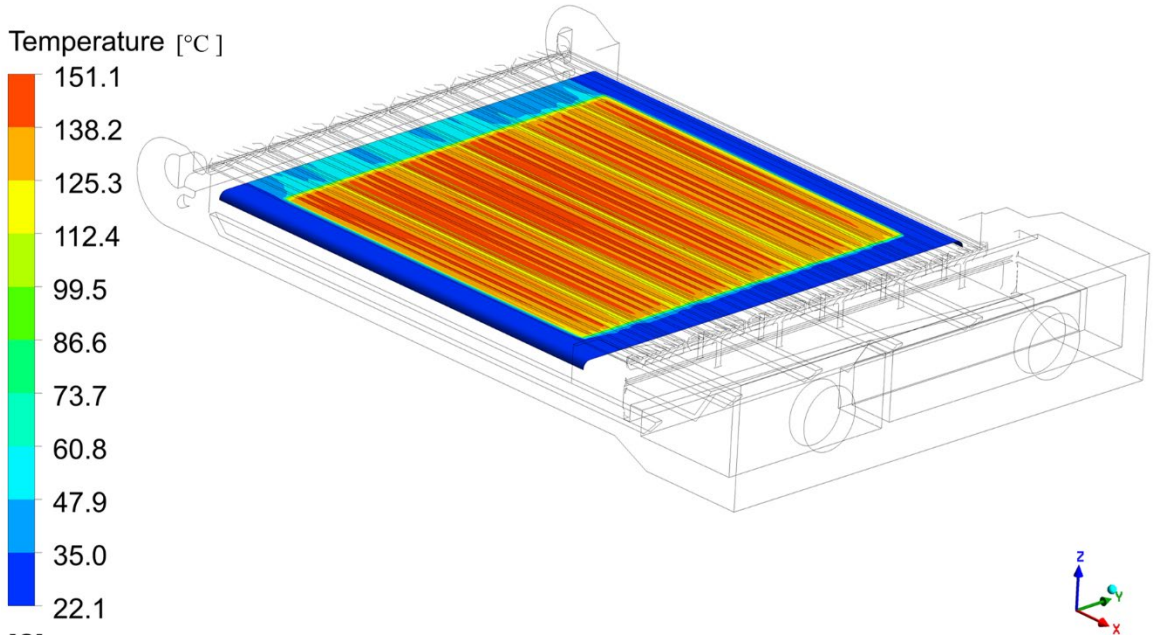

Figure 6. 23 Beamstop interface temperature of the optimized target at the end of 13th pulse [105].

In addition, the transient temperature change across a 24 Hz pulse operation was also assessed in this work. Correspondingly, Figure 6.24 records the transient temperature of the optimized target during the operation of 13 pulses. The maximum solid temperature depicted in red demonstrates that during the first three pulses, the heat deposition continually switches from a steady state to a pulsed state. Besides, according to the outlet temperature in blue, it takes about 3 pulses till the outlet temperature starts to increase significantly and then steadily increases to 40 °C before almost reaching a thermal equilibrium condition after 13th pulse. However, the outlet temperature actually starts to rise even during the first pulse, but the values are quite low due to thermal inertia. The outlet temperature of 40 °C at the thermal equilibrium condition is consistent with the result obtained from the steady state simulation, although there is still a small deviation in the energy balance between the steady state simulation.

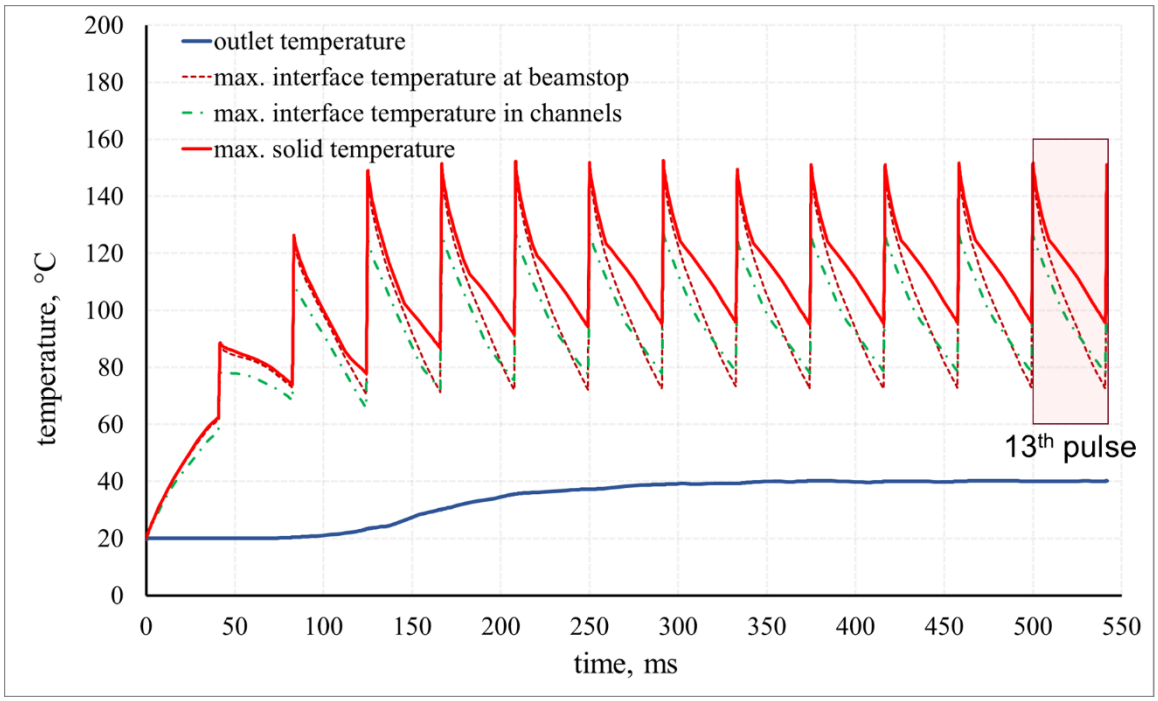

Figure 6. 24 Transient temperature of the optimized target during pulse operation [105].

In order to get further details, the transient temperature results at the 13th pulse of the optimized target magnified locally as shown in Figure 6.25. As can be seen in the dark red dash line, the maximum interface temperature occurs at beamstop when operated to 13th pulse. Additionally, at the end of a pulse the solid red line of maximum solid temperature coincides with dark red dash line of maximum interface temperature at the beamstop, when the maximum interface temperature

at the beamstop of 151.1 °C is also the maximum solid temperature of the optimized target. The green dash curve indicates that the maximum interface temperature within the microchannels is about 124.9 °C, which is much lower than the boiling temperature of 155 °C at 5 bar [86] (water pressure inside the microchannels, see Figure 6.9). Therefore, boiling can be avoided within the channels. However, the maximum interface temperature at the beamstop is up to 151.1 °C, which is higher than the boiling temperature of 134 °C at 3 bar [86] (water pressure at the beamstop, see Figure 6.9). As a result, boiling will occur at the beamstop interface and therefore this interface should be orientated upwards to prevent accumulation of bubbles and film boiling there.

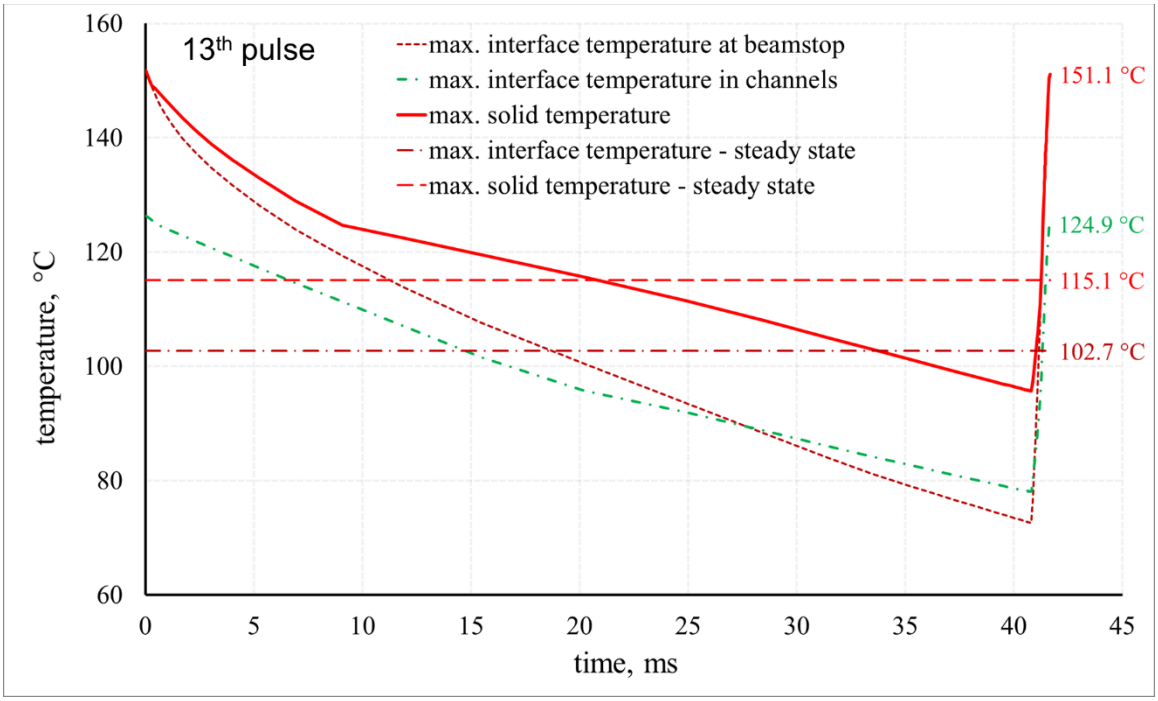

Figure 6. 25 Transient temperature of the optimized target during 13th pulse [105].

6.3.2 Heat flux

The heat flux of the optimized target on channel interfaces at the end of 13th pulse is depicted as in Figure 6.26. As can be seen, most heat fluxes at the channel interfaces are within 5.2×10^6 W/m^2. The higher heat fluxes mainly concentrate on the bridge sections between the individual microchannel structure, where the critical heat flux most likely occurs. In addition, the maximum heat flux at the channel wall is 6.3×10^6 W/m^2, which is quite high but still below the achieved power of 1.1×10^7 W/m^2 at the heat flux test of first target design.

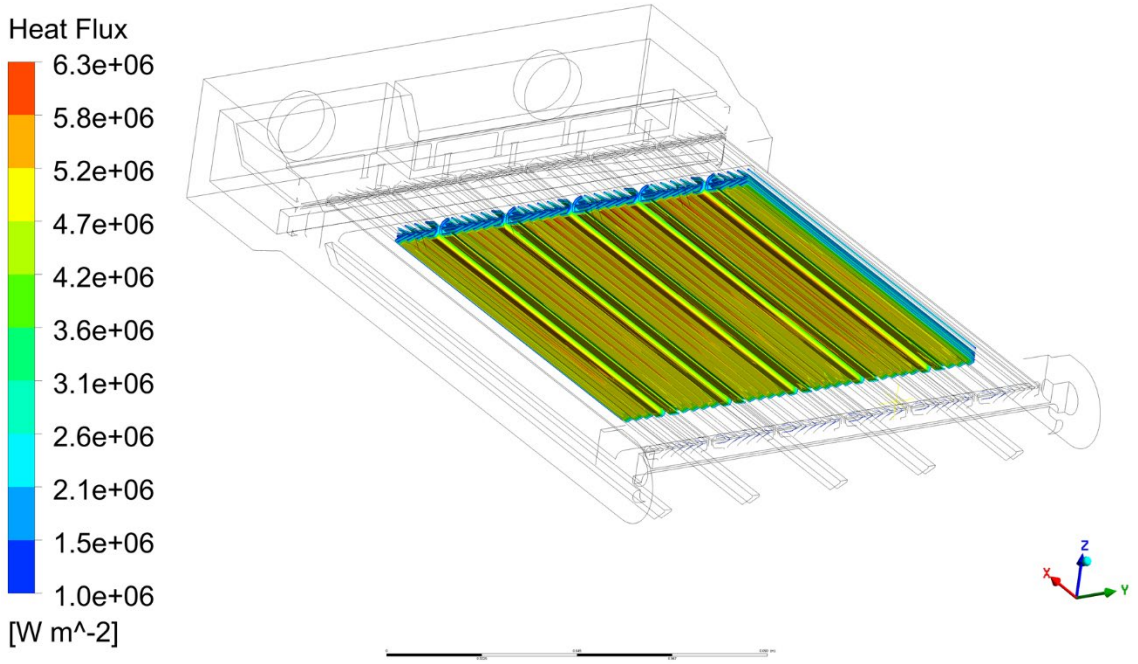

Figure 6. 26 Heat flux of the optimized target on channel interfaces at the end of 13th pulse [105].

Furthermore, the heat flux of the optimized target on beamstop interface at the end of 13th pulse is shown in Figure 6.27. As can been seen, the heat flux near the side of cooling inlet is quite low and it becomes higher towards the side of 180° turnaround. The increased heat flux close to the 180° turnaround is enforced by the special design of the turnaround with increased velocities (see Figure 6.5). Compared with the heat fluxes on channel interfaces presented in Figure 6.26, the heat fluxes on the beamstop interface are lower. The maximum heat flux on the beamstop interface is only 4.01×10^{6} W/m^2, which is also less than the maximum value appearing on the channel interfaces, which is because the beamstop interface is cooled through the water in the beamstop as well as the microchannel structures.

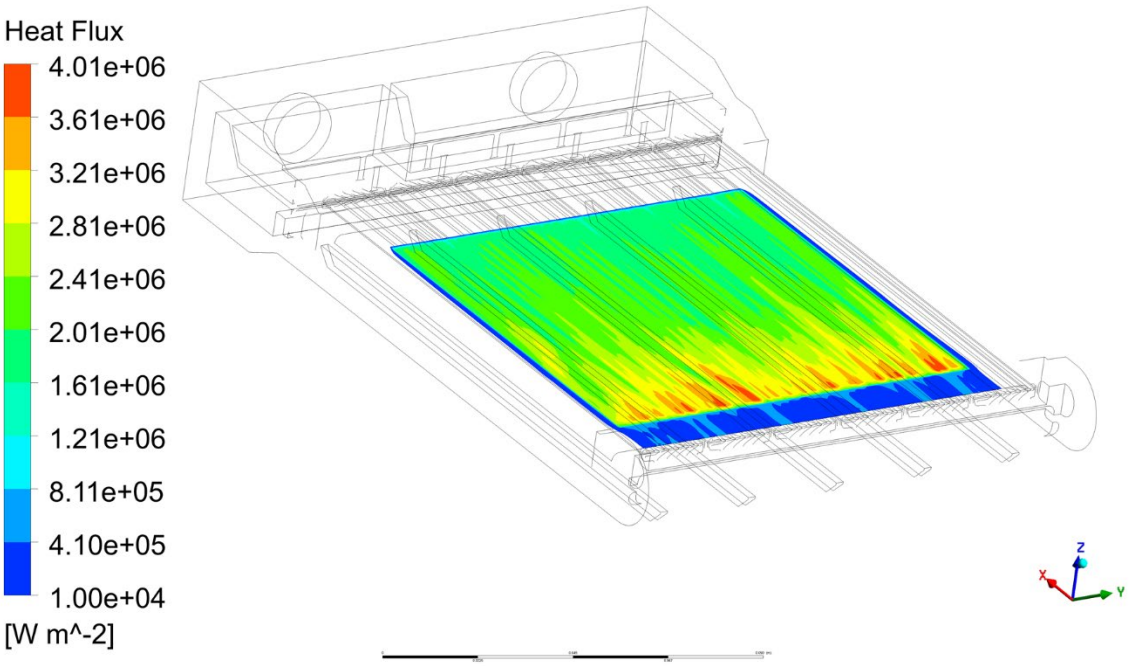

Figure 6. 27 Heat flux of the optimized target on beamstop interface at the end of 13th pulse [105].

6.3.3 Heat flow

The time-dependent heat flow in the optimized target during one pulse interval is given in Figure 6.28. According to the dotted orange line of the time-average heat flow on channel interfaces, it indicates that nearly 103.7 kW heat is dissipated through the microchannels. And the dashed blue line of the time-average heat flow on beamstop interface shows approximate 10.1 kW power is removed by the coolant in the beamstop. The dashed red curve reveals that the total heat removed by cooling water is like 114 kW. From this it can be inferred that the main contribution to the target cooling is coming from the cooling channels (~91%). The other point is that although the total cooling effect by the beamstop water is small (9%), it is still important to reduce the solid temperatures at the lower side of the target.

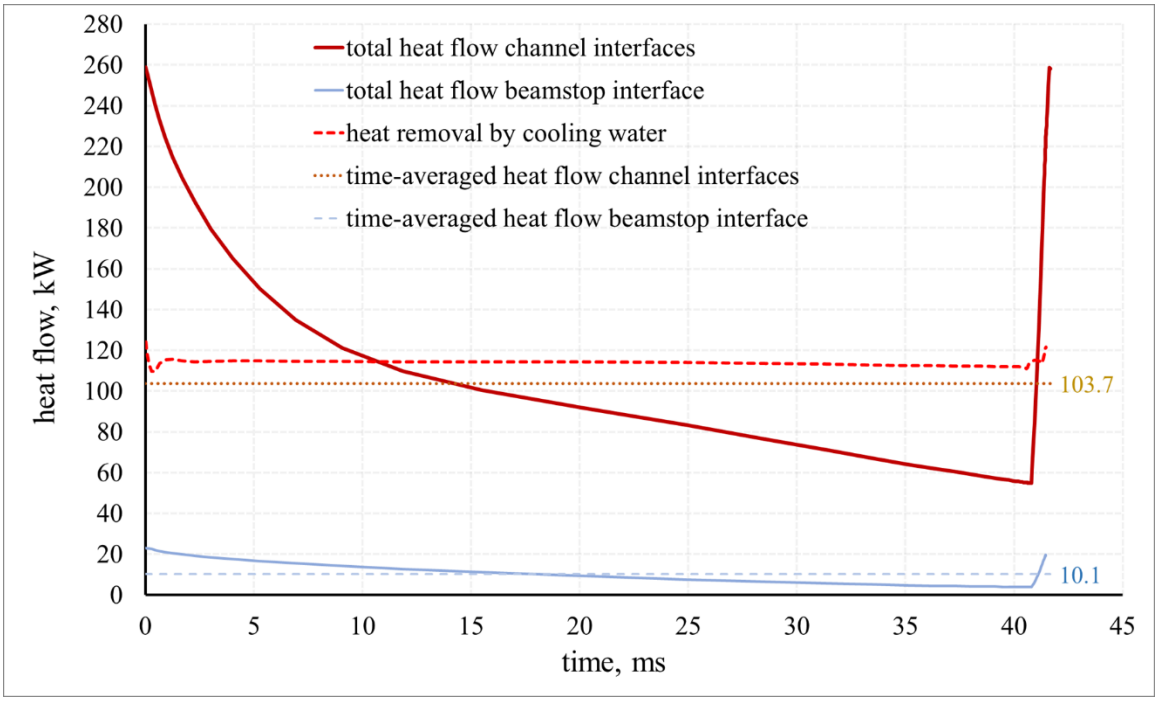

Figure 6. 28 Heat flow in the optimized target during one pulse interval [105].

6.4 Conclusions

This chapter introduces the optimized target design and the cooling circuit. The mechanical and thermo-mechanical properties of the optimized target are simulated under two flow patterns. For the steady state, the maximum interface temperature is about 103 °C and is well below the boiling temperature of 134 °C at 3 bar pressure; and the maximum interface heat flux is 3.3 $\times 10^6$ W/m^2, which is a factor of 3 lower than the heat flux of 1.1×10^7 W/m^2 achieved on the first target at the last JUDITH experiment. Hence, there exists a quite high safety margin for the burn-out of the optimized target. In addition, the simulations with an elastic-ideal plastic material model have shown that expected plastic deformations due to local stresses are very small and well below 1%, if the yield stress is in the range of 185 MPa. The safety factor against plastic collapse due to mechanical loads is quite large (factor 8.9), even without considering hardening of the material, but it should be considered that the elongation at break of the material is reached for a much lower load factor of about 2.8.

For the unsteady flow, the pulsed operation will significantly increase maximum temperatures in the target compared to steady-state conditions with a time-averaged heat deposition. The maximum interface temperature in the microchannels is about 124.9 °C, which is much lower than the boiling temperature of 155 °C at 5 bars. Thus, there will not no boiling in the microchannel structures. While at the beamstop interface boiling is expected since the maximum interface temperature at the beamstop is up to 151.1 °C, which is higher than the boiling temperature of 134 °C at 3 bars. For this, the beamstop interface should be orientated upwards to allow the vapor bubbles to separate from the surface. Finally, the maximum interface heat flux of 6.3×10^6 W/m^2 at the channel walls is quite high but most likely still below the critical heat flux.

7 Prototype Manufacturing & Testing

As presented in Chapter 5 and 6, the HBS target design was obtained with a long iterative optimization using particle transport code FLUKA and thermal-mechanical simulations ANSYS. The key part, the microchannel structure as well as the sophisticated cooling component, is the most challenging part for manufacturing. In order to verify the machinability, the manufacturing of the prototype of HBS target is presented in this chapter. The manufacturing-related tolerances were cross-checked with two different technologies, optical microscope and computed tomography (CT). The CT examination was operated at the CT laboratory of ZEA-1 of the Forschungszentrum Jülich. Feedback from the production process helps to improve the manufacturing methods and to eliminate some weak points of the prototype. In addition, the relevant impacts in particle transport properties for the target caused by the manufacturing-related tolerances were also estimated in this Chapter. This helps to determine the acceptable limitation of the tolerances and further to improve the requirements of processing methods.

7.1 Electrical discharge machining (EDM)

The selected target material for the HBS target is tantalum, but an aluminum alloy AW 6061-T6 was used for manufacturing of the prototype (see Figure 7.1) since it is much cheaper compared to tantalum. Additionally, there is not any direct physical contact between the tools and the workpiece, therefore it has no influence for the manufacturing-related tolerances even if using the other materials for the prototype manufacturing. Besides, one of the tolerance evaluation techniques in this thesis, computed tomography, is suitable for low-density materials like aluminum but not high-density materials like tantalum. The low density of the material enables easy penetration of X-rays and does not influence the attenuation of the scanned part. The density of aluminum alloy AW 6061-T6 and tantalum are 2.7 g/cm³ and 16.6 g/cm³, respectively. In addition, aluminum alloy AW 6061-T6 is much cheaper than tantalum but it still can provide valuable reference information to boost the quality of the real HBS target fabrication. The

prototype was fabricated with milling and Electro Discharge Machining (EDM), the details will be described in the following context.

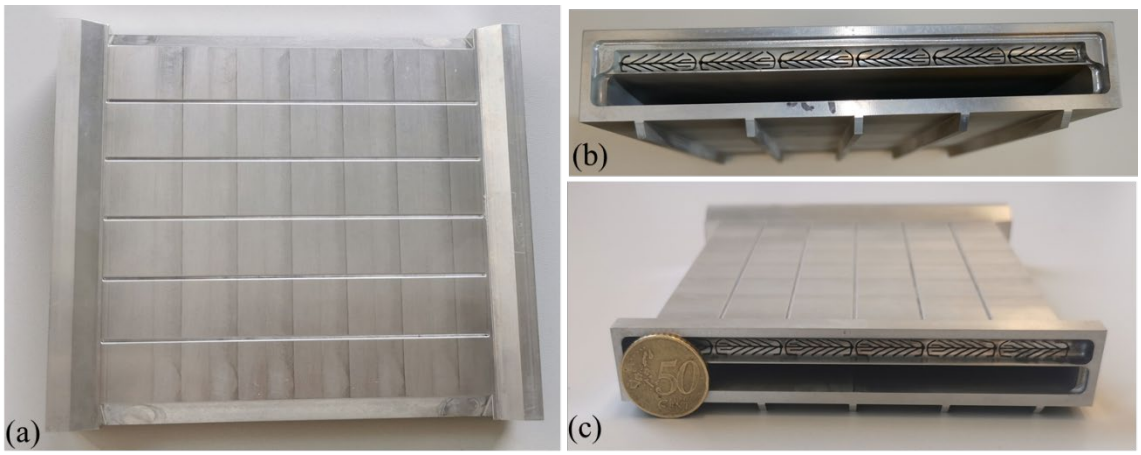

Figure 7. 1 Aluminum prototype of HBS target fabricated with milling and EDM
(a) Top view (b) Front view (c) Top-front view.

The manufacturing setup for the HBS target prototype is the wire-cut EDM machine (Figure 7.2(a)) installed at the workshop of ZEA-1. Before starting to fabricate each individual microchannel structure, some small holes were machined firstly in the rectangular aluminum block on the sinker-EDM machine. These holes were used as the starting points of each microchannel structure, i.e. the entry for the wire entering the target to fabricate the microchannel structure. The complicated microchannel structures were manufactured in the wire-cut EDM machine as shown in the Figure 7.2(a) and (b). The wire EDM machining is an electrothermal production process where a thin single-strand metal wire, along with deionized water allows the wire to cut through metal by the use of heat from electrical sparks while preventing rust. The principle can be described briefly as an electrical discharge between the wire and the work piece, i.e. aluminum metal in this context. As the spark jumps across the gap, material is then removed from the work piece and the electrode. Due to the inherent properties of the process, wire EDM can easily machine the complex microchannel structure in work piece. To stop the sparking process from shorting out, a non-conductive dielectric is also used in the process. The waste material is removed by the dielectric, and the process continues until the microchannel structures are fabricated.

(a) (b)

Figure 7. 2 (a) Wire-cut EDM machine; (b) The target is being wire-cut under EDM machine at ZEA-1.

7.2 Computed tomography test

One of the tolerance examinations of the prototype was performed with computed tomography (see Figure 7.3), which is commonly referred to as CT scanning. It has become an important inspection tool for a large number of industrial applications. CT scanning is a computer-aided diagnostic imaging technique that uses X-rays to produce images of the inside of the scanned object. Using CT scanning, one can examine and measure the external and internal structure of 3D objects without destruction. X-rays pass through the products, but they are attenuated because of scattering and absorption. The principle of CT scanning is to measure attenuation coefficient by capturing the remaining X-rays using a radiation detector, generating a series of cross-sectional, two-dimensional images of the body [108]. During the process of the CT scanning, the scanned body will be rotated and 2D images are recorded for each angle. The individual images are than reconstructed into a 3D body via the CT software (VGSTUDIO MAX 2022.1 in the investigation

of this work), which means that three-dimensional internal structures can be made visible without destroying the sample.

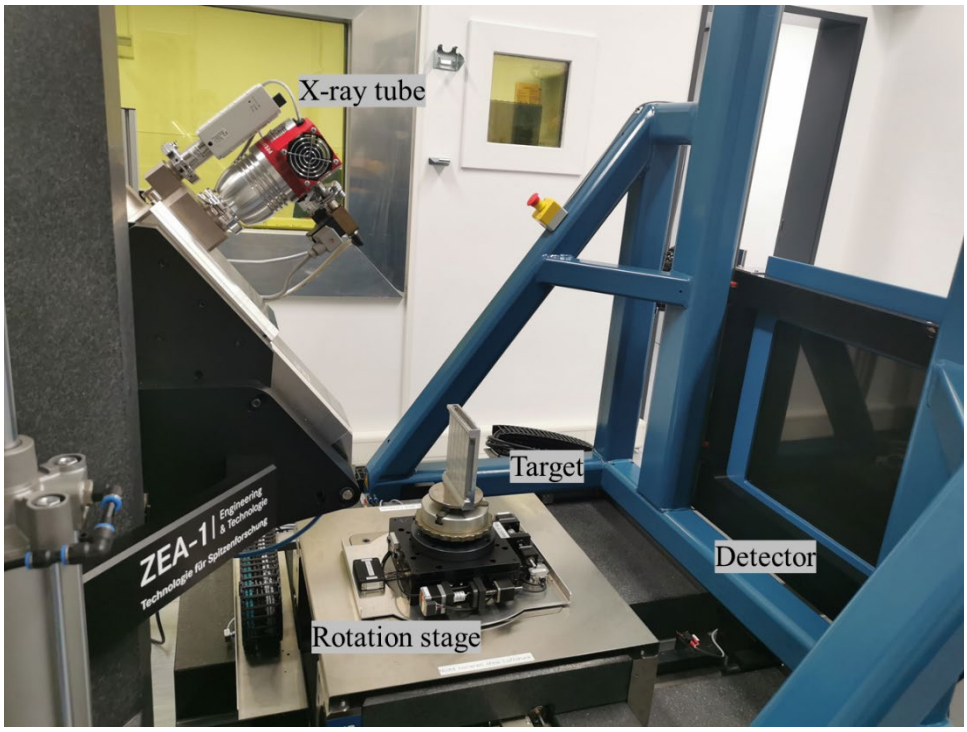

Figure 7. 3 Computed tomography at ZEA-1.

7.2.1 Measurement method

As presented in Figure 7.3, the target prototype is irradiated by the X-Ray tube while it rotates on a turntable. 2D image of the entire object for each angle is projected on the detector. The individual images are than reconstructed into a 3D body (see Figure 7.4) via the CT software. Depending on the geometry, the material to be radiographed and the power of the X-ray tube, different resolutions can be achieved. In the present case, the target used to produce X-rays in the CT machine is tungsten, the measurement time is 1.8 h in total and the detector resolution is up to 100 µm. In this respect, the resolution of the images in computed tomography is sufficient to detect the manufacturing-related tolerances. Scanning parameters which were carefully chosen by the CT operator according to the scanned material and geometry are shown in Table 7.1.

Table 7. 1 Parameter setting for the computed tomography (CT) scanning.

	Parameter	Unit
Voltage	180	kV
Current	120	μA
Power	21	W
Magnification	2.22	-
Voxel size	90	μm
Focal spot size	10	μm
Integration time	2	s
No. of projections	1080	-
Detector matrix	4096 x 4096	pixel
Pixel size	100	μm

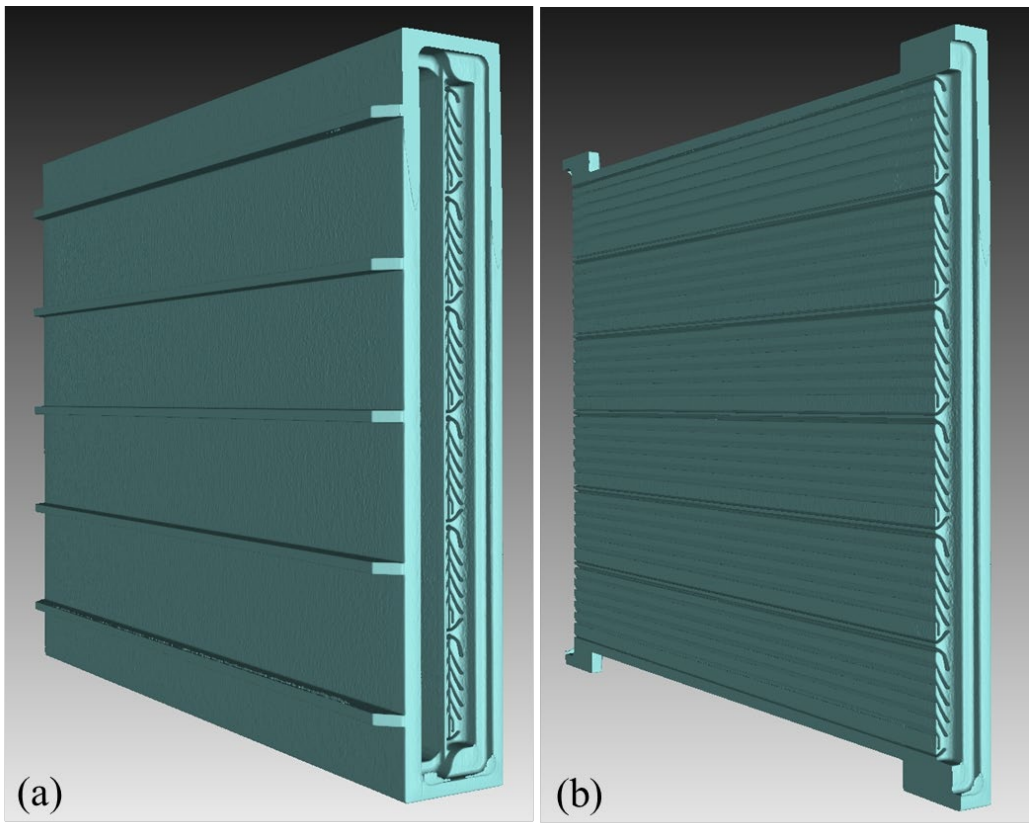

Figure 7. 4 3D computed tomography images of the HBS target prototype (a) The entire target;(b) The vertical cross-section through the microchannel structure.

A common means of quality assurance for new manufactured parts is 3D inspection, where 3D inspection software, i.e. VGSTUDIO MAX 2022.1, compares the scanned data against the CAD model. To be more specific, the manufactured product is reconstructed firstly in the software from these 2D projections. In this way, the scan data are then imported into the inspection software. The scan data of manufactured prototype is used to compare against CAD data (design file) to check for deviations. As a result, the two models overlap each other and the specific deviations of the scanned object are visible in a color map as shown in Figure 7.5, in which one can observe precisely where and how much the variations occur. In general, most deviations are within ±0.2 mm (green region) and the biggest variations occur at the red and blue region. The large deviations in red are not true as the surface of the real manufactured prototype is smooth and flat and does not have such protruding roughness. This roughness is caused due to the X-ray artifacts. The blue parts indicate that the inclined surface of the manufactured prototype is 0.2 mm smaller than the nominal design. Note: “Top”, “Left”, “Right”, “Front” and “Back” marked in Figure 7.5 are used to define the surface orientation in the following graphs.

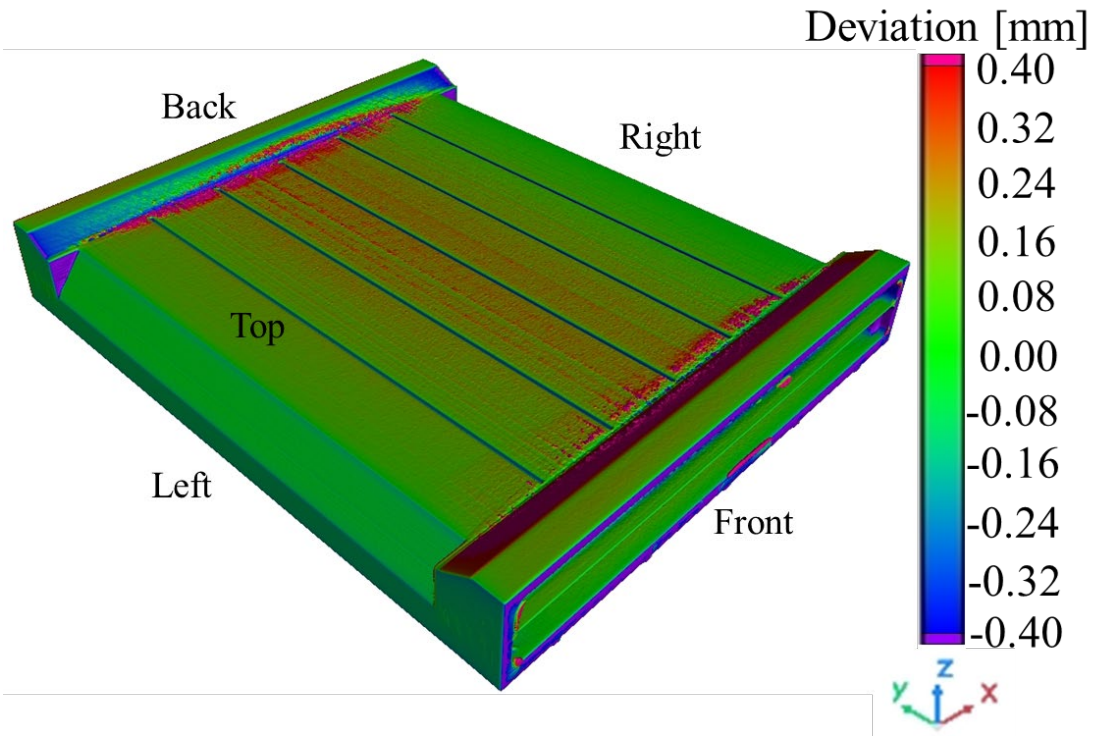

Figure 7. 5 An overview of deviations between scan data and CAD design as the color map.

7.2.2 Data analysis

The results of manufacturing-related tolerances from the comparison between the scanned data against the CAD model through the 3D inspection software VGSTUDIO MAX 2022.1 are presented in this section. The conformity check of the key parameters such as the microchannel structure was realized by measuring individual features also using the software VGSTUDIO MAX 2022.1. The deviation distribution of the manufactured HBS target prototype is plotted in Fig.7.6. The deviation is obtained by comparing CT data against the CAD file, i.e. CT data minus CAD value. Hence, if the symbol of deviation is negative, the manufactured target is smaller than the nominal design. Analogously, the manufactured product is larger than the CAD design if the symbol of deviation is positive. The surface in the vertical axis represents the surface area of the voxels from the CT scanning. As shown in the Figure 7.6, most deviations concentrate around ±0.2 mm (the green region) and only a few deviations in red and blue region are over 0.2 mm. Though the maximum of the absolute value of deviation is over 1 mm, which is an artifact. The specific reason will be discussed in the following context.

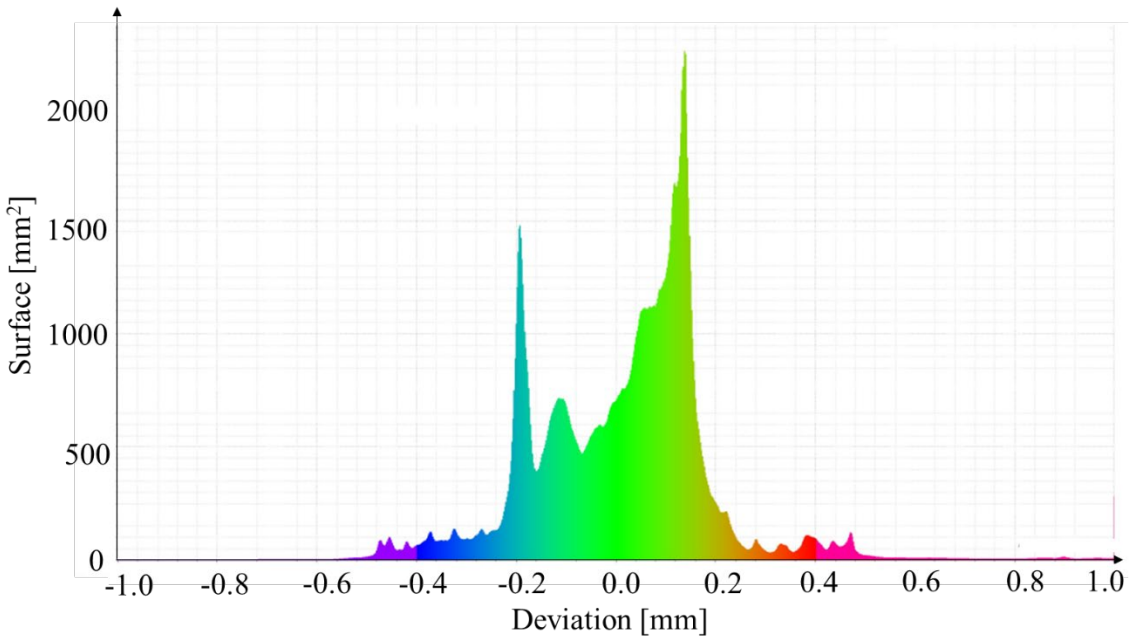

Figure 7. 6 Deviation distribution of the manufactured HBS target prototype.

In order to have a more intuitive concept, the normalized deviation distribution of the fabricated HBS target prototype is plotted in Figure 7.7, where the deviation in horizontal axis is an absolute

value. It can be directly seen from the accumulative deviation distribution that the curve can be divided into two parts. The beginning part is almost linear with a distinct positive increase until the deviation reaches 0.26 mm. The second part is much flatter than the first part. 90% of the deviations are smaller than 0.26 mm, 95% of the deviations are smaller than 0.38 mm and 98% of the deviations are smaller than 0.47 mm, which means only 2% of the deviations are in the interval of [0.47, 1]. Regarding the 2% with larger deviation, it could be errors occurring in the reconstructed model due to anisotropies in the voxels of the CT scanning.

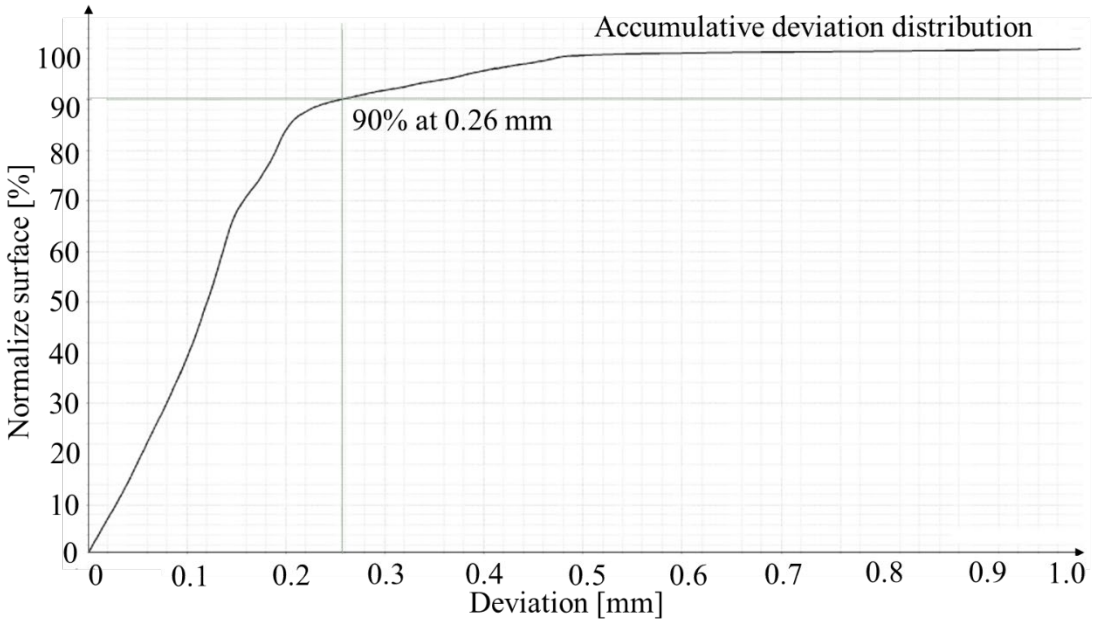

Figure 7. 7 Accumulative deviation distribution of the manufactured HBS target prototype.

The tolerance map clearly shows the position and the amount of the specific deviations. Figure 7.8 (a) and (b) presents the tolerance distribution on the top and bottom surface of the manufactured prototype. The orientations of top and bottom surface are taken from Figure 7.5. As shown in the map of Figure 7.8(a), most area on the top side is green, the deviations are within ±0.08 mm. But there exists partial red region in the inclined transition area "A" and on the same place at the other side, where the deviations are up to 0.4 mm. This large deviation is due to X-rays artifacts. The details of the artifact in the area "A" within the yellow circle can be seen in Figure 7.9. Compared with the top surface, there is no red area on the bottom side, all the deviations are within ±0.08 mm.

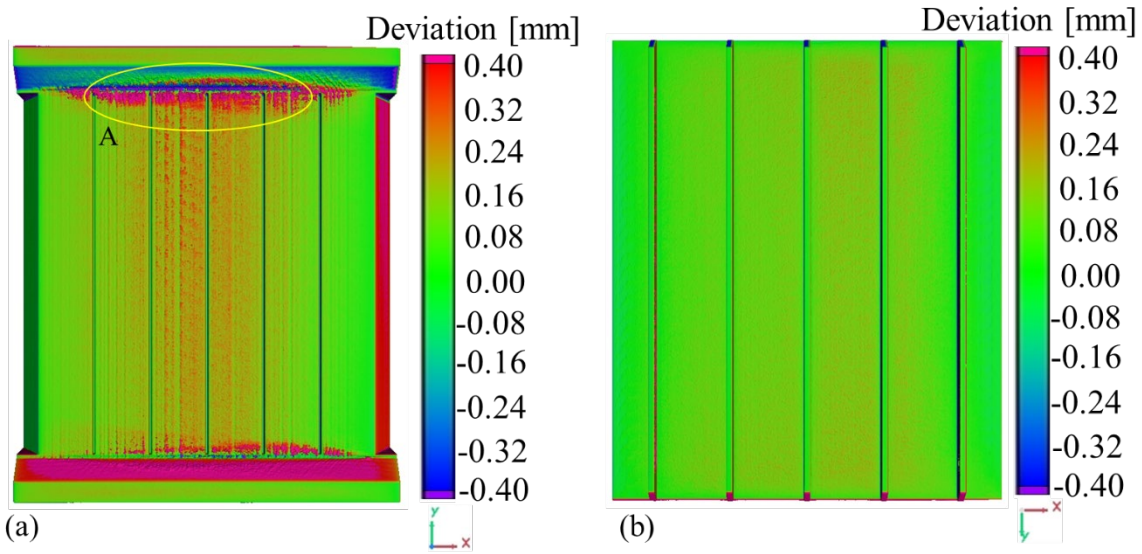

Figure 7. 8 The color map of deviations between scan data and CAD design of the HBS target (a) Top side (b) Bottom side.

Figure 7.9 shows a partial enlargement of the inclined transition zone "A" within the yellow circle in Figure 7.8 (a). It shows the surface is bumpy and there exist evident peaks in the red regions and valleys in the purple part, from which the deviations caused can be determined up to 0.4 mm. However, the surface of the real manufactured target is quite smooth and flat. Hence, the high roughness is artifacts, which is a common phenomenon called X-ray artifact influenced by many factors. The anisotropies in the measuring volume, geometrical errors from the manipulator, focus spot drift, and scaling errors of the 3D image lead to errors in voxel size and systematic length measurement. Especially the voxel size and the used surface determination algorithm also have an impact on roughness profile. While smaller voxel size results in large deviations for steep peaks or valleys.

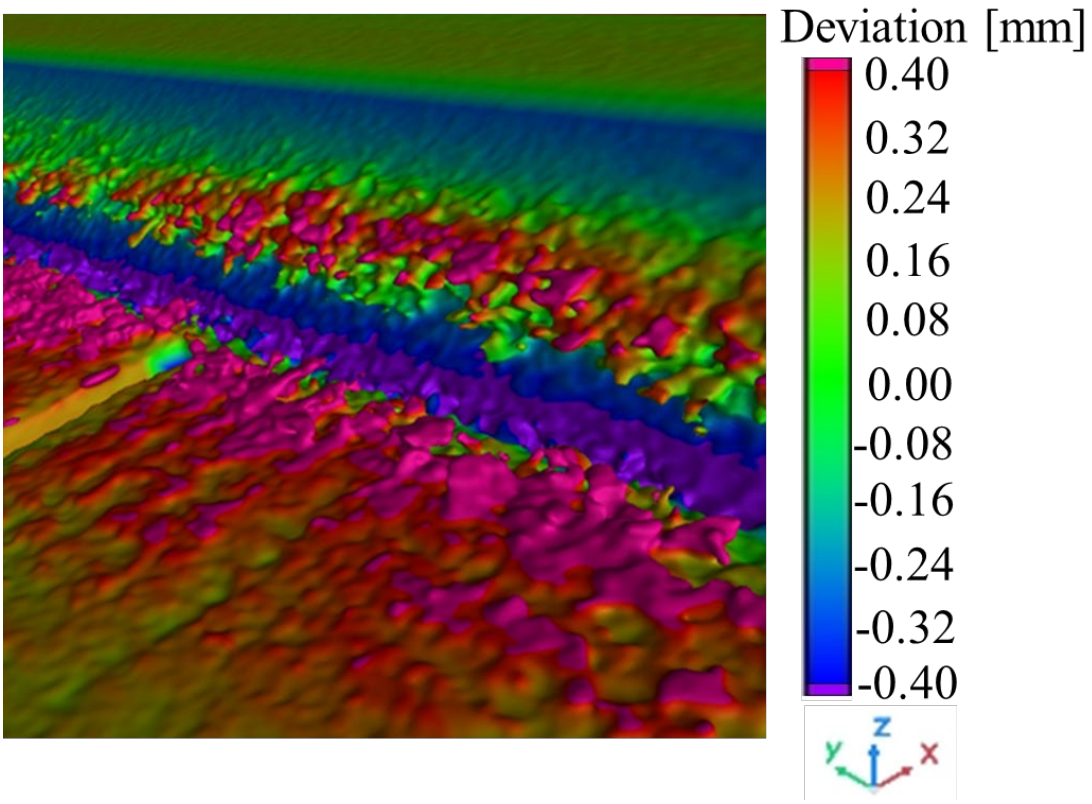

Figure 7. 9 A partial enlargement of the inclined transition zone “A” within the yellow circle in Figure 7.8 (a).

Figure 7.10 (a) and (b) presents the tolerance distribution on the left and right surface of the manufactured prototype. The orientations of left and right surface are taken from Figure 7.5. As shown in the map of 7.10(a), all tolerances in the left side are (green) within ±0.08 mm. But for the right side, all the area shown in Figure 7.10 (b) is red, corresponding to a deviation of 0.4 mm according to the color bar. This means the manufactured prototype's dimensional quality on the right side is 0.40 mm larger than the nominal value.

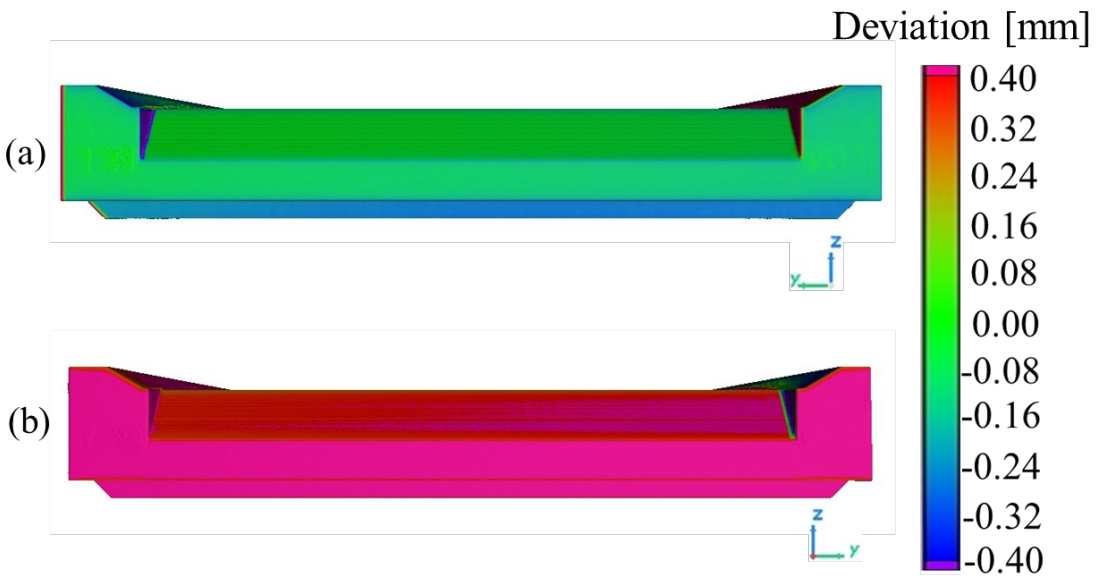

Figure 7. 10 The color map of deviations between scan data and CAD design of the HBS target (a) Left side (b) Right side.

Analogously, Figure 7.11 (a) and (b) presents the tolerance distribution on the front and back side of the manufactured prototype. The orientations of the front and back side are taken from Fig.7.5. As shown in the color map of 7.11(a), nearly all area on the front side are purple, which indicates that the relevant parameters of the manufactured prototype are at least 0.40 mm smaller than the CAD design. However, the areas of microchannel structures are green, which reveals the deviations of the channels are within ±0.1 mm. On the contrary, most areas of the back side are red and few on the left corner are light blue, which is out of the range of the color bar. The probable explanation is that the target is fixed on the rotation stage during the CT scan, and the back side is the contact surface to the turntable. Therefore, there exists an interface between the turntable and target. However, the detector cannot determine exactly which part is the turntable or which one is the back surface of the target, which results in large deviations and even the left corner is treated as the internal part of the target instead of a part of a surface. The bumps in Figure 7.11 (a) and (b) are caused by X-ray artifacts.

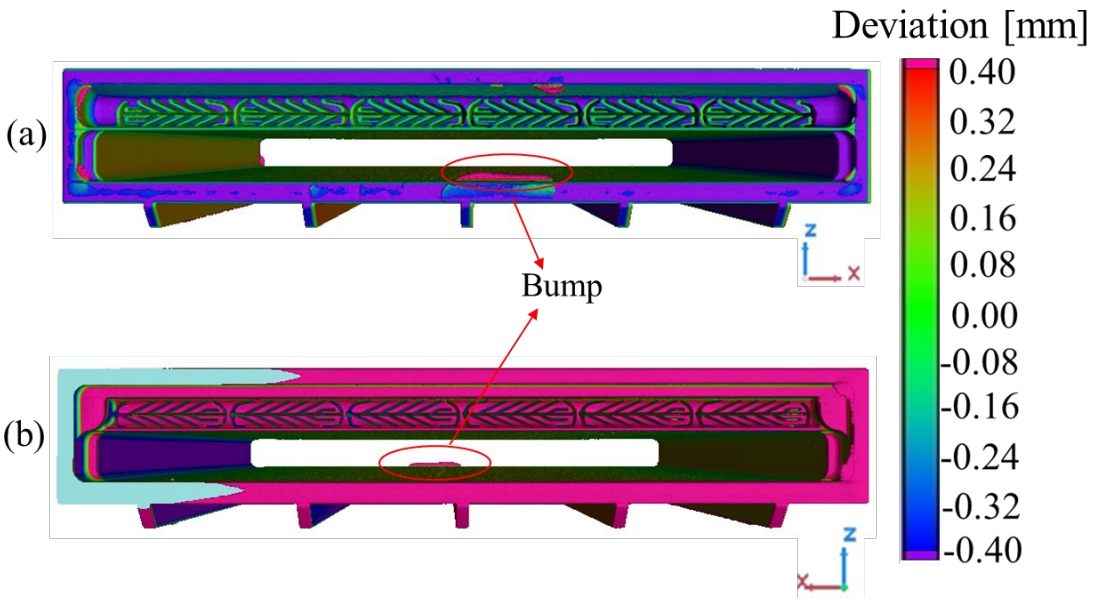

Figure 7. 11 The color map of deviations between scan data and CAD design of the HBS target (a) Front side (b) Back side.

As mentioned before the key design of the target is the microchannel structure, therefor this work also tried to estimate the manufacturing-related tolerances of the channels. Figure 7.12 shows the tolerance map of the microchannel structure of the target at the middle position, which is green and indicates the deviations of the channels are within ±0.1 mm.

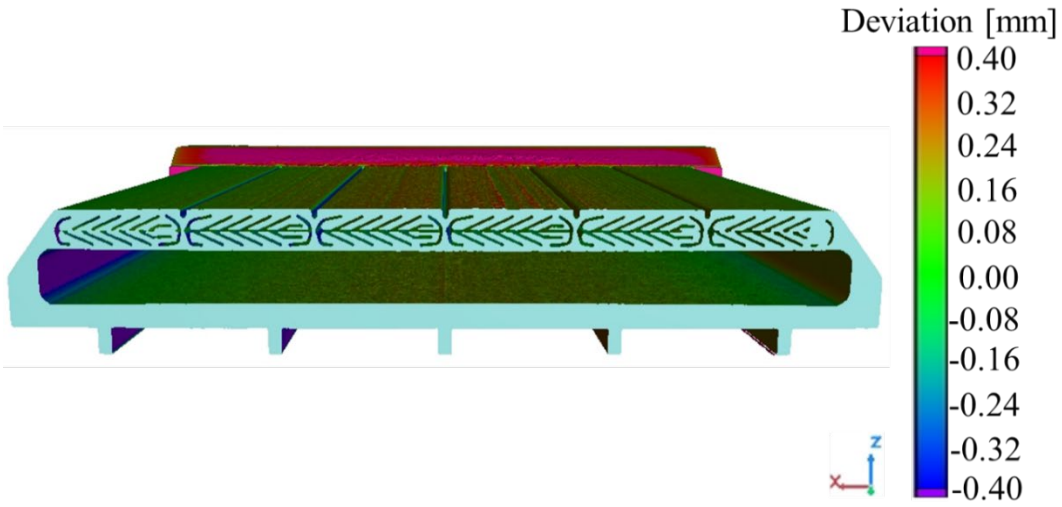

Figure 7. 12 The color map of deviations between scan data and CAD design in the middle cut-surface of the HBS target.

The evaluated manufacturing-related tolerances of key parameters are summarized in Table 7.2. The nominal parameters are from the CAD design of the target. The CT data are determined from the reconstructed 3D object with the software of VGSTUDIO MAX 2022.1. A minimum of 20 samples per parameter is taken to ensure a good statistical result and the measuring positions are distributed randomly. The CT data presented in the Table 7.2 are the mean value of the samples after removing the maximum and minimum values. The deviation is the difference of nominal value and CT data, i.e. the so-called manufacturing-related tolerance. Due to the anisotropies in the measuring volume of the scanner, errors occur on the reconstructed model. The specific geometrical definition of the individual parameter is presented in Figure 7.13. The standard deviation is calculated to evaluated the probability distribution. Most standard deviations are quite low except the target thickness, which indicates that most of the measured data tend to be close to the mean of the set, while the measured target thickness is spread out over a wider range compared with other parameters due to the roughness on the surface caused by X-ray artifacts.

Table 7. 2 Results of geometrical and dimensional tolerance analysis.

Parameters		Nominal value [mm]	CT data [mm]	Deviation[1] [mm]	Standard deviation [mm]
a	Target thickness	5.80	5.99	-0.19 ± 0.1	0.12
b	Channel width	0.35	0.42	-0.07 ± 0.1	0.01
c	Channel length (up)	2.08	2.08	0.00 ± 0.1	0.02
d	Channel length (down)	1.99	2.05	-0.06 ± 0.1	0.03
e	Top distance[2]	0.75	0.88	-0.13 ± 0.1	0.02
f	Bottom distance[3]	0.60	0.63	-0.03 ± 0.1	0.07

Note: 1 Deviation = Nominal value – CT data; 2 Top distance is the distance between the fins to the top surface; 3 Bottom distance is the distance between the fins to the bottom surface.

According to the Table 7.2, most of the deviations are quite small generally. The largest deviation is -0.19 mm, which occurs at target thickness, the symbol of minus "-" shows the manufactured target is larger than the nominal design. The other one is the tolerance of the distance between the fins to the top surface, which is -0.13 mm, the minus "-" also indicate the solid tantalum of fabricated object is more than the nominal value. The relevant influence on the target properties caused by the machining errors will be presented in Section 7.2.3.

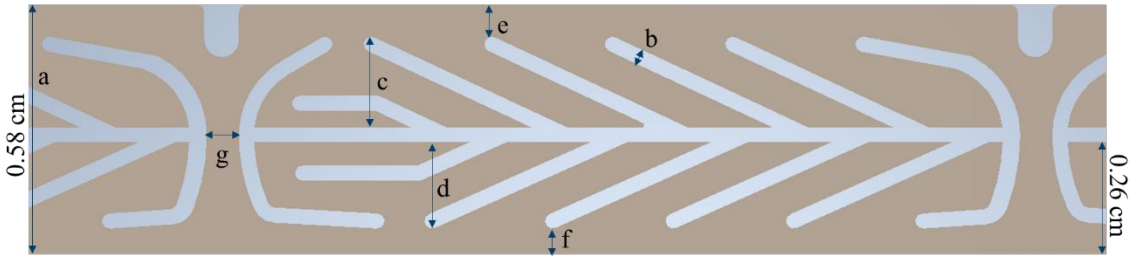

Figure 7. 13 Parameters for tolerance evaluation.

7.2.3 The effect of machining errors

The main factor which will have an impact on the target performance is the amount or mass of tantalum as the deviations of water channels are quite small. This work focuses on estimating the effect of processing errors in tantalum on the life time of the target. Of these quantities, hydrogen implantation and DPA are key factors in assessing target lifetimes.

Figure 7.14 shows the distribution of the percentage of stopping protons along the target depth, which is obtained via FLUKA simulations. In order to estimate the limitation of machining errors, the solid tantalum for neutron producing is extended to 1 cm thick but the microchannel structure stays the same as the nominal design. The protons impinge the target homogeneously from left to right side in the simulation. According to Figure 7.14, only 4.6% of protons accumulate in the solid tantalum part at the depth of 0.58 cm. However, the number of protons depositing in the target increases steeply to 98.7% in a subsequent 0.07 cm narrow interval once the target thickness exceeds 0.58 cm. The worst case is that all the protons stop in the target when the target is 0.65 cm thick (0.07 cm thicker than the nominal value of 0.58 cm). It can be also inferred from the steep interface in Figure 7.14 that the Bragg peak starts to appear immediately after the nominal target thickness of 0.58 cm. From this point of view, the manufactured target can't be thicker than the nominal value and the machining errors should be as small as possible.

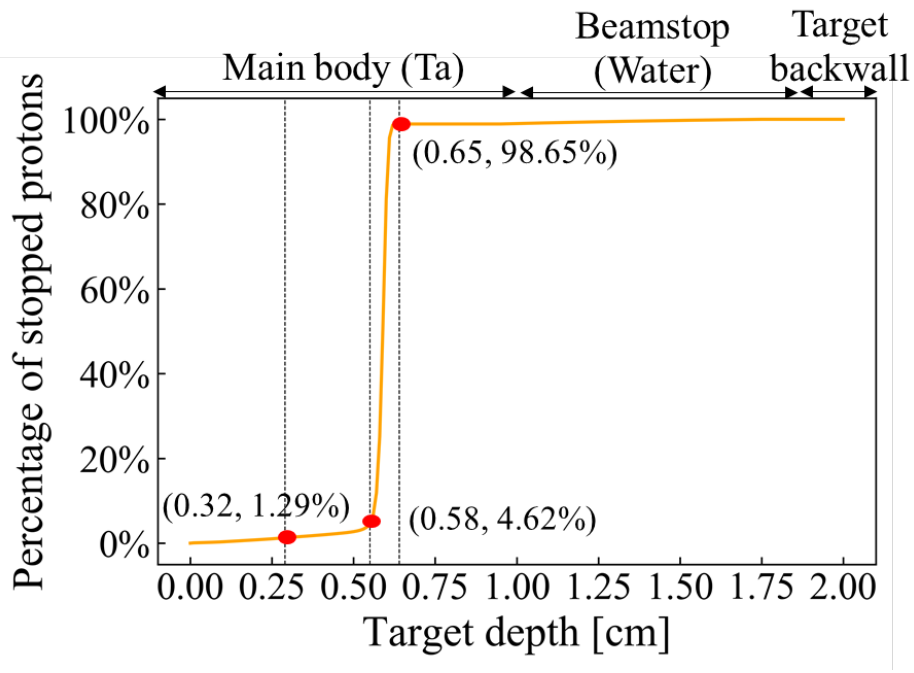

Figure 7. 14 The percentage of stopped protons along the target depth in a thick target.

The partial percentage of stopped protons in the steep interface of Figure 7.14 and the corresponding target thickness are listed in Table 7.4. The increment is 0.01 cm. According to Table 7.2, the machining error of target thickness is -0.02 cm (Deviation = Nominal value – CT data). In this case, the target is 0.6 cm thick and approximately 12% of protons will accumulate in the manufactured prototype. Compared to the nominal design, the number of protons parked on the target will increase by 157%.

Table 7. 3 Percentage of stopped protons in neutron-producing target for different thicknesses.

Target thickness [cm]	Percentage of stopping protons
0.58	4.6%
0.59	6.6%
0.60	11.9%
0.61	25.2%
0.62	51.5%
0.63	81.1%
0.64	95.7%
0.65	98.9%

According to [61, 62], the closest critical point at room temperature for tantalum is at a hydrogen atom concentration of 17%. Accumulation of such amount of hydrogen in tantalum at room temperature leads to the phase transition from the disordered solid solution of hydrogen in tantalum (α-phase) to the ordered tantalum hydride Ta_2H (β-phase) accompanied with re-arrangement of crystal lattice with possible loss of mechanical strength. The dissolved hydrogen also causes expansion of the crystal lattice [61], which can result in mechanical instability not only of the surface layer but of the whole target. At HBS facility, the proton current is 8.74×10^{15} s^{-1}. Based on Figure 7.14, at a depth of 0.32 cm and 0.58 cm, 1.29% and 4.62% of the protons were deposited in neutron-producing tantalum, respectively. Correspondingly, it can be inferred that 3.33% of protons accumulating in the last 0.26 cm of the target, i.e. the tantalum part after the horizontal water channel (see Figure 7.13), when the thickness of the neutron-producing tantalum is 0.58 cm. The estimations of the critical point of hydrogen are based on the percentage of protons in the last 0.26 cm for nominal target and 0.28 cm for fabricated prototype considering the machining-error of 0.02 cm. This is a very conservative evaluation as the percentage of stopped protons increase rapidly once the target thickness exceeds 0.58 cm (see Figure 7.14). Assuming all the protons accumulating in the tantalum can catch electrons to form hydrogen atoms. For a nominal design of 0.58 cm, it takes 18 years to reach the critical hydrogen concentration of 17%. However, the lifetime of a 0.6 cm thick target will be 6 years, which is decreased by 66.7% even if the manufacturing deviation is only 0.02 cm. The relevant data are summarized in Table 7.4.

Table 7. 4 Life time estimation of the nominal design and the fabricated prototype based on hydrogen concentration. Proton current is 8.74×10^{15} s^{-1} at HBS facility.

	Critical hydrogen concentration	Number of Ta atoms	Number of H atoms at critical point	Lifetime [years]
Nominal target	17%	1.0×10^{24}	1.7×10^{23}	18
Fabricated prototype	17%	1.1×10^{24}	1.9×10^{23}	6

The DPA in the tantalum target is mainly induced by protons and neutrons. Correspondingly, Figure 7.15 (a) and (b) depict the distribution of DPA induced by protons and neutrons in the fabricated prototype, respectively. In general, the DPA caused by protons is an order of magnitude

higher than the DPA caused by neutrons. Nonetheless, since the neutron-induced damage is more critical compared to the damage induced by protons, the minimum lifetime of the target is limited by the DPA induced by neutrons (see Table 5.6).

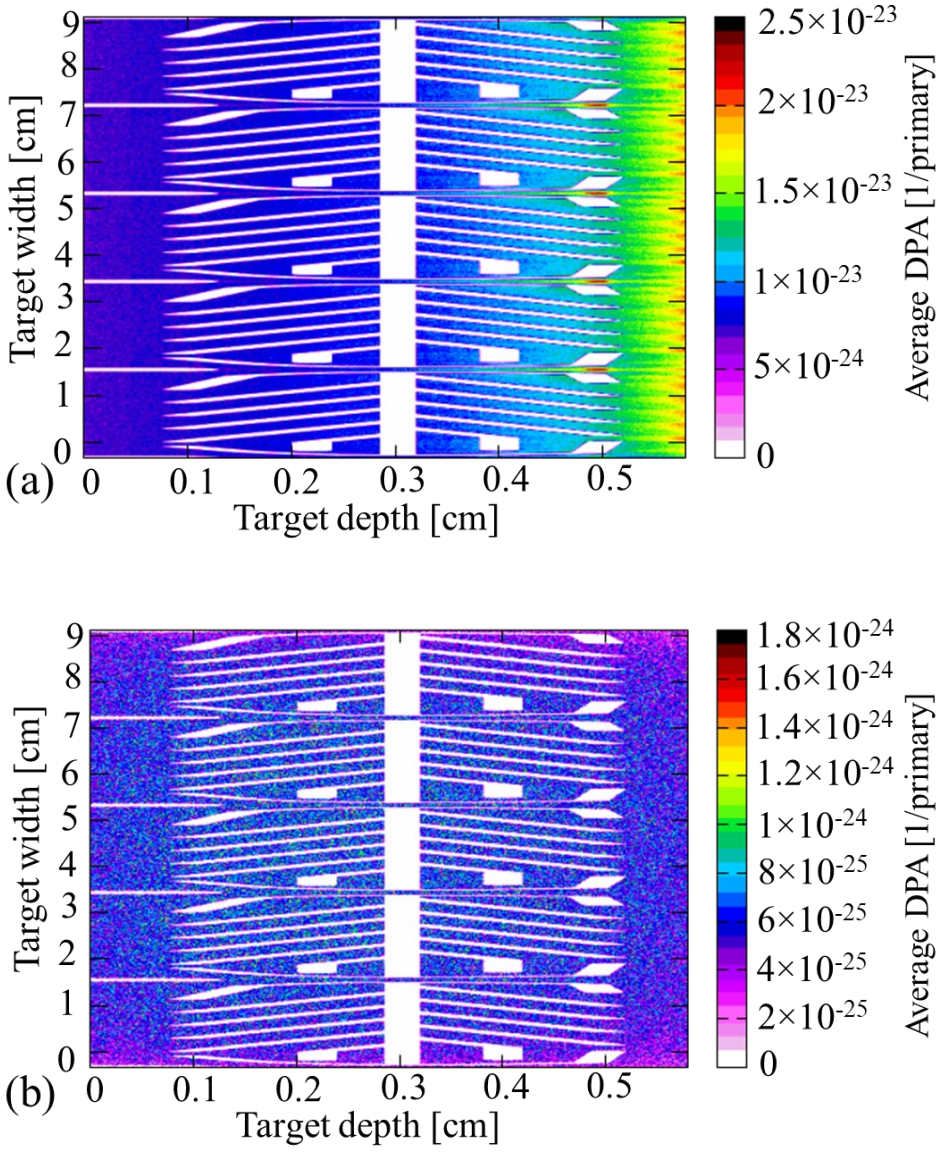

Figure 7. 15 (a) Spatial distribution of the proton atomic displacements of the fabricated prototype; (b) Spatial distribution of the neutron atomic displacements of the fabricated prototype.

A comparison of the lifetime estimation of the nominal target and fabricated prototype with the total integral values of DPA are listed in Table 7.5. Based on the total integrated value of the average DPA induced by protons and neutrons on the manufactured target, the predicted lifetimes

are 5.47 and 1.17 years, respectively, which are almost identical to the nominal design lifetimes but higher than the estimates of 2.62 and 0.78 years reported in [98]. The specific reasons for this can be found in Chapter 5.4.5. From this perspective, a machining error of 0.02 cm for the prototype is acceptable.

Table 7. 5 Lifetime estimation of the nominal target and fabricated prototype based on DPA.

		Annual does [DPA/fpy]		Minimum target lifetime [years]	
		Reference values	Calculated values	This work	Reference [98]
Nominal target	Proton-induced	11 [58],[99]	1.93 ± 0.1	5.70	2.62
	Neutron-induced	0.14 [100]	0.12 ± 0.1	1.17	0.78
Fabricated prototype	Proton-induced	11 [58],[99]	2.01 ± 0.1	5.47	
	Neutron-induced	0.14 [100]	0.12 ± 0.1	1.17	

Note: [DPA/fpy] is displacements per atom (DPA) per full power year.

As mentioned in [109], a problem with comparisons between CT data and CAD data is that it is not known whether the deviations are associated with inaccuracies in the manufacturing process or with the CT scan itself. Therefore, a calibration of the measurements using a high-resolution measuring microscope has been performed in this work.

7.3 Optical microscope test

Video measuring microscopes possess many merits, fast image processing, high-resolution, multi-touch panel PC with intuitive measuring software. Hence, this work adapted Garant MM1 200 video measuring microscope to make the comparison with regards to the parameters of the target prototype. Garant MM1 combines a 6.4-megapixel camera with an optical lens, enabling a field of view in different zoom level while offering a high precision. The length measurement error of this microscope is defined as $\mathrm{Error}\,[\mu m] = 2.9 + \mathrm{L}/100$ at 20 °C ±1 K, where L is the measured value in mm. Besides, measuring microscopes combine an optical microscope with a table capable of precise movement to measure targets. As with optical comparators, a telecentric optical system

is used to enable accurate measurements. All the measurements were performed in a non-contact manner, so there is no risk of damaging the target. Figure 7. 16 shows the Garant MM1 200 video measuring microscope used in the prototype measurement.

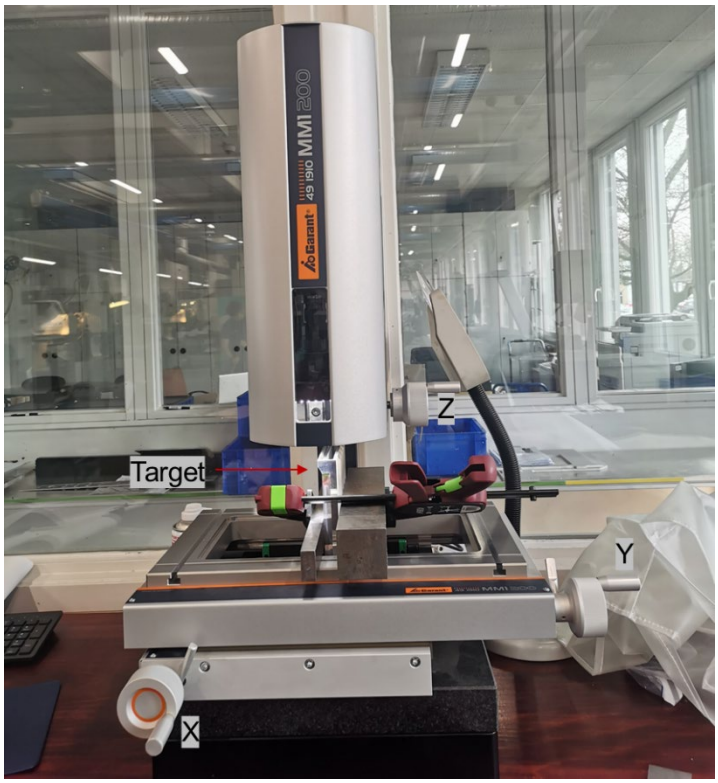

Figure 7. 16 Garant MM1 200 video measuring microscope at JCNS-2.

7.3.1 Experimental method

As presented in Figure 7.16, the target is fixed to the base. The measured surface is facing the direction of the LED light. First, a reference coordinate system needs to be established through slightly adjusting the handles (see Figure 7.16) in three axes (X, Y and Z). To move the handle slowly to find the right measuring surface. The image of the measured surface with high resolution is transmitted to the monitor connected with the microscope. Then the quantities can be measured with a high repeat accuracy through automatic focus and automatic edge detection. The relevant parameters of the manufactured prototype measured with Garant MM1 200 video-measuring microscope are shown in Figure 7.17.

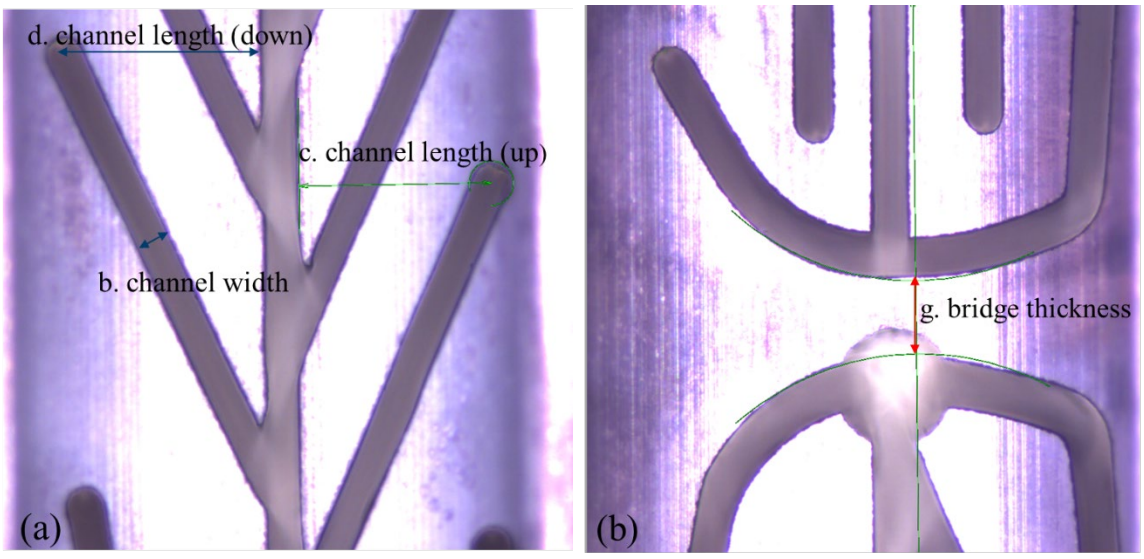

Figure 7. 17 The parameters of the fabricated prototype were measured with Garant MM1 200 video-measuring microscopes.

7.3.2 Data analysis

The evaluated machining errors of key parameters in measuring microscopes are summarized in Table 7.6. The nominal parameters are from the CAD design of the target. The measured data are obtained from the automatic focus measurement with Garant MM1 200 video-measuring microscope. A minimum of 20 samples per parameter is taken to ensure a good statistical result and the measuring positions are distributed randomly. The measured data presented in the Table 7.6 are the mean values of the samples. The deviation, i.e. the machining errors, is the difference of nominal value and measured data. The specific geometrical definition of the individual parameter is presented in Figure 7.13. The standard deviation is calculated to evaluate the probability distribution. All the standard deviations are quite low, which indicates that most of the measured data tend to be close to the mean of the dataset. Overall, the processing errors in Table 7.7 evaluated from the microscope measurement are smaller than the deviations assessed with the CT scan presented in Table 7.3. As this work already estimated the effect of the machining errors in tantalum on the life time of the target based on the deviations of the CT scan, the results indicate that the influences are negligible. The effect of the processing deviations evaluated from the optical microscope in the performance of tantalum target will not be repeated.

Table 7. 6 Machining errors of key parameters measured with measuring microscopes.

	Parameters	Nominal value [mm]	Measured data [mm]	Deviation[1] [mm]	Standard deviation [mm]
b	Channel width	0.35	0.36	-0.01 ± 0.003	0.03
c	Channel length (up)	2.08	2.05	0.03 ± 0.003	0.03
d	Channel length (down)	1.99	1.99	0.00 ± 0.003	0.02
g	Bridge thickness	0.75	0.71	0.04 ± 0.003	0.02

Note: 1 Deviation = Nominal value – Measured data. 2 Measurement error is calculated with $Error\ [\mu m] = 2.9 + L/100$ at 20 °C ±1 K, where L is the measured value in mm.

7.4 Conclusions

Considering the accuracy of measurement methods, the results of microscope should be more precise compared with the data of CT scan. Besides, X-ray artifacts in CT scan also lead to a larger deviation compared to the data of Garant MM1 200 video-measuring microscopes. Correspondingly, it can be inferred that the machining errors should be smaller than the results presented in Table 7.3, which were obtained from CT scan. However, the effect of the machining errors of 0.02 cm in tantalum on the lifetime of the target are quite small according to the estimations of hydrogen implantation and DPA even if taking the deviations of CT scan as the real processing errors. In general, the microchannel target is manufacturable and the machining error of the prototype is acceptable from the point of particle transport view. In addition, the effect of machining errors on the cooling efficiency and thermomechanical properties of the target should be further estimated.

8 Conclusion and Outlook

8.1 Conclusion

The High Brilliance neutron Source (HBS) project aims to develop a high-current accelerator-driven neutron source (Hi-CANS) to deliver high brilliant beam to a variety of neutron scattering instruments. The high brilliance is going to be ensured by an optimal target-moderator-reflector (TMR) unit. Within the framework of the project, the heart of the TMR unit – the neutron-producing target is well-dedicated through a long iterative optimization via FLUKA and ANSYS simulations, which results in an optimal tantalum target with an innovative internal microchannel water-cooling structure for the required HBS specifications of a 70 MeV pulsed proton beam with a peak current of 100 mA and an average power release of 100 kW with a duty cycle of 1.43 %. The first solid tantalum target [54] with a microchannel structure, as a result of optimization between reduced thermal and mechanical loads, was fabricated and tested with the high heat flux experiment with an electron beam. Besides, in order to further get an optimal design in terms of both particle transport and thermomechanical properties, the microchannel geometry of the target was gradually adapted using the particle transport code FLUKA and thermo-mechanical simulations with ANSYS. The development of the concept of an optimized microchannel target for HBS is described in this thesis. Typical potential risks that compromise the integrity of the high-power density proton target, including hydrogen embrittlement and blistering, heat dissipation, thermomechanical stress, and critical heat flux, have been minimized accordingly during the development process. In addition, the optimized microchannel target was manufactured via electrical discharge machining (EDM) successfully and examined the machining-error through computed tomography (CT) and optical microscopy measurement respectively.

The accelerated proton collides with the nucleus of the tantalum target, being scattered or releasing high-energy neutrons. The more neutrons produced in the target collision, the “brighter” the neutron source. The first solid tantalum target with a microchannel structure, which resulted from optimization between reduced thermal and mechanical loads, was fabricated by wire erosion and tested with high heat fluxes using electron beams in the JUDITH-II facility at IEK-4 of

Forschungszentrum Jülich. This is a very conservative experiment since nearly all the heat from electron beams concentrate on the target surface and only approximate 1/3 of the microchannel surfaces (the tantalum-water interfaces) contributes to the cooling. However, the target is not damaged even though the power density putting on the target surface is up to 1 kW/cm² which is the HBS design goal. The experimental results prove that the internal microchannel water-cooling concept can efficiently remove the heat load of 1 kW/cm² and the HBS design goal is achieved. Besides, for the actual operation at HBS facility under a pulsed proton beam, the heat deposition in the target is distributed over the entire target volume. Accordingly, all cross-sections of the microchannel structure are involved in the cooling. From this point of view, the maximum operational power density of the target can reach 3 kW/cm^2.

In addition, an optimized target with microchannel structure was obtained from an iteration between particle transport code FLUKA and thermomechanical simulations with ANSYS. From the particle transport point of view, the optimized internal cooling microchannel structure matches the proton beam of 70 MeV energy and the target thickness is slightly smaller than the ion penetration depth. Correspondingly, in this optimized design 93.22% of protons are dumped into the water beamstop, 2.22% reaches the tantalum backwall behind the beamstop, and only 4.56% of protons accumulate in the neutron-producing target, which strongly minimizes the risk of hydrogen damage. Besides, a homogeneous heat deposition within the target was achieved minimizing strains and stresses. The microchannel cooling structures provide plenty of cross-sectional area to dissipate heat, which can efficiently decrease thermal stresses caused by temperature gradients. Based on the number of displacements per atom induced by protons and neutrons, the target is expected to have a minimum lifetime of 1.17 years.

What's more, the mechanical and thermo-mechanical properties of the optimized target are also well-adjusted for the HBS specifications through ANSYS simulations under two flow patterns. For the steady state, the maximum interfacial temperature is approximately 115 °C, well below the boiling temperature at 3 bar pressure. The maximum interfacial heat flux of 3.6×10^6 W/m^2 is three times lower than the highest heat flux of 1.1×10^7 W/m^2 achieved on the first target in the last JUDITH experiment, which means that the safety margin for the burn-out of the optimized target is quite high. Furthermore, simulations with an elastic ideal plastic material model show that if the yield stress is 185 MPa, the expected plastic deformation caused by local stresses is small, well

below 1%. Besides, even without considering the hardening of the material, the safety factor for plastic collapse due to mechanical loading is considerable (factor 8.9), but it should be considered that the elongation at the break of the material is achieved at a much lower load factor of approximately 2.8. For unsteady flow, the pulsed operation will significantly increase the maximum temperature of the target compared to the time-averaged thermal deposition under steady-state conditions. The maximum interfacial temperature in the microchannel is approximately 144 °C. Boiling is expected to occur at the beamstop interface, so the interface should be oriented upwards to allow vapor bubbles to separate from the surface. In addition, the maximum interfacial heat flux at the channel wall of 5.5×10^6 W/m^2 is quite high, but still below the predicted critical heat flux of 3×10^7 W/m^2.

Finally, a prototype of the optimized target was fabricated via electrical discharge machining successfully and examined the manufacturing-related errors through CT measurement. The maximum machining error of 0.2 mm occurred in the target thickness. Accordingly, the effects of the machining error of 0.2 mm on the particle transport properties of the optimized target are estimated with FLUKA simulations. It has been shown that the proportion of protons accumulated in the neutron-producing target will increase to 12%, but the effect on the life expectancy of the optimized target based on DPA damage will be negligible. However, the actual processing errors could be smaller than those measured by CT, as artifacts and resolution limitations can amplify errors. Thus, the optimized microchannel target is manufacturable and the machining errors are acceptable.

In summary, this thesis provides an optimal neutron-producing target design for HBS specifications in terms of particle transport and mechanical properties through the iterative optimization, which will be of benefit in the development of compact accelerator-based neutron sources.

8.2 Outlook

Neutrons can activate materials, especially high-Z materials like tantalum; protons can also activate measurement equipment. Since the activated parts of the target can cause significant dose

to maintenance personnel, handling of “hot” materials has to be considered carefully. The target material activation after operation is therefore necessary to be simulated with FLUKA.

Nevertheless, the thermal limit is an essential factor for the target to be able to operate thermally and mechanically stable. Hence, a high heat flux test should be performed for the optimized target to determine the critical heat flux at the metal-water boundary and also the maximum power which the target can withstand.

Besides, the current selected target material is pure solid tantalum. From the holistic view, tantalum performs well in many aspects. For example, it has a high melting point, good mechanical properties, high hydrogen solubility, and high neutron yield etc. However, due to some limits with respect to mechanical properties of tantalum, especially for thermomechanical behavior, it is worth to investigate Ta-W alloy as a potential material for the target.

For the pulse operation, so far only CFX simulations have been carried out to obtain an impression of the expected temperatures on the optimized target. The real target of the HBS facility will be operated under a pulsed proton beam, therefore a possible pressure pulse and the thermomechanical properties of the optimized target should also be investigated by ANSYS simulations to determine the upper limit of plastic deformation due to local stress and the limit of mechanical loading to prevent plastic collapse.

Besides, fatigue of the optimized target is also a topic that has to be investigated in detail. ANSYS simulations should be performed with considering radiation-related changes in material properties. It is worth comparing the calculated stresses and stress cycles with the permissible values, which can be obtained from the literature or determined experimentally.

Bibliography

[1] E. Mauerhofer et al., 'Prompt gamma rays from fast neutron inelastic scattering on aluminum, titanium and copper', J Radioanal Nucl Chem, Aug. 2022, doi: 10.1007/s10967-022-08435-6.

[2] N. Nandakumaran et al., 'Unravelling Magnetic Nanochain Formation in Dispersion for In Vivo Applications', Advanced Materials, vol. 33, no. 24, Jun. 2021, doi: 10.1002/adma.202008683.

[3] T. Köhler et al., 'Mechanism of magnetization reduction in iron oxide nanoparticles', Nanoscale, vol. 13, no. 14, pp. 6965–6976, Apr. 2021, doi: 10.1039/d0nr08615k.

[4] S. Bouat *et al.*, 'Detection of hydrate plugs inside submarine pipelines using neutrons', *Nondestructive Testing and Evaluation*, vol. 37, pp. 1–13, Oct. 2021, doi: 10.1080/10589759.2021.1990284.

[5] W. Ji, Z. Huang, E. Kentzinger, U. Rücker, T. Brückel, and Y. Xiao, 'Nanoparticle-induced morphological transformation in block copolymer-based nanocomposites', *Nanoscale*, vol. 14, no. 24, pp. 8766–8775, May 2022, doi: 10.1039/d2nr01625g.

[6] W. Jin *et al.*, 'Bulk domain Meissner state in the ferromagnetic superconductor EuFe2(As0.8 P0.2)2: Consequence of compromise between ferromagnetism and superconductivity', *Phys Rev B*, vol. 105, no. 18, May 2022, doi: 10.1103/Phys Rev B.105.L180504.

[7] N. Biniskos *et al.*, 'Complex magnetic structure and spin waves of the noncollinear antiferromagnet Mn5Si3', *Phys Rev B*, vol. 105, no. 10, Mar. 2022, doi: 10.1103/PhysRevB.105.104404.

[8] L.-M. Wang, O. Petracic, J. Schubert, and Th. Brückel, 'Electric-field control of magnetism in iron oxide nanoparticle/BaTiO $_3$ film composites', *Materials Express*, vol. 12, no. 4, pp. 599–602, Apr. 2022, doi: 10.1166/mex.2022.2187.

[9] H. Gerstenberg and I. Neuhaus, 'A brief overview of the research reactor FRM II', *International Journal of Nuclear Energy Science and Technology*, vol. 4, no. 4, pp. 265–274, Jan. 2009, doi: 10.1504/IJNEST.2009.028587.

[10] R. Pynn, 'Neutron scattering instrumentation at reactor-based installations', *Review of Scientific Instruments*, vol. 55, no. 6, pp. 837–848, Jun. 1984, doi: 10.1063/1.1137855.

[11] Th. A. Mueller et al., 'Improved predictions of reactor antineutrino spectra', Phys Rev C, vol. 83, no. 5, p. 054615, May 2011, doi: 10.1103/PhysRevC.83.054615.

[12] National Research Council (U.S.). Panel on Neutron Scattering. and G. Rossi, *Neutron scattering facilities in europe : present status and future perspectives*. University of Milan, 2016.

[13] H. Conrad, 'Spallation: Neutrons Beyond Nuclear Fission', in *Handbook of Particle Detection and Imaging*, M. and G. C. and B. I. Fleck Ivor and Titov, Ed. Cham: Springer International Publishing, 2021, pp. 1001–1040. doi: 10.1007/978-3-319-93785-4_30.

[14] R. Hall-Wilton and C. Theroine, 'Status of the European Spallation Source ESS AB, the Instrument Selection Process, and a Fundamental Physics Beamline at the ESS', *Phys Procedia*, vol. 51, pp. 8–12, 2014, doi: https://doi.org/10.1016/j.phpro.2013.12.004.

[15] European Spallation Source Conceptual Design Report (CDR, 2012). https://europeanspallationsource.se/sites/default/files/downloads/2017/09/CDR_final_120206.pdf.

[16] European Spallation Source Technical Design Report (2015). https://backend.orbit.dtu.dk/ws/portalfiles/portal/110641459/TDR_final.pdf

[17] T. Brückel *et al.*, 'Low energy accelerator-driven neutron sources: Closing the gap and shaping the future', *Neutron News*, vol. 31, no. 2–4. Bellwether Publishing, Ltd., pp. 2–3, 2020. doi: 10.1080/10448632.2020.1826231.

[18] I. S. Anderson *et al.*, 'Research opportunities with compact accelerator-driven neutron sources', *Phys Rep*, vol. 654, pp. 1–58, 2016, doi: https://doi.org/10.1016/j.physrep.2016.07.007.

[19] Letourneau Alain *et al.*, 'Development of compact accelerator neutron source', *EPJ Web Conf.*, vol. 146, p. 3018, 2017, doi: 10.1051/epjconf/201714603018.

[20] T. Brückel, T. Gutberlet, S. Schmidt, C. Alba-Simionesco, F. Ott, and A. Menelle, 'Low energy accelerator-driven neutron facilities—A prospect for a brighter future for research with neutrons', *Neutron News*, vol. 31, no. 2–4, pp. 13–18, 2020, doi: 10.1080/10448632.2020.1819125.

[21] U. Rücker *et al.*, 'The Jülich high-brilliance neutron source project', *The European Physical Journal Plus*, vol. 131, no. 1, p. 19, 2016, doi: 10.1140/epjp/i2016-16019-5.

[22] T. Gutberlet *et al.*, 'Sustainable neutrons for today and tomorrow—The Jülich High Brilliance neutron Source project', *Neutron News*, vol. 31, no. 2–4, pp. 37–43, 2020, doi: 10.1080/10448632.2020.1819132.

[23] M. Rimmler *et al.*, 'Proton Beam Multiplexer Developments for Multi-Target Operation at the High-Brilliance Neutron Source HBS', *EPJ Web Conf*, vol. 231, p. 02002, 2020, doi: 10.1051/epjconf/202023102002.

[24] J. Carpenter and C.-K. Loong, 'Elements of Slow-Neutron Scattering: Basics, Techniques, and Applications', 2015.

[25] P. D. L. Fernandez-Alonso, *Neutron Scattering*. Academic Press., 2013.

[26] F. Foglia *et al.*, 'Progress in neutron techniques: Towards improved polymer electrolyte membranes for energy devices', *Journal of Physics Condensed Matter*, vol. 33, no. 26, Jun. 2021, doi: 10.1088/1361-648X/abfc10.

[27] T. Brückel et al, Technical design report of the High Brilliance neutron Source HBS, which will be published in 2023.

[28] S. Terrón *et al.*, 'Conceptual design of the beryllium rotating target for the ESS-Bilbao facility', *Nucl Instrum Methods Phys Res A*, vol. 724, pp. 34–40, 2013, doi: https://doi.org/10.1016/j.nima.2013.04.072.

[29] J. Schwindling *et al.*, 'Long term operation of a 30 kW Beryllium target at IPHI', *Journal of Neutron Research*, vol. 24, no. 3–4, pp. 289–298, Oct. 2022, doi: 10.3233/jnr-220024.

[30] B. Bayanov, V. Belov, V. Kindyuk, E. Oparin, and S. Taskaev, 'Lithium neutron producing target for BINP accelerator-based neutron source', in *Applied Radiation and Isotopes*, 2004, vol. 61, no. 5. doi: 10.1016/j.apradiso.2004.05.032.

[31] D. Petrich *et al.*, 'A neutron production target for FRANZ', *Nucl Instrum Methods Phys Res A*, vol. 596, no. 3, pp. 269–275, Nov. 2008, doi: 10.1016/j.nima.2008.08.131.

[32] R. Bedogni *et al.*, 'Neutron spectrometry of a liquid Lithium based (p, n) beam at SARAF facility using the broad-energy range directional spectrometer CYSP', *Nucl Instrum Methods Phys Res A*, vol. 902, 2018, doi: 10.1016/j.nima.2018.06.053.

[33] M. Paul *et al.*, 'Reactions along the astrophysical s-process path and prospects for neutron radiotherapy with the Liquid-Lithium Target (LiLiT) at the Soreq Applied Research Accelerator Facility (SARAF)', *European Physical Journal A*, vol. 55, no. 3. 2019. doi: 10.1140/epja/i2019-12723-5.

[34] M. Friedman *et al.*, 'Simulation of the neutron spectrum from the ^{7}Li(p,n) reaction with a liquid-lithium target at Soreq Applied Research Accelerator Facility', *Nucl Instrum Methods Phys Res A*, vol. 698, 2013, doi: 10.1016/j.nima.2012.09.027.

[35] L. Silvestrin, D. Bisello, J. Esposito, P. Mastinu, G. Prete, and J. Wyss, 'SPES and the neutron facilities at laboratori nazionali di legnaro', *Eur Phys J Plus*, vol. 131, no. 3, 2016, doi: 10.1140/epjp/i2016-16072-0.

[36] P. Zakalek, P.-E. Doege, J. Baggemann, E. Mauerhofer, and T. Brückel, 'Energy and target material dependence of the neutron yield induced by proton and deuteron bombardment', *EPJ Web Conf*, vol. 231, p. 03006, 2020, doi: 10.1051/epjconf/202023103006.

[37] P. Capel, 'Introduction to nuclear-reaction theory', *Springer Proceedings in Physics*, vol. 225. 2019. doi: 10.1007/978-3-030-22204-8_2.

[38] H. Feshbach, 'A unified theory of nuclear reactions. II', *Ann Phys (N Y)*, vol. 19, no. 2, 1962, doi: 10.1016/0003-4916(62)90221-X.

[39] P. G. Hansen and J. A. Tostevin, 'Direct Reactions with Exotic Nuclei', *Annual Review of Nuclear and Particle Science*, vol. 53, 2003, doi: 10.1146/annurev.nucl.53.041002.110406.

[40] Y. Alhassid, G. F. Bertsch, P. Fanto, and T. Kawano, 'Transmission coefficients in compound-nucleus reaction theory', *Phys Rev C*, vol. 99, no. 2, 2019, doi: 10.1103/PhysRevC.99.024621.

[41] A. Ferrari, P. R. Sala, A. Fasso, and J. Ranft, 'FLUKA: A multi-particle transport code (Program version 2005)', Sep. 2005, doi: 10.2172/877507.

[42] T. T. Böhlen *et al.*, 'The FLUKA Code: Developments and Challenges for High Energy and Medical Applications', *Nuclear Data Sheets*, vol. 120, pp. 211–214, 2014, doi: https://doi.org/10.1016/j.nds.2014.07.049.

[43] G. Battistoni *et al.*, 'The FLUKA code: Description and benchmarking', in *AIP Conference Proceedings*, 2007, vol. 896. doi: 10.1063/1.2720455.

[44] C. Ahdida *et al.*, 'New Capabilities of the FLUKA Multi-Purpose Code', *Front Phys*, vol. 9, 2022, doi: 10.3389/fphy.2021.788253.

[45] D. Y. Lee and K. Vafai, 'Comparative analysis of jet impingement and microchannel cooling for high heat flux applications', *Int J Heat Mass Transf*, vol. 42, no. 9, 1999, doi: 10.1016/S0017-9310(98)00265-8.

[46] J. J. Lewandowski and M. Seifi, 'Metal Additive Manufacturing: A Review of Mechanical Properties', *Annual Review of Materials Research*, vol. 46. 2016. doi: 10.1146/annurev-matsci-070115-032024.

[47] D. A. Brown *et al.*, 'ENDF/B-VIII.0: The 8th Major Release of the Nuclear Reaction Data Library with CIELO-project Cross Sections, New Standards and Thermal Scattering Data', *Nuclear Data Sheets*, vol. 148, pp. 1–142, Feb. 2018, doi: 10.1016/j.nds.2018.02.001.

[48] S. Kunieda *et al.*, 'Overview of JENDL-40/HE and benchmark calculations', Japan, 2016. [Online]. Available: http://inis.iaea.org/search/search.aspx?orig_q=RN:48045186

[49] Britannica, The Editors of Encyclopaedia. "cross section". Encyclopedia Britannica, 5 Feb. 2018, https://www.britannica.com/science/cross-section-physics. Accessed 28 April 2023.

[50] Y. Nakasone, S. Yoshimoto, and T. A. Stolarski, *Engineering Analysis with ANSYS Software*. 2007. doi: 10.1016/B978-0-7506-6875-0.X5030-3.

[51] A. D. Moscheto, C. Cziulik, S. Marcon, and M. Sulevis, "Space claim analysis for addressing maintenance of key components in complex products," Assembly Automation, vol. 37, no. 1, 2017, doi: 10.1108/AA-04-2016-038.

[52] E. H. Dill, 'ANSYS Workbench', in *The Finite Element Method for Mechanics of Solids with ANSYS Applications*, 2020. doi: 10.1201/b11455-19.

[53] W. Wagner *et al.*, 'The IAPWS industrial formulation 1997 for the thermodynamic properties of water and steam', *J Eng Gas Turbine Power*, vol. 122, no. 1, 2000, doi: 10.1115/1.483186.

[54] T. Brückel et al, Conceptual Design Report of the High Brilliance Neutron Source (HBS), 2020, https://juser.fz-juelich.de/record/884799/files/Allgemeines_08.pdf

[55] Q. Ding et al., 'An optimized microchannel Ta target for high-current accelerator-driven neutron sources', Nucl Instrum Methods Phys Res A, p. 167508, Oct. 2022, doi: https://doi.org/10.1016/j.nima.2022.167508.

[56] M. R. Louthan, G. R. Caskey, J. A. Donovan, and D. E. Rawl, 'Hydrogen embrittlement of metals', *Materials Science and Engineering*, vol. 10, pp. 357–368, 1972, doi: https://doi.org/10.1016/0025-5416(72)90109-7.

[57] YU. v. Martynenko, 'The theory of blister formation', *Radiat Eff*, vol. 45, no. 1–2, pp. 93–101, Jan. 1979, doi: https://doi.org/10.1080/00337577908208414.

[58] N. Simos *et al.*, 'Multi-MW accelerator target material properties under proton irradiation at Brookhaven National Laboratory linear isotope producer', *Physical Review Accelerators and Beams*, vol. 21, no. 5, May 2018, doi: 10.1103/PhysRevAccelBeams.21.053001

[59] A. San-Martin and F. D. Manchester, 'The H-Ta (hydrogen-tantalum) system', *Journal of Phase Equilibria*, vol. 12, no. 3, pp. 332–343, 1991, doi: 10.1007/BF02649922.

[60] X. S. Kong *et al.*, 'First-principles calculations of hydrogen solution and diffusion in tungsten: Temperature and defect-trapping effects', *Acta Mater*, vol. 84, pp. 426–435, Feb. 2015, doi: 10.1016/j.actamat.2014.10.039.

[61] V. T. Astrelin et al., 'Blistering of the selected materials irradiated by intense 200 keV proton beam', Journal of Nuclear Materials, vol. 396, no. 1, pp. 43–48, Jan. 2010, doi: 10.1016/j.jnucmat.2009.10.051.

[62] T. Schober, 'Vanadium-, niobium- and tantalum-hydrogen', Solid State Phenomena, vol. 49–50, pp. 357–422, 1996, doi: 10.4028/www.scientific.net/ssp.49-50.357.

[63] J. Chen et al., 'Summary of the results from post-irradiation examination of spent targets at the FZ-Juelich', in Journal of Nuclear Materials, May 2003, vol. 318, no. SUPPL, pp. 56–69. doi: 10.1016/S0022-3115(03)00007-2.

[64] A. J. Koning, S. Hilaire, and M. C. Duijvestijn, 'TALYS: Comprehensive nuclear reaction modeling', in *AIP Conference Proceedings*, 2005, vol. 769. doi: 10.1063/1.1945212.

[65] J. F. Ziegler, M. D. Ziegler, and J. P. Biersack, 'SRIM - The stopping and range of ions in matter (2010)', *Nucl Instrum Methods Phys Res B*, vol. 268, no. 11–12, 2010, doi: 10.1016/j.nimb.2010.02.091.

[66] P. Mastinu *et al.*, 'Micro-channel-based high specific power lithium target', *Nuovo Cimento della Societa Italiana di Fisica C*, vol. 38, no. 6, Nov. 2015, doi: 10.1393/ncc/i2015-15193-y.

[67] S. G. Kandlikar, 'Heat transfer mechanisms during flow boiling in microchannels', *J Heat Transfer*, vol. 126, no. 1, pp. 8–16, Feb. 2004, doi: 10.1115/1.1643090.

[68] G. Cerbe and H.J. Homann. Einführung in die Wärmelehre: von der Thermodynamik zur technischen Anwendung. Studienbücher der technischen Wissenschaften. Hanser, 1990.

[69] VDI Gesellschaft. VDI Heat Atlas. VDI-Buch. Springer Berlin Heidelberg, 2010.

[70] S. Kandlikar, S. Garimella, D. Li, S. Colin, and M.R. King. Heat Transfer and Fluid Flow in Minichannels and Microchannels. Chemical, Petrochemical & Process. Elsevier Science, 2006.

[71] S. G. Kandlikar and H. R. Upadhye. Extending the heat flux limit with enhanced microchannels in direct single-phase cooling of computer chips. In Semiconductor Thermal Measurement and Management IEEE Twenty First Annual IEEE Symposium, 2005., pages 8–15, 2005.

[72] Mark E. Steinke and Satish G. Kandlikar. An Experimental Investigation of Flow Boiling Characteristics of Water in Parallel Microchannels. Journal of Heat Transfer, 126(4):518–526, 05 2004.

[73] P. Mastinu, J. Praena, G. Martín-Hernández, N. Dzysiuk, G. Prete, R. Capote, M. Pignatari, and A. Ventura. Status of the LEgnaro NeutrOn Source facility (LENOS). *Physics Procedia*, 26:261 –273, 2012. Proceedings of the first two meetings of the Union of Compact Accelerator-Driven Neutron Sources.

[74] Results obtained by J. Baggemann, which will be published in 'Technical design report of the High Brilliance neutron Source HBS (2023)'.

[75] T. Weber *et al.*, 'Improvements in electron beam monitoring and heat flux flatness at the JUDITH 2-facility', in *Fusion Engineering and Design*, Oct. 2015, vol. 96–97, pp. 187–191. doi: 10.1016/j.fusengdes.2014.11.014.

[76] F. A. Lukiyanov, E. I. Rau, and R. A. Sennov, 'Depth range of primary electrons, electron beam broadening, and spatial resolution in electron-beam studies', *Bulletin of the Russian Academy of Sciences: Physics*, vol. 73, no. 4, pp. 441–449, 2009, doi: 10.3103/S1062873809040029.

[77] U. Fano, 'Penetration of Protons, Alpha Particles, and Mesons. [Online]. Available: https://www.annualreviews.org/doi/pdf/10.1146/annurev.ns.13.120163.000245

[78] V. P. Budaev *et al.*, 'High-heat flux tests of tungsten divertor mock-ups with steady-state plasma and e-beam', *Nuclear Materials and Energy*, vol. 25, Dec. 2020, doi: 10.1016/j.nme.2020.100816.

[79] N. Tosun and C. Cogun, "Analysis of wire erosion and workpiece surface roughness in wire electrical discharge machining," Proc Inst Mech Eng B J Eng Manuf, vol. 217, no. 5, 2003, doi: 10.1243/095440503322011353.

[80] M. Simoncelli, N. Marzari, and A. Cepellotti, “Generalization of Fourier’s Law into Viscous Heat Equations,” Phys Rev X, vol. 10, no. 1, 2020, doi: 10.1103/PhysRevX.10.011019.

[81] I. V. Savchenko and S. V. Stankus, “Thermal conductivity and thermal diffusivity of tantalum in the temperature range from 293 to 1800 K,” Thermophysics and Aeromechanics, vol. 15, no. 4, 2008, doi: 10.1007/s11510-008-0017-z.

[82] Katto, Y. ‘Critical heat flux.’ International Journal of Multiphase Flow 20 (1994): 53-90.

[83] F. Inasaka and H. Nariai, ‘Evaluation of subcooled critical heat flux correlations for tubes with and without internal twisted tapes’, *Nuclear Engineering and Design*, vol. 163, no. 1–2, pp. 225–239, Jun. 1996, doi: 10.1016/0029-5493(95)01170-6.

[84] G. P. Celata, ‘On the application method of critical heat flux correlations’, *Nuclear Engineering and Design*, vol. 163, no. 1–2, pp. 241–242, Jun. 1996, doi: 10.1016/0029-5493(95)01171-4.

[85] P. Hejzlar and N. E. Todreas, ‘Consideration of critical heat flux margin prediction by subcooled or low quality critical heat flux correlations’, *Nuclear Engineering and Design*, vol. 163, no. 1–2, pp. 215–223, 1996, doi: 10.1016/0029-5493(95)01169-2.

[86] S. G. Kandlikar, Heat Transfer and Fluid Flow in Minichannels and Microchannels, 2005. eBook ISBN: 9780080456188. Elsevier Science.

[87] S. M. Ghiaasiaan and R. C. Chedester, ‘Boiling incipience in microchannels’, Int J Heat Mass Transf, vol. 45, no. 23, pp. 4599–4606, Nov. 2002, doi: 10.1016/S0017-9310(02)00167-9.

[88] T. SATO and H. MATSUMURA, ‘On the Conditions of Incipient Subcooled-Boiling with Forced Convection’, Bulletin of JSME, vol. 7, no. 26, pp. 392–398, 1964, doi: 10.1299/jsme1958.7.392.

[89] W. Qu and I. Mudawar, ‘Prediction and measurement of incipient boiling heat flux in micro-channel heat sinks’, Int J Heat Mass Transf, vol. 45, no. 19, pp. 3933–3945, Sep. 2002, doi: 10.1016/S0017-9310(02)00106-0.

[90] G. M. Roach, S. I. Abdel-Khalik, S. M. Ghiaasiaan, M. F. Dowling, and S. M. Jeter, ‘Low-Flow Critical Heat Flux in Heated Microchannels’, Nuclear Science and Engineering, vol. 131, no. 2–3, pp. 411–425, 1999, doi: 10.13182/nse99-a2043.

[91] G. and A.-K. S. and G. S. and D. M. and J. S. Roach Jr, 'Low-flow critical heat flux in heated microchannels', Nuclear Science and Engineering, vol. 131, no. 3, pp. 411–425, 1999.

[92] A. M. and N. A. and B. G. Lezzi, 'Experimental data on CHF for forced convection water boiling in long horizontal capillary tubes', International Heat Transfer Conference Digital Library, 1994.

[93] W. Qu and I. Mudawar, 'Measurement and correlation of critical heat flux in two-phase micro-channel heat sinks', Int J Heat Mass Transf, vol. 47, no. 10–11, pp. 2045–2059, 2004, doi: 10.1016/j.ijheatmasstransfer.2003.12.006.

[94] D. Liu, P. S. Lee, and S. v. Garimella, 'Prediction of the onset of nucleate boiling in microchannel flow', Int J Heat Mass Transf, vol. 48, no. 25–26, pp. 5134–5149, Dec. 2005, doi: 10.1016/j.ijheatmasstransfer.2005.07.021.

[95] Alfredo Ferrari, Paola R. Sala, Alberto Fass`o, Johannes Ranft. Fluka: a multi-particle transport code(manual). (Program version 2023).

[96] W. Ulmer and E. Matsinos, 'Theoretical methods for the calculation of Bragg curves and 3D distributions of proton beams', *European Physical Journal: Special Topics*, vol. 190, no. 1. pp. 1–81, 2010. doi: 10.1140/epjst/e2010-01335-7.

[97] G. Pluvinage, 'Notch Effects in Fatigue and Fracture', in *Notch Effects in Fatigue and Fracture*, G. Pluvinage and M. Gjonaj, Eds. Dordrecht: Springer Netherlands, 2001, pp. 1–22. doi: 10.1007/978-94-010-0880-8_1.

[98] N. Ophoven *et al.*, 'Monte Carlo simulation of proton- and neutron-induced radiation damage in a tantalum target irradiated by 70 MeV protons', *Appl Phys A Mater Sci Process*, vol. 127, no. 8, Aug. 2021, doi: 10.1007/s00339-021-04713-4.

[99] J. Chen *et al.*, 'Mechanical properties of pure tantalum after 800 MeV proton irradiation', *Journal of Nuclear Materials*, vol. 298, no. 3, pp. 248–254, 2001, doi: https://doi.org/10.1016/S0022-3115(01)00654-7.

[100] T. S. Byun and S. A. Maloy, 'Dose dependence of mechanical properties in tantalum and tantalum alloys after low temperature irradiation', *Journal of Nuclear Materials*, vol. 377, no. 1, pp. 72–79, Jun. 2008, doi: 10.1016/j.jnucmat.2008.02.034.

[101] F. Jikol, M. Z. Akop, Y. M. Arifin, M. A. Salim, and S. G. Herawan, 'A Study of Steady-State Thermal Distribution on Circular Plate Using ANSYS', International Journal of Nanoelectronics and Materials, vol. 14, no. Special Issue ISSTE, 2021.

[102] W. Yang, L. Mao, W. Wang, C. Qu, J. Shu, and J. He, 'Temperature and stress of gas generator under unsteady state based on ANSYS', Guti Huojian Jishu/Journal of Solid Rocket Technology, vol. 42, no. 2, 2019, doi: 10.7673/j.issn.1006-2793.2019.02.005.

[103] V. B. Shim, J. Böshme, P. Vaitl, C. Josten, and I. A. Anderson, 'An Efficient and Accurate Prediction of the Stability of Percutaneous Fixation of Acetabular Fractures with Finite Element Simulation', J Biomech Eng, vol. 133, no. 9, Oct. 2011, doi: 10.1115/1.4004821.

[104] F. Cardarelli. Materials Handbook. Springer International Publishing, 2008.

[105] ANSYS results obtained by J.Wolters, which will be published in 'Technical design report of the High Brilliance neutron Source HBS (2023)'.

[106] L. Anikanova, O. Volkova, A. Kurmangalieva, and N. Mesheulov, 'Solving heat engineering problems using the finite element method', Architecture and Engineering, vol. 6, no. 3, 2021, doi: 10.23968/2500-0055-2021-6-3-03-10.

[107] K. Q. Sun et al., "Optimisation of compatibility for improving elongation at break of chitosan/starch films," RSC Adv, vol. 9, no. 42, 2019, doi: 10.1039/c9ra04053f.

[108] P. Müller, A. Cantatore, J. L. Andreasen, J. Hiller, and L. de Chiffre, 'Computed tomography as a tool for tolerance verification of industrial parts', in Procedia CIRP, 2013, vol. 10, pp. 125–132. doi: 10.1016/j.procir.2013.08.022.

[109] Y. Wu et al., 'Analysis of manufacturing-induced defects and structural deformations in lithium-ion batteries using computed tomography', Energies (Basel), vol. 11, no. 4, Apr. 2018, doi: 10.3390/en11040925.

List of Figures

List of Tables

Abbreviations

HBS High Brilliance neutron Source

Hi-CANS High Current Accelerator-driven Neutron Source

ESS European Spallation Source

ILL Institute Laue-Langevin

ISIS Neutron and Muon Source

FRM II The research neutron source Heinz Maier-Leibnitz

FLUKA FLUktuierende KAskade

ANSYS Analysis of Systems

CPU Central Processing Unit

ENDF Evaluated Nuclear Data File

JENDL Japanese Evaluated Nuclear Data Library

ZEA-1 Central Institute for Engineering, Electronics and Analytics (ZEA). Engineering and Technology (ZEA-1)

JCNS Jülich Centre for Neutron Science

IEK Institute for Energy and Climate Research

MC Monte Carlo

SRIM Stopping and Range of Ions in Matter

TMR Target-Moderator-Reflector

IR Infrared camera

CHF Critical Heat Flux

DPA Displacement Per Atom

CFD Computational Fluid Dynamics

EDM Electrical discharge machining

CT Computed Tomography

Acknowledgements

The research and results described in this thesis would not have been possible without the help and support of many people at JCNS-2 and ZEA-1, and I would like to thank everyone who participated and contributed directly or indirectly to this work. In particular, I would like to express my sincere gratitude to the following people.

First and foremost, I would like to acknowledge Prof. Dr. Thomas Brückel for providing me the opportunity to work at JCNS-2, and for making it possible for me as a PhD candidate to work on this interdisciplinary and thus very comprehensive project, which combines aspects of nuclear physics and thermo hydraulic as well as manufacturing engineering. It helps me to develop the ability to solve problems with multi-disciplinary skills. Thank you for providing me the opportunities to participate in various of academic conferences, which expand my vision and capabilities in target development for large-scale facilities.

I am incredibly grateful to my first supervisor, Prof. Dr. Ghaleb Natour, who is always so kind and professional. Thank you for regularly checking in on the progress of my dissertation, which motivates me to accomplish specific projects on time. Every time I discuss with you, I feel that I am always inspired and encouraged by your insightful advice. Thank you for your constructive suggestions on my research program, which have shaped the integrity and comprehensiveness of this project very well. Thank you for your generous support throughout my PhD.

I would like to express my sincere thanks to Prof. Lorenz Singheiser for agreeing to be my second referee. I really appreciate your strong support during my PhD, where you are so responsible and always have time to participate in the regular meetings to follow up on my progress. Thank you for your professionalism and enthusiasm for my PhD thesis, which has always inspired me and strengthened my interest in becoming a brilliant researcher. Thank you for reviewing this thesis carefully and for your nice feedback, which has always raised the quality of the thesis.

I would like to give special thanks to Dr. Thomas Gutberlet for including me in the HBS group, where I met so many kind and interesting people and gained lots of valuable and joyful experiences. Thank you for always forwarding potential job opportunities to me and being open when I need support.

In particular, I would like to thank Dr. Jingjing Li, who has been an ideal mentor for me. Thank you so much for opening the door to the FLUKA simulation for me. Thank you for proofreading and encouraging me to keep going forward during the stressful writing times. In addition to providing valuable insights into projects, you have always supported my personal growth as a researcher, guiding me into new areas. Thank you for always being a great listener when I was down and a great mentor when I was having a hard time. Thank you for always providing me with positive feedback and encouraging me to be brave in my work and life. Thank you for your concern, insight and humor.

I would like to express my sincere thanks to Dr. Ulrich Rücker for your strong support throughout my PhD. Since I was relatively new to this comprehensive project related with neutron science and physics engineering, I lost my way a bit at the beginning of my PhD thesis. Without your patient guidance and professional support, I am afraid that I would not have been able to proceed smoothly with my project. Thank you for arranging the weekly discussions, where I gained lots of valuable scientific knowledge and skills from you. I appreciate your insightful comments regarding the publications, which have always raised the quality of the manuscript and certainly contributed to the fact that the manuscript was accepted by the journal.

Besides, I would like to express my sincere thanks to Dr. Paul Zakalek, who always had time for me whenever I encountered problems and questions. Without you I would not have discovered my love for python. Thank you for improving my technical skills and your bright optimism and enthusiasm always cheered me. Thank you for always asking the right questions and giving me so much room for learning, thinking, and practicing. I am grateful for your reviewing the thesis carefully and encouraging me to find my true potential. Your insightful feedback always pushed me to sharpen my thinking about a subject. Special thanks to Paul for carefully proofreading the German version of the abstract.

I have to mention special thanks to Dr. Johannes Baggemann, who provides me so much strong support in my PhD project. Thank you so much for your great contribution in the high heat flux test of the first target at JUIDTH-2 facility and the kind support in data analysis. I am grateful for your patient explanations whenever I had questions and your professional suggestions regarding CFD simulations and the target design. Thank you for your recommended nice books regarding the microchannel cooling theory, which are very classic and useful. Thank you for your kind

assistance in the communication with the technical staffs at the JCNS workshop and the ZEA-1 workshop and always being a professional translator, without you the high heat flux test and optical microscopy measurement would not have been performed successfully. Thank you for your insightful opinions in many online and offline discussions. Thank you for your reviewing the thesis carefully and providing nice corrections.

In this regard, I also like to express my sincere gratitude to Dr. Jörg Wolters at ZEA-1, who is always so kind to offer me assistance and always with a smile. I am grateful for your great contribution in the target optimization with respect to mechanical and thermo-mechanical simulations with ANSYS. Thanks a lot for always quickly providing your outcome in the long iterative process. Thank you for your reviewing the thesis carefully and providing constructive corrections.

I am incredibly grateful to Dr. Yannick Beßler at ZEA-1, who is always so kind and friendly. Thank you for helping to coordinate the regular meetings to check on the progress of my PhD and for taking the time to attend each of my regular meetings. I appreciate you always providing nice suggestions to guide me forward on the right track. Thank you so much for your kind assistance in target prototype manufacturing and CT measurement at the ZEA-1 workshop, the relevant would not have been completed on time without your coordination. Special thanks to Yannick for your patient help in figuring out the PhD examination processes and kind support during my period.

Special thanks to Mr. Carsten Hoven at ZEA-1 for your professional assistance in the CT measurement to examine the manufacturing-related tolerance of the target and the discussions regarding the data analysis. Thank you for your patient explanations when I had questions concerning the CT data.

I would like to thank Dr. Eberhard Rosenthal at ZEA-1 for arranging the regular Doc meeting, where I got to know the other Phd students at ZEA-1. Thank you for providing me the opportunity to give a talk at ZEA colloquium, where I could share my PhD work to the other colleagues and received nice feedback.

I would like to thank the rest of the HBS team, Dr. Eric Mauerhofer, Dr. Jörg Voigt, Dr. Klaus Lieutenant, Dr. Tania Claudio Weber, Dr. Ivan Pechenizkiy, Dr. Junyang Chen, Dr. Monia EL Barbari and Norberto Schmidt, for all the interesting scientific exchanges and for the HBS lunch,

coffee talks and especially great company at conferences and workshops. Especially the HBS Unkel workshop was always a pleasure.

Many thanks also to all colleagues in JCNS-2 for the good teamwork. Special thanks to Ms. Barbara Daegener for her generous and perfect administrative assistance throughout my PhD.

I am very grateful to Ms. Sarah Lipke and Ms. Evelyn Dück at ZEA-1 for the well-organized regular meeting and kind administrative assistance at every point.

I express my sincere thanks to office colleagues Dr. Nileena Nandakumaran, Alexander Schwab, and Chengyang Yin and Dr. Monia EL Barbari for making a lively and fun work environment. Special thanks to Alex and Niklas Ophoven for proofreading the German version of the abstract.

During my time as a Ph.D. student, I thank Dr. Wenhai Ji, Dr. Zhanwen Ma for your invaluable friendship and the joy during stressful pandemic times.

I am forever indebted to my dearest sister Liqing. This would not have been possible without your infinite love and encouragement from you. Thanks for always being there and telling me “You can manage it!”.

In the end, I also want to dedicate special thanks to my parents. No words can express my deepest love and gratitude to my parents. Without the endless love, inspiration, and support that you gave me, I might not be the person I am today.